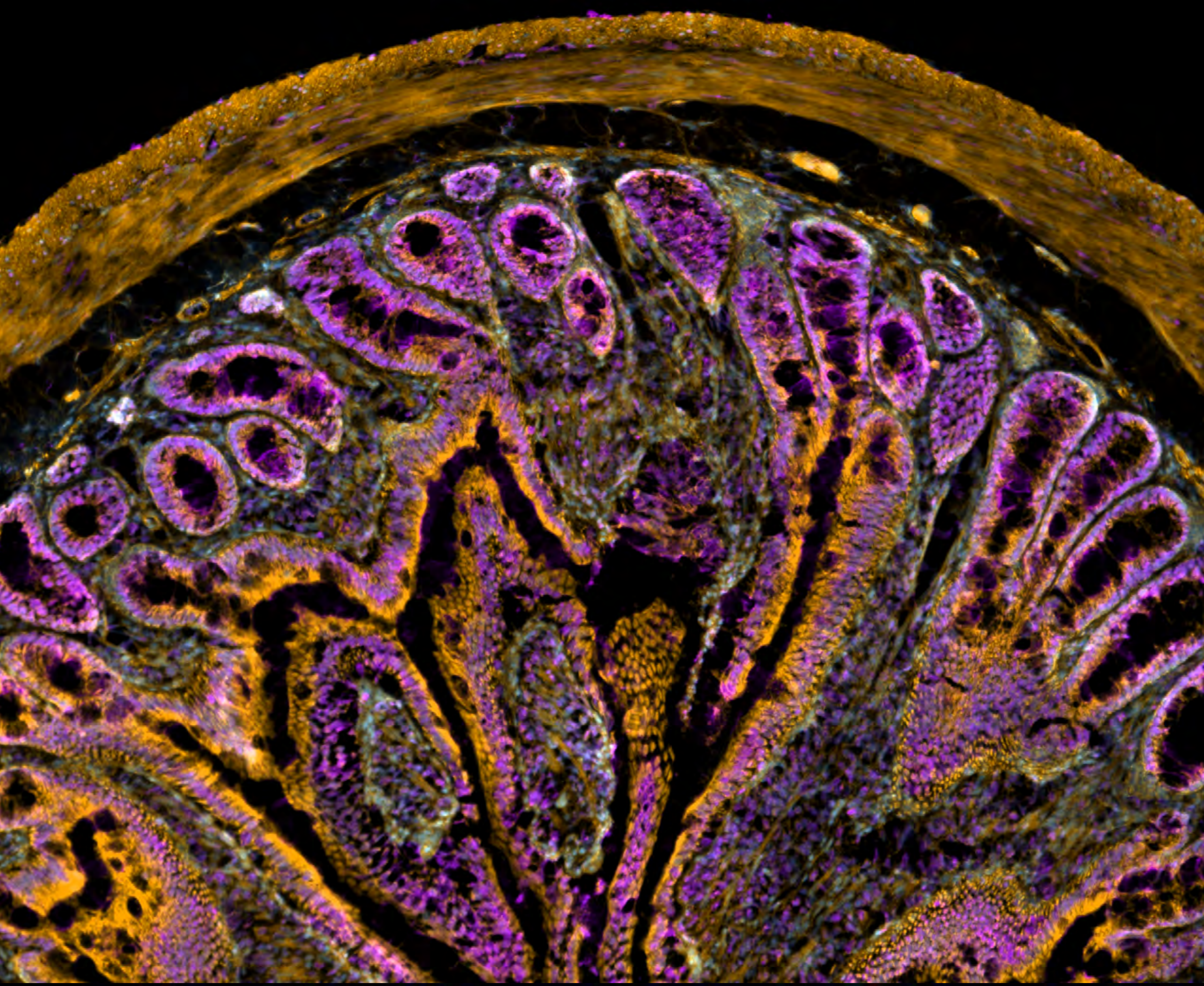

Seeing is Believing:
The Power of EVOS Imaging Systems in Uncovering Biological Insights

ARTICLE COLLECTION

WILEY

CURRENT PROTOCOLS
A Wiley Brand

Sponsored by:
Thermo Fisher
SCIENTIFIC
The world leader in serving science

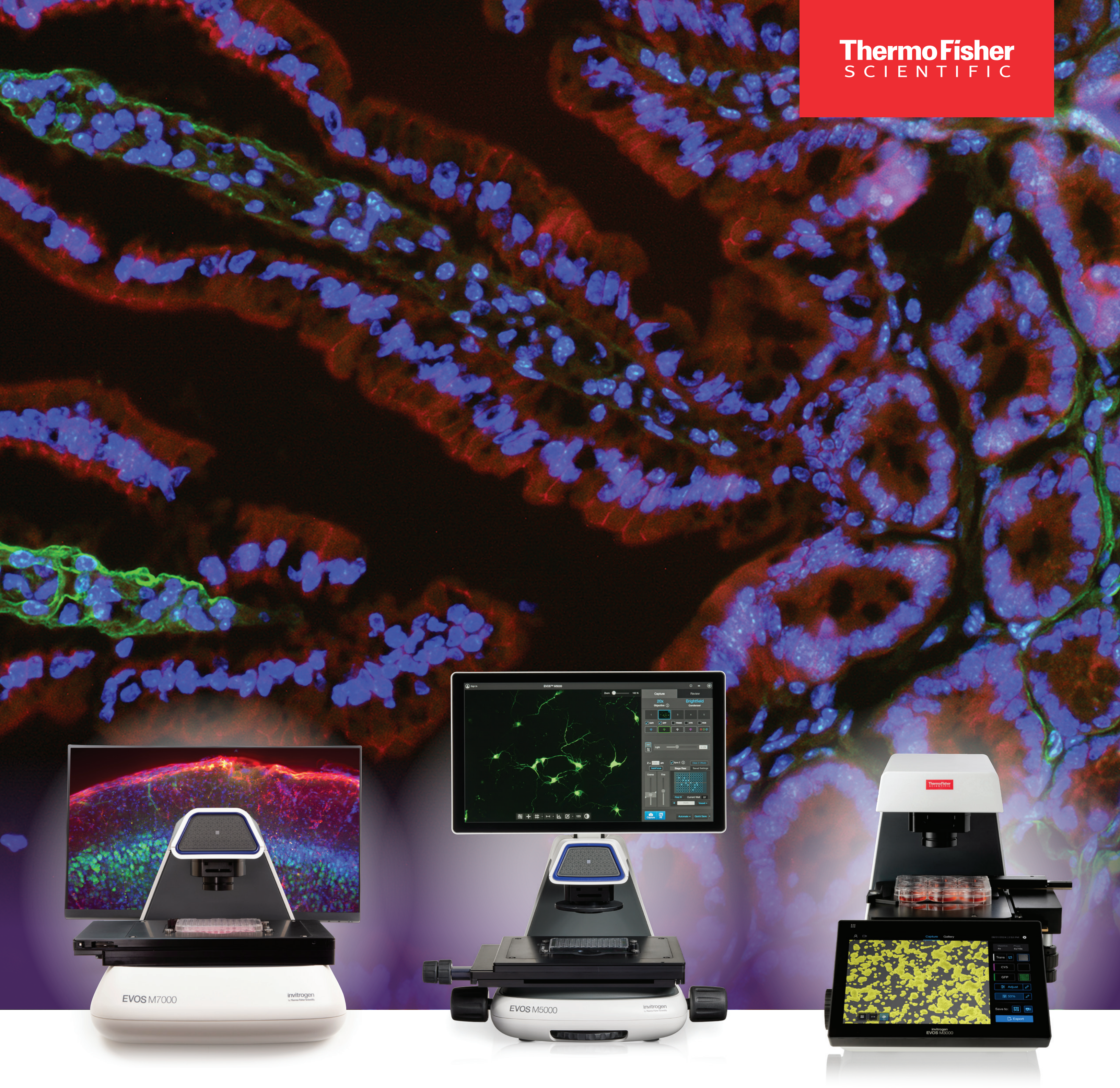
Thermo Fisher
SCIENTIFIC
EVOS M7000
invitrogen
EVOS M5000
invitrogen
EVOS M3000

Contents

Cover Image ©Thermo Fisher Scientific

Introduction

Imaging techniques have become indispensable in the life sciences, serving as vital instruments for unravelling the complexities of biological systems. The ability to visualize cellular processes at the molecular level has revolutionized our understanding of cell biology, particularly through the detailed observation of protein and gene expression within individual cells. Such high-resolution cell imaging not only enhances our basic scientific knowledge but is also crucial in applied fields like drug discovery, where it facilitates the rapid screening of potential therapeutics across numerous conditions in multiwell formats. The insights gained from these imaging applications guide the development of targeted treatments, enabling a more personalized approach to medicine. Furthermore, the continuous advancement in imaging technologies promises to propel life science research into new frontiers, expanding our capabilities to observe and manipulate life at its most fundamental level.

The EVOS Cell Imaging Systems have been at the forefront of this technology with over ten thousand references in the literature. The EVOS Imaging Systems are self-contained, easy to maintain, and they produce high-quality brightfield, phase contrast, and multichannel fluorescence images through a combination of customizable hardware configurations and software processing. Research publications involving assays such as cell proliferation, wound healing, immunofluorescence, and spatial transcriptomics all employ EVOS Cell Imaging Systems.

To highlight its contributions to research, we present this collection of articles illustrating the variety of areas that utilize EVOS Cell Imaging Systems. These articles feature contributions to the fields of cell biology, immunology, drug discovery, and biomaterials.

First, Li *et al.* describe the characterization of a coiled-coil forming peptide (denoted as K5). When fused to the target protein of interest, K5 can function as a cell-penetrating peptide and significantly enhance delivery into cells for therapeutic purposes, including gene editing. To validate this, the degree of an EGFP-K5 fusion internalization by various cell types was quantified by imaging GFP fluorescence on the EVOS M5000 Imaging System.

Next, Hansell *et al.* demonstrate the use of a fluorescently conjugated chemokine ligand to identify the expression of its associated receptor (ACKR2) on stromal cells. A key piece of evidence involved detection of gene expression by in situ hybridization for this chemokine receptor and imaged using the EVOS M7000 Imaging System.

Third, Maitz *et al.* (2020) examine the ability of cross-linking on the longevity and effectiveness of a collagen-elastin dermal template used for skin tissue regeneration and wound healing. The EVOS M7000 Imaging System was used to image and quantify pore size differences in non-cross-linked and cross-linked samples in histochemically stained sections.

Finally, Jin *et al.* investigated the role of two different miRNAs in giant cell tumor of bone (GCTB) cultures and their impact on a specific fibroblast growth factor receptor. The EVOS M7000 System was utilized for examining both proliferation and translocation rates of cultured GCTB cells.

Taken together, this article collection emphasizes the versatility of EVOS Cell Imaging Systems, and the wide range of research areas in which they can be employed. For more information and testimonials regarding EVOS Imaging Systems, we encourage you to access the following resources from Thermo Fisher Scientific:

- EVOS Cell Imaging Systems
- EVOS Cell Imaging System Resources
- Imaging Protocols Handbook
- Cell Analysis Resource Center

REFERENCES

Li, J., Tuma, J., Han, H., Kim, H., Wilson, R. C., Lee, H. Y., Murthy, N., The Coiled-Coil Forming Peptide (KVSALKE)5 Is a Cell Penetrating Peptide that Enhances the Intracellular Delivery of Proteins. Adv. *Healthcare Mater*. 2021, 2102118. https://doi.org/10.1002/adhm.202102118

Hansell, C.A., Love, S., Pingen, M., Wilson, G.J., MacLeod, M. and Graham, G.J. (2020), Analysis of lung stromal expression of the atypical chemokine receptor ACKR2 reveals unanticipated expression in murine blood endothelial cells. *Eur. J. Immunol.*, 50: 666-675. https://doi.org/10.1002/eji.201948374

Maitz, J, Wang, Y, Fathi, A, et al. The effects of cross-linking a collagen-elastin dermal template on scaffold bio-stability and degradation. *J Tissue Eng Regen Med*. 2020; 14: 1189-1200. https://doi.org/10.1002/term.3082

Jin, Y, Zhang, J, Zhu, H, Fan, G, Zhou, G. Expression profiles of miRNAs in giant cell tumor of bone showed miR-187-5p and miR-1323 can regulate biological functions through inhibiting FRS2. *Cancer Med*. 2020; 9: 3163- 3173. https://doi.org/10.1002/cam4.2853

The Coiled-Coil Forming Peptide (KVSALKE)$_5$ Is a Cell Penetrating Peptide that Enhances the Intracellular Delivery of Proteins

Jie Li, Jan Tuma, Hesong Han, Hansol Kim, Ross C. Wilson, Hye Young Lee, and Niren Murthy**

Protein-based therapeutics have the potential to treat a variety of diseases, however, safe and effective methods for delivering them into cells need to be developed before their clinical potential can be realized. Peptide fusions have great potential for improving intracellular delivery of proteins. However, very few peptides have been identified that can increase the intracellular delivery of proteins, and new peptides that can enhance intracellular protein delivery are greatly needed. In this report, the authors demonstrate that the coiled-coil forming peptide (KVSALKE)$_5$ (termed K5) can function as a cell penetrating peptide (CPP), and can also complex other proteins that contain its partner peptide E5. It is shown here that GFP and Cas9 fused to the K5 peptide has dramatically enhanced cell uptake in a variety of cell lines, and is able to edit neurons and astrocytes in the striatum and hippocampus of mice after a direct intracranial injection. Collectively, these studies demonstrate that the coiled-coil forming peptide (KVSALKE)$_5$ is a new class of multifunctional CPPs that has great potential for improving the delivery of proteins into cells and in vivo.

1. Introduction

Protein-based therapeutics have the potential to treat a variety of diseases, such as neurodegenerative diseases, cancer, and genetic diseases.[1–5] However, before the tremendous potential of protein therapeutics can be realized, safe and effective methods for delivering them into cells need to be developed. Developing effective intracellular protein delivery vehicles has been challenging. Proteins are in general intolerant to chemical modifications, easily denature, and also do not complex cationic materials as readily as nucleic acids.[6] A wide variety of protein delivery strategies are currently being considered, based upon gold nanoparticles, block copolymers, cationic lipids, and cell penetrating peptides (CPPs), which have shown promising results in cell culture and animal studies.[7–9] However, it is unclear if these delivery vectors will have the properties needed to succeed in human clinical trials, given their ill-defined nature, large size, and toxicity. The development of safe and effective protein delivery vectors is still an unsolved problem.

Intracellular protein delivery strategies based upon fusing short peptides (termed CPPs) to proteins have tremendous potential for enhancing the intracellular delivery of proteins, and also have the properties needed to succeed in human clinical trials.[10,11] In particular, protein fusions are a single molecular species and can be easily synthesized and characterized on a large scale. Protein fusions also have a much smaller molecular weight than nanoparticles and will be able to access tissues and cells that nanoparticles cannot. Finally, protein fusions should have lower toxicity than cationic nanoparticles because of their lower charge density, and will also not activate toll-like receptor ligands, as cationic lipids do.[12,13]

Pioneering studies from the Dowdy laboratory demonstrated that short cationic peptide sequences 10–20 amino acids in length derived from the TAT protein were able to deliver proteins such as CRE, beta-galactosidase, and GFP into a variety of cell types and even in vivo.[14–18] TAT appears to enhance cell uptake via its cationic charge density, which causes binding with cellular proteoglycans. The efficiency of TAT was further improved by fusing it to an endosomal disruptive peptide from the Influenza virus, HA, to generate a fusion peptide that could stimulate both endocytosis and endosomal disruption.[15,16] Based upon these studies a variety of other CPPs have been explored. For example, the gene editing enzymes, Cas9 and zinc finger nucleases, fused to the SV40 nuclear localization signals (NLS), were able to directly edit cells in vitro and vivo.[17,19] In addition to TAT, a variety of other peptides for enhancing intracellular protein delivery

---

J. Li, H. Han, H. Kim, N. Murthy
Department of Bioengineering
University of California, and the Innovative Genomics Institute
2151 Berkeley Way, Berkeley, CA 94720, USA
E-mail: nmurthy@berkeley.edu

J. Tuma, H. Y. Lee
The Department of Cellular and Integrative Physiology
the University of Texas Health Science Center at San Antonio
San Antonio, TX 78229, USA
E-mail: leeh6@uthscsa.edu

R. C. Wilson
The Innovative Genomics Institute
2151 Berkeley Way, Berkeley, CA 94720, USA

The ORCID identification number(s) for the author(s) of this article can be found under https://doi.org/10.1002/adhm.202102118

DOI: 10.1002/adhm.202102118

have been developed, of which the peptide GALA is perhaps the most well studied.[20,21] The peptide GALA is a pH sensitive membrane disruptive peptide, which forms amphiphilic helices at pH 5.0, and can enhance the endosomal release of proteins. GALA has been fused to antibodies and the ribosome inactivating protein HBP, and was able to dramatically improve the intracellular delivery of these proteins.

Despite these encouraging results, there is still a great need for improving the efficiency of CPPs fused to proteins. Current delivery peptides used in protein fusions are frequently positively charged peptides and appear to function by increasing the positive charge density of their target protein.[22–24] However, making cell delivery dependent upon charge density is challenging because every protein has its own unique charge density, and will require its own unique peptide fused to it. Related to this issue is the fact that CPPs have only been examined on a moderate number of proteins, and it is unclear if they have the versatility needed to act as universal protein delivery reagents. For example, GFP has been the most widely studied protein fused to CPPs, and here large enhancements in cell delivery are observed after fusion with the positively charged peptides such as the TAT peptide.[25] However, fusing the TAT peptide to a larger protein such as Cas9 results in negligible enhancements in uptake.[26] Developing CPPs that can enhance the delivery of larger functional proteins has been a major challenge because they will most likely require fusion to 40–50 amino acid peptide segments, to compensate for their large size and charge density. However, current CPPs are unstructured peptides and most proteins will not tolerate fusion to large unstructured peptides.[27] Thus, expanding the arsenal of CPPs will consequently have numerous applications in biotechnology.

Peptides that form coiled-coil motifs are potential candidates for CPPs that can enhance the delivery of proteins. Coiled-coil peptides form amphipatic alpha helices that self-assemble with partner peptides due to the complementary nature of their hydrophobic and charged domains.[28] Coiled-coil forming peptides also have the potential to interact strongly with cell membranes because they generate amphiphatic alpha helices, with hydrophobic and charged surfaces, which in general bind membranes with much higher affinity than unstructured peptides with a similar hydrophobic–hydrophilic balance.[29–31] For example, Rabe et al. demonstrated that the coiled-coil peptide $(KIAALKE)_3$ could bind lipid bilayers with a K_d of 10^{-9} M, and could also enhance lipid bilayer fusion and facilitate drug release from liposomal vectors intracellularly.[32–34] Coiled-coil forming peptides have the potential to act as CPPs, given their ability to bind cell membranes tightly.

Using coiled-coil peptides as CPPs could have many potential benefits over existing CPPs commonly fused to proteins. For example, coiled-coil peptides have a well-defined structure in contrast to CPPs such as TAT and SV40 NLS, which appear to be random coil peptides.[35] Fusing structureless peptides to proteins can be problematic because it increases the chances of generating an unfoldable protein. In addition, current CPPs are primarily composed of cationic peptides such as Arg_n, which bind membranes through electrostatic interactions, and do not insert into the hydrophobic core of the membrane.[36,37] In contrast, coiled-coil peptides contain hydrophobic surfaces and can bind and insert into the hydrophobic core of membranes,[31] potentially leading to efficient endosomal disruption. Finally, proteins fused to coiled-coil peptides will also be able to complex other proteins or particles, which could enable cell targeting and endosomal disruption functions.[38,39] However, despite their potential, the ability of coiled-coil peptides to enhance the delivery of proteins has never been investigated.

In this report, we demonstrate that that the coiled-coil forming peptide $(KVSALKE)_5$ (termed K5) can function as a CPP, and can also complex proteins that contain its partner peptide E5 (see **Figure 1**). We show here that GFP and Cas9 fused to the K5 peptide had dramatically enhanced cell uptake in a variety of cell lines, and that Cas9-K5 was able to edit brain tissue in neurons and astrocytes of striatum and hippocampus after a direct intracranial injection into adult mouse brains. Collectively, these studies demonstrate that the coiled-coil forming peptide $(KVSALKE)_5$ is a new class of multifunctional CPPs that has great potential for improving the delivery of proteins into cells and in vivo.

2. Results and Discussion

2.1. The K5 Peptide Enhances the Delivery of EGFP into Various Cell Types

We performed experiments to determine if the coiled-coil forming peptide K5 could act as a CPP and enhance the delivery of EGFP into cells (see **Figure 2**a). We selected EGFP as a model protein because of its straightforward fluorescent readout, and because it is widely used as a reporter protein for investigating the efficacy of CPPs, and would allow us to compare K5 with other CPPs reported in the literature. K5 was fused to EGFP at its N-terminal and expressed in high yields in *Escherichia coli* (*E. coli*) (10 mg L^{-1}). K5 was fused to the N-terminus of Cas9 because this site tolerates fusion proteins well, and several Cas9 fusions at the N-terminus have already been made, which were enzymatically active. K5-EGFP was incubated with NIH 3T3 and Hela cells at 166 µg mL^{-1} for 4 h in the presence of 10% FBS, the cells were washed, and then imaged via fluorescent microscopy. As a control, EGFP only was incubated with NIH 3T3 and Hela cells and imaged. Figure 2b demonstrates that K5 significantly enhances the delivery of EGFP into NIH 3T3 cells. Notably, cells treated with EGFP had minimal levels of fluorescence, whereas cells treated with EGFP-K5 had high levels of green fluorescence, which appeared to have distributed throughout the cell. We performed flow cytometry experiments to further quantify the increase in fluorescence observed with K5. Figure 2c,d demonstrates that K5 dramatically increased the number of GFP positive cells in both NIH 3T3 and HeLa cells. NIH 3T3 and HeLa cells treated with GFP were only 1–2% GFP positive, whereas cells treated with GFP-K5 were 20% and 40% GFP positive, respectively (see Figures S1 and S2, Supporting Information, for detailed flow cytometry histograms). In addition, there was no sign of toxicity in cells treated with GFP-K5 and these experiments demonstrate that K5 can dramatically increase the uptake of small proteins into cells.

2.2. Cas9 Fused to K5 Is Enzymatically Active

Although CPPs have been intensely investigated for enhancing the delivery of GFP, there are very few studies investigating their

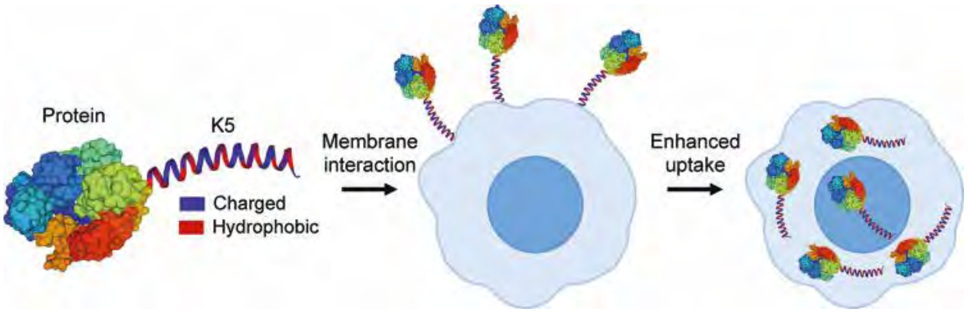

Figure 1. The coiled-coil forming peptide $(KVSALKE)_5$ (K5) is a cell penetrating peptide and can enhance the delivery of proteins into cells. The peptide $(KVSALKE)_5$ (K5) is fused to proteins and enhances cell uptake via its binding with cell membranes.

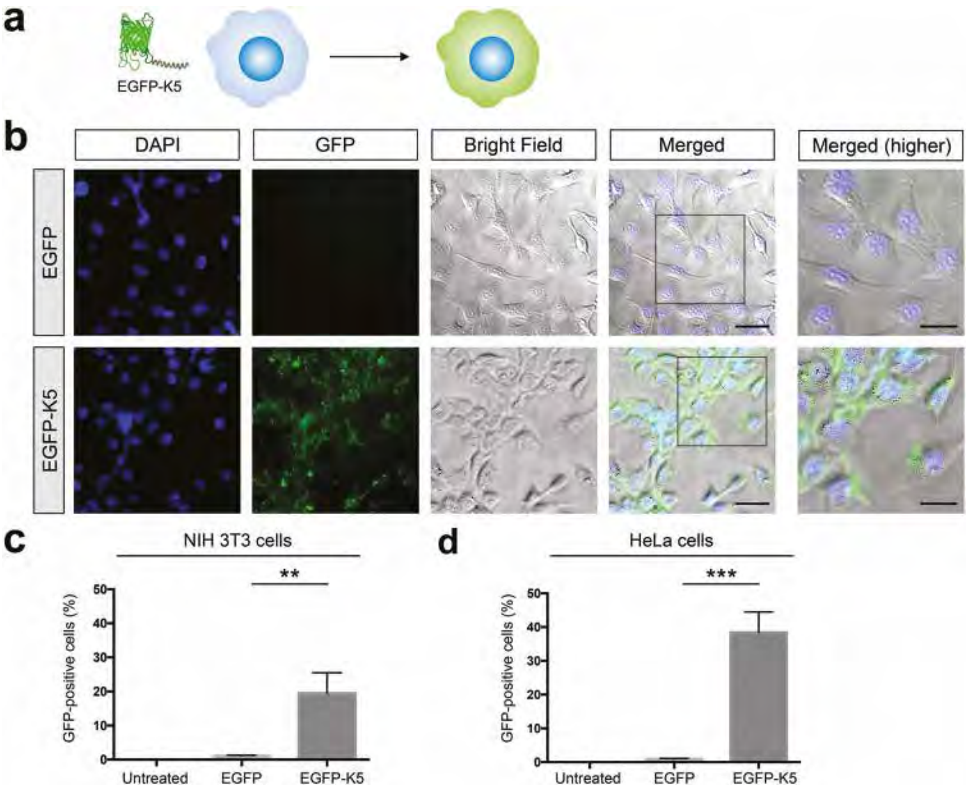

Figure 2. K5 enhances the delivery of EGFP into various cell types. a) Schematic illustration of enhanced cellular uptake of EGFP by K5. b) K5 facilitates the internalization of EGFP into NIH 3T3 cells. Higher magnifications of the merged images (black boxes) are shown in the right panel. Scale bars represent 50 µm (left panels) and 30 µm (right panels), respectively. c,d) Quantification of flow cytometry data of EGFP or EGFP-K5 uptake in c) NIH 3T3 cells and d) HeLa cells. Mean ± SEM. $^{**}p < 0.01$ and $^{***}p < 0.001$ by permutation *t*-test. *p* values were calculated between EGFP and EGFP-K5.

ability to deliver functional proteins, and their results with proteins outside of GFP have been mixed. For example fusion of TAT to the Cas9 RNP results in only moderate increases in cell delivery, and requires coformulation with additional TAT peptides for delivery into cells.[26] Fusion of 7 SV40-NLS sequences to Cas9 was able to enhance delivery into the brain,[19] and these results demonstrate that CPPs can enhance the delivery of even large proteins. However, outside of the SV40-NLS and TAT, the ability of other CPPs to enhance the delivery of the Cas9 RNP into cells and in vivo has not been investigated, and could improve numerous aspects of this delivery strategy, in particular, protein yield, editing efficiency, and cell tropism. There is consequently great interest in exploring other types of CPPs that can enhance the delivery of the Cas9 RNP.

In our study, we investigated if the K5 peptide could enhance the delivery of the Cas9 RNP into cells and further in vivo. The K5 peptide was fused to the N-terminus of the Cas9 protein, and expressed in *E. coli*, with a yield of 10 mg L^{-1} (see Figure S3, Supporting Information, for gel characterization). The nuclease activity of Cas9-K5 RNP was compared against Cas9 RNP (native Cas9 RNP), with regards to their ability to cleave a PCR amplicon. A total of 500 ng of Cas9-K5 RNP or Cas9 RNP were mixed

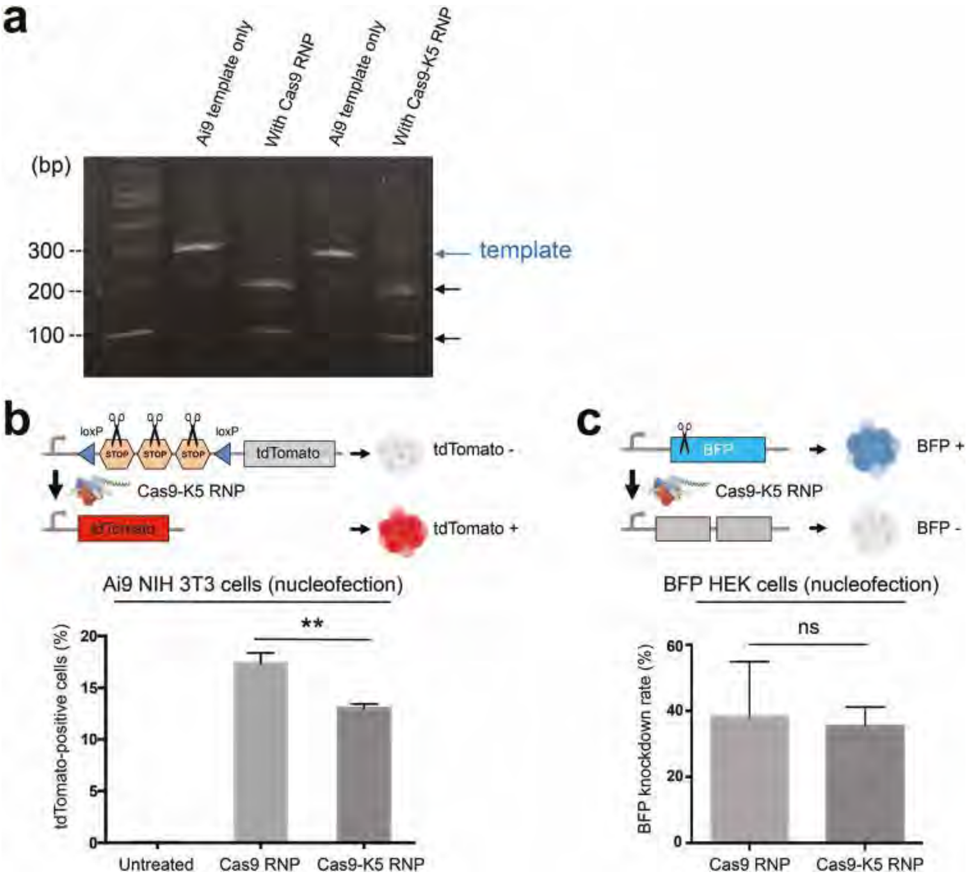

Figure 3. Cas9 fused to K5 is enzymatically active. a) In vitro Ai9 template DNA cleavage assay demonstrates that the Cas9-K5 RNP has 71% of the nuclease activity of the native Cas9 RNP (Cas9 RNP). b,c) Quantification of flow cytometry data of b) tdTomato-positive cells in Ai9 NIH 3T3 cells and c) BFP knockdown rate in BFP HEK cells by Cas9 RNP or Cas9-K5 RNP delivered by nucleofection. Mean ± SEM. $^{**}p < 0.01$ and ns $p < 0.05$ by permutation *t*-test. *p* values were calculated between Cas9 RNP and Cas9-K5 RNP.

with 500 ng of template DNA (1:1 mass ratio), and the cutting efficiency was determined by gel electrophoresis. **Figure 3**a demonstrates that although the Cas9-K5 RNP does have enzymatic activity, its ability to cleave DNA is lower than Cas9 RNP. For example, under these conditions, the Cas9 RNP cleaved 100% of the template DNA, whereas the Cas9-K5 RNP cleaved only 71%. The Cas9 RNP also had a higher level of enzymatic activity than the Cas9-K5 RNP, when mixed with template DNA at a 0.5:1 mass ratio and a 2:1 mass ratio (see Figure S4, Supporting Information). The K5 peptide could be interfering with the activity of Cas9 in multiple ways, given the numerous conformational changes that the Cas9 protein undergoes during its catalytic cycle.

Next, the ability of the Cas9-K5 RNP to edit cells after nucleofection was investigated and compared against the Cas9 RNP, using either Ai9 NIH 3T3 cells or BFP-HEK cells. Ai9 NIH 3T3 cells have a loxP-flanked STOP cassette (i.e., three repeated SV40 polyA signal sequences) upstream of a tdTomato transgene that is integrated into their genome, and will generate red fluorescence after gene editing and removal of the STOP cassette.[40] The Cas9-K5 RNP and Cas9 RNP had similar levels of editing in cells after electroporation. The Cas9-K5 RNP edited 14% of Ai9 3T3 fibroblasts which was 77% of the editing rate of the Cas9 RNP (see Figure 3b; see Figure S5, Supporting Information, for detailed flow cytometry histograms). We further tested the Cas9-K5 RNP activity in BFP HEK cells. Gene editing efficiency was calculated by subtracting the percentage of BFP-negative cells in the untreated cells from the percentage of BFP-negative cells in the treated cells. BFP HEK cells treated with Cas9-K5 RNP had a similar BFP knockdown rate to cells treated with Cas9 RNP targeting the BFP gene (see Figure 3c; see Figure S6, Supporting Information, for detailed flow cytometry histograms). These results demonstrate that the Cas9-K5 RNP has sufficient enzymatic activity for gene editing in cells.

2.3. K5 Peptide Enhances the Delivery of Cas9 RNP into Various Cell Types

To further explore whether K5-fused Cas9 could enhance gene editing efficiency, we first explored the internalization of the Cas9-K5 RNP in various cell types. ATTO 550-labeled sgRNA was assembled with Cas9 or Cas9-K5 to form fluorescent Cas9 RNP or Cas9-K5 RNP and their uptake efficiency was measured by flow

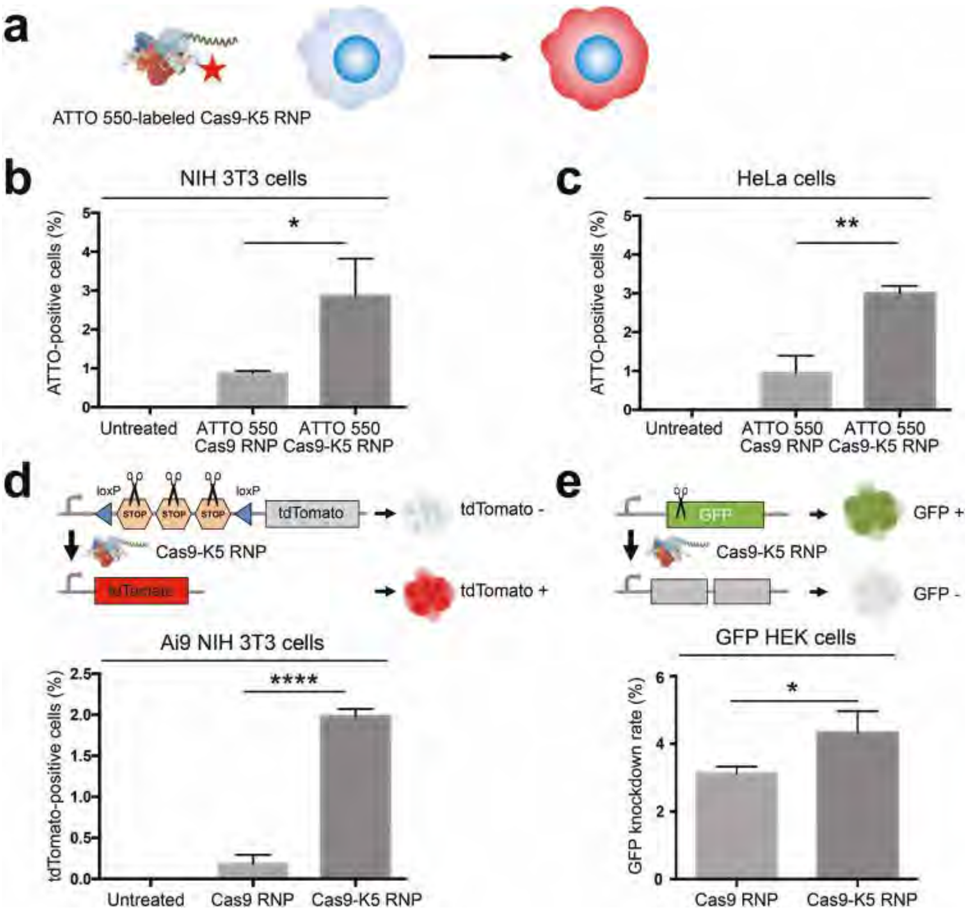

Figure 4. The K5 peptide enhances the delivery of the Cas9 RNP into various cell types. a) Schematic illustration of enhanced uptake of ATTO 550-labeled Cas9 RNP by the K5 peptide in cells. b,c) K5 enhanced uptake of ATTO 550-labeled Cas9 RNP: Quantification of flow cytometry data of ATTO 550-positive cells in b) NIH 3T3 cells and c) HeLa cells using ATTO 550-labeled Cas9 RNP or ATTO 550-labeled Cas9-K5 RNP. d,e) The K5 peptide enhanced the gene editing efficiency of the Cas9 RNP: Quantification of flow cytometry data of d) tdTomato-positive cells in Ai9 NIH 3T3 cells and e) GFP knockdown rate in GFP HEK cells by Cas9 RNP or Cas9-K5 RNP. Mean ± SEM. $^{*}p < 0.05$, $^{**}p < 0.01$, and $^{****}p < 0.0001$ by permutation *t*-test. *p* values were calculated between Cas9 RNP and Cas9-K5 RNP.

cytometry (see **Figure 4**a). The K-5 peptide causes a significant enhancement of cell internalization of the Cas9 RNP in NIH 3T3 cells, even in the presence of serum proteins. For example, incubating NIH 3T3 cells with Cas9-K5 RNP in DMEM medium with 10% FBS resulted in more than 3% of cells being ATTO 550-positive, while NIH 3T3 cells incubated with Cas9 RNP exhibited less than a 1% positive rate, leading to approximately a threefold increase in uptake (see Figure 4b; see Figure S7, Supporting Information, for detailed flow cytometry histograms). A similar trend was confirmed in HeLa cells, where cells treated with Cas9-K5 RNP also showed more than a 3% ATTO 550-positive rate, while Cas9 RNP-treated HeLa cells were less than 1% ATTO 550-positive (see Figure 4c; see Figure S8, Supporting Information, for detailed flow cytometry histograms).

2.4. The K5 Peptide Enhances the Gene Editing Efficiency in Ai9 3T3 Cells and GFP HEK Cells

We then investigated if the K5 peptide could enhance Cas9 RNP editing in cells. Ai9 NIH 3T3 cells were used as model cells to measure the tdTomato-positive rate to determine the Cas9 RNP editing efficiency. We found that Ai9 NIH 3T3 cells treated with Cas9 RNP (166 µg mL^{-1}) were merely 0.183% tdTomato-positive, whereas Cas9-K5 RNP-treated cells (166 µg mL^{-1}) were 1.98% tdTomato-positive, which represents approximately a tenfold increase in editing efficiency (see Figure 4d; see Figure S9, Supporting Information, for detailed flow cytometry histograms). We further confirmed the enhanced editing in GFP-expressing HEK cells, using a sgRNA designed to knock out the GFP gene via indel mutations. Gene editing efficiency was calculated by subtracting the percentage of GFP-negative cells in the untreated cells from the percentage of GFP-negative cells in the treated cells. Figure 4e demonstrates that the K5 peptide also improved the delivery of the Cas9 RNP in GFP HEK cells. GFP HEK cells treated with the Cas9 RNP (166 µg mL^{-1}) were 3.12% GFP-negative, whereas GFP HEK cells treated with the Cas9-K5 RNP (166 µg mL^{-1}) were 4.33% GFP-negative, a 39% increase in editing efficiency (see Figure S10, Supporting Information, for detailed flow cytometry histograms). These results show that the K5 peptide can enhance the intracellular delivery of gene editing enzymes.

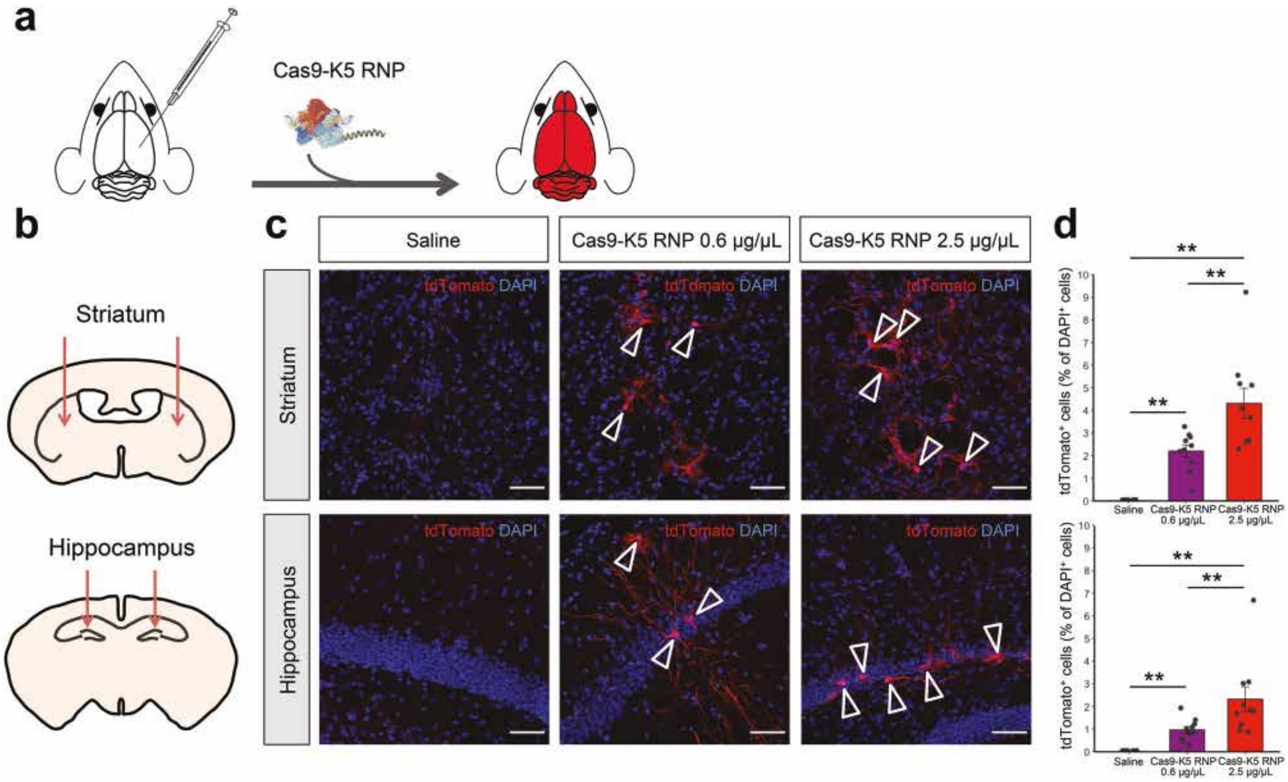

Figure 5. The Cas9-K5 RNP can edit the brains of Ai9 mice after an intracranial injection. a) Cas9 is fused to K5 and injected into the brains of Ai9 mice, and was able to edit neurons and astrocytes in the brain after an intracranial injection. b) Schematic showing the injection site in either the striatum or hippocampus of adult Ai9 mice. Saline or Cas9-K5 RNP (0.6 or 2.5 µg μL^{-1}) was injected into the striatum (AP: 0.50 mm, ML: ±1.87 mm, DV: −3.47 mm) or the hippocampus (AP: −2.56 mm, ML: ±1.55 mm, DV: −2.00 mm) of Ai9 mice. c) tdTomato (red) immunostaining and DAPI (blue) nuclear staining were performed 21 days after the saline or Cas9-K5 RNP (0.6 or 2.5 µg μL^{-1}) injection. Scale bar represents 50 µm. d) Quantification of the percentage of tdTomato$^+$ cells among DAPI$^+$ cells in the striatum (permutation one-way ANOVA: $F_{(2,27)} = 27.03$, $p < 0.001$) and hippocampus (permutation one-way ANOVA: $F_{(2,27)} = 12.93$, $p < 0.001$). Mean ± SEM, $n = 10$, $^{**}p < 0.01$ by post hoc permutation *t*-test. Post hoc *p* values were calculated between control (saline) and Cas9-K5 RNP 0.6 and 2.5 µg μL^{-1}, respectively, or Cas9-K5 RNP 0.6 µg μL^{-1} and Cas9-K5 RNP 2.5 µg μL^{-1}.

2.5. The Cas9-K5 RNP Can Edit Genes in the Striatum and Hippocampus of Ai9 Mice In Vivo

Given that our results demonstrate that K5 fusion to Cas9 RNP leads to enhanced gene editing in various cell types (see Figure 4d,e), we further tested the gene editing efficiency of the Cas9-K5 RNP in vivo. To test our idea of whether Cas9-K5 RNP could deliver and edit genes in vivo, we stereotaxically injected Cas9-K5 RNP into the brains of adult Ai9 mice (see **Figure 5**a). The Ai9 mouse is a genetically engineered mouse model, which has a fluorescent tdTomato gene containing loxP-flanked STOP cassettes upstream of it.[41] As mentioned earlier, the deletion of the STOP sequences allows transcription of the tdTomato gene, resulting in fluorescence expression (see Figure 5a). The sgRNA used for these experiments was designed to remove the STOP sequences, and was verified in Ai9 NIH 3T3 cells (see Figure 4d). Cas9 RNP or Cas9-K5 RNP or saline were stereotaxically injected into two brain regions, the hippocampus and the striatum, of 2–4 month old adult Ai9 mice as shown in Figure 5b, and the expression of tdTomato was measured via fluorescence histology. The gene editing efficiency was determined by detecting tdTomato-positive (tdTomato$^+$) cells normalized by total cell number (DAPI$^+$). Figure 5c,d demonstrates that Cas9-K5 RNP can efficiently edit cell genomes after stereotaxic intracerebral injection in both striatum and hippocampus, while control (saline-treated brain hemisphere) did not show edited cells. We treated two dosages (0.6 and 2.5 µg μL^{-1}) of Cas9-K5 RNP; the efficiency was significantly increased by higher dosage injection (2.5 µg μL^{-1}) compared to lower dosage injection (0.6 µg μL^{-1}), ≈2-fold increase in striatum (≈2% : ≈4%) and ≈2.5-fold increase in hippocampus (≈1% : ≈2.5%). These results indicate that Cas9-K5 RNP edited brain cells and that the gene editing efficiency was dose-dependently increased. Notably, when we counted the total number of cells (DAPI$^+$) by DAPI nuclear staining, we did not see a significant difference in total DAPI-positive cell numbers, in comparison to the saline-treated group, in either the low or high dosages, demonstrating that the Cas9-K5 has no significant impact on cell numbers (see Figure S11, Supporting Information).

2.6. The K5 Peptide Edits Neurons and Astrocytes in the Striatum and Hippocampus of Ai9 Mice In Vivo

Whereas neurons are the primary working units of the brain, non-neuronal cells also play important roles in brain function by maintaining, supporting, and regulating neuronal functions.

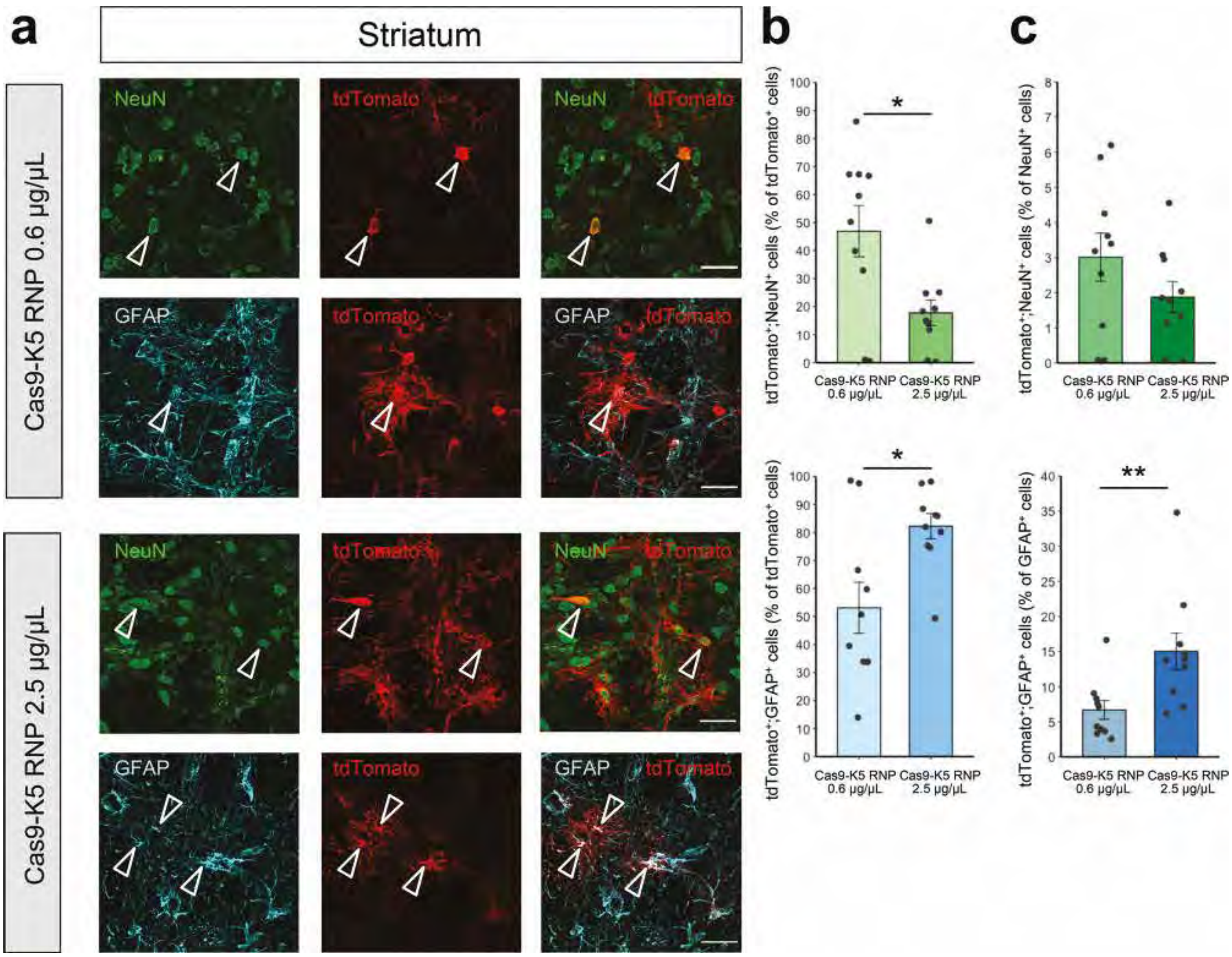

Figure 6. The cell specificity of Cas9-K5 RNP edited cells in the striatum of Ai9 mice. a) Immunostaining of tdTomato^+ (red) and either NeuN^+ (green) or GFAP^+ (cyan) cells 21 days after stereotaxic injection of Cas9 K5 RNP. Scale bar represents 30 µm. b,c) Quantification of b) tdTomato^+;NeuN^+ or tdTomato^+;GFAP^+ cells among total tdTomato^+ cells (%); c) tdTomato^+;NeuN^+ or tdTomato^+;GFAP^+ cells among total NeuN^+ or GFAP^+ cells (%), respectively, in the Cas9-K5 RNP-injected area. Mean ± SEM, $n = 10$. $^*p < 0.05$, $^{**}p < 0.01$ by permutation t-test. p values were calculated between Cas9-K5 RNP 0.6 µg μL^{-1} and Cas9-K5 RNP 2.5 µg μL^{-1}.

There is great interest in editing the genes of both neuronal and glial cells, since along with neurons, glial cell dysfunction causes multiple brain disorders.[42] We further identified the brain cell types edited by Cas9-K5 RNP to determine the editing efficiency in both neurons and astrocytes of Ai9 mouse brains. Cas9-K5 RNP-injected Ai9 brain sections were stained with the following cell markers: neuronal nuclear protein (NeuN) and glial fibrillary acidic protein (GFAP) which identify the neuronal populations and astrocytes respectively in the histology sections. The colocalization of tdTomato-positive (tdTomato^+) cells with NeuN-positive (NeuN^+) or with GFAP-positive (GFAP^+) cells demonstrates that ≈47% and ≈53% among all edited cell populations (% of tdTomato^+ cell) are neurons and astrocytes respectively in the striatum (see **Figure 6**b; see Figure 6a for representative images) and ≈72% and ≈28% in the hippocampus (see **Figure 7**b; see Figure 7a for representative images) when we used lower dosage injection (0.6 µg μL^{-1}) of Cas9-K5 RNP. Notably, the % of astrocytes among edited cells increased by a higher dosage (2.5 µg μL^{-1}) injection of Cas9-K5 RNP compared to lower dosage (0.6 µg μL^{-1}), ≈1.5-fold increase in striatum (≈53% : ≈82%) and ≈2.5-fold in hippocampus (≈28% : ≈80%), while the % of neurons among edited cells decreased in striatum (≈47% : ≈18%) and in hippocampus (≈72% : ≈20%) (see Figure 6b for striatum and Figure 7b for hippocampus).

Next, we further determined the gene editing efficiency in each cell type in neuron and astrocyte by analyzing the edited neurons (tdTomato^+;NeuN^+) among neuronal populations (NeuN^+) and edited astrocytes (tdTomato^+;GFAP^+) among astrocyte populations (GFAP^+). As a result, we found that gene editing efficiency in neurons ranges from ≈1.3% to ≈3% in striatum and hippocampus, and did not show any significant increased gene editing efficiency by higher dosage (see the upper graphs of Figure 6c for striatum and Figure 7c for hippocampus; see Figure S12, Supporting Information, for non-normalized raw values). Notably, the gene editing efficiency in astrocytes increased significantly by ≈2.1-fold in striatum (≈7% : ≈15%) and ≈4.5-fold

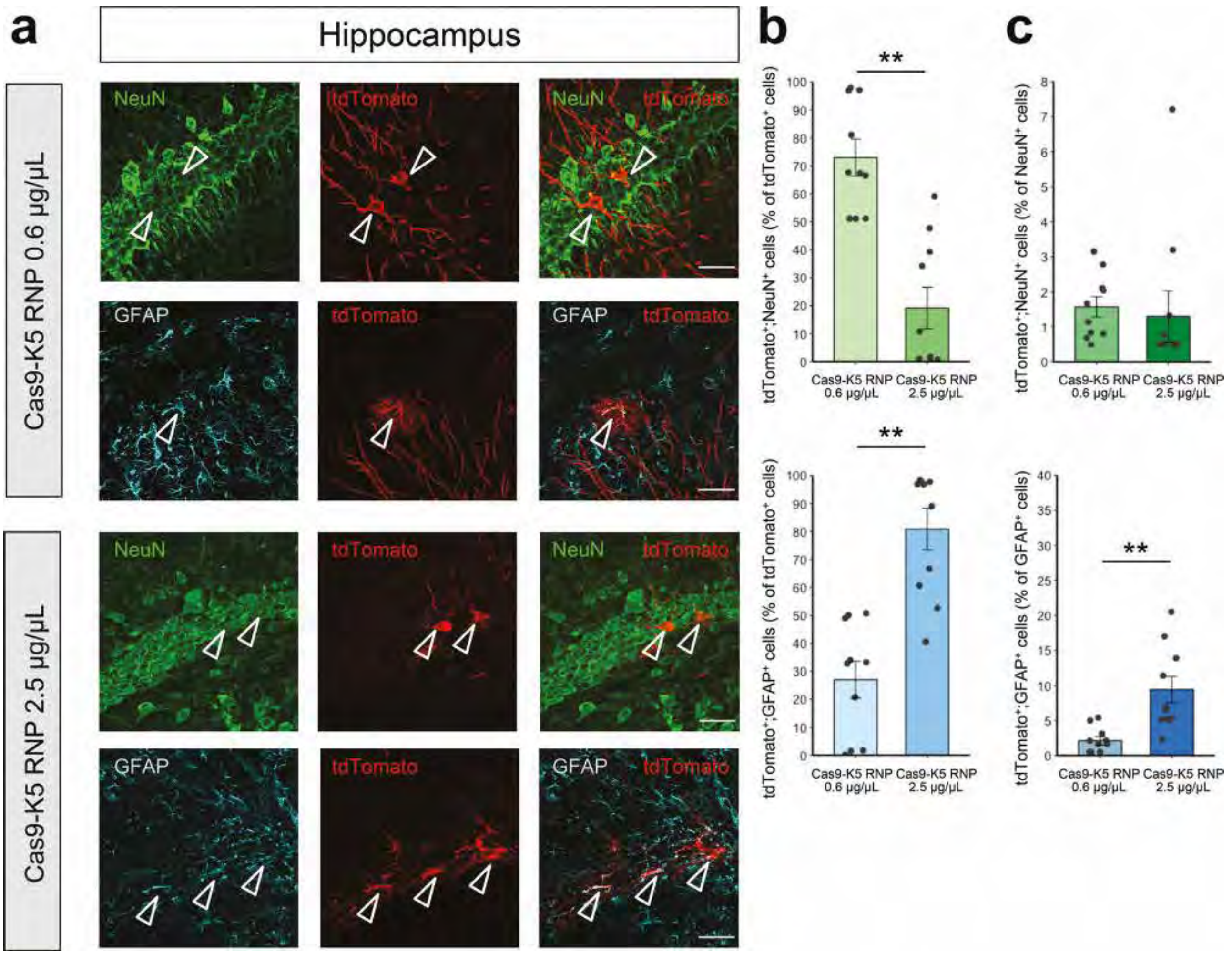

Figure 7. The cell specificity of Cas9-K5 RNP edited cells in the hippocampus of Ai9 mice. a) Immunostaining of tdTomato^+ (red) and either NeuN^+ (green) or GFAP^+ (cyan) cells 21 days after stereotaxic injection of Cas9 K5 RNP. Scale car represents 30 μm. b,c) Quantification of b) tdTomato^+;NeuN^+ or tdTomato^+;GFAP^+ cells among total tdTomato^+ cells (%); c) tdTomato^+;NeuN^+ or tdTomato^+;GFAP^+ cells among total NeuN^+ or GFAP^+ cells (%), respectively, in the Cas9-K5 RNP-injected area. Mean ± SEM, $n = 10$. $^{**}p < 0.01$ by permutation t-test. p values were calculated between Cas9-K5 RNP 0.6 μg μL^{-1} and Cas9-K5 RNP 2.5 μg μL^{-1}.

in hippocampus (≈2% : ≈9%) by a higher dosage injection of Cas9-K5 RNP compared to lower dosage (see the lower graphs of Figure 6c for striatum and Figure 7c for hippocampus; see Figure S12, Supporting Information, for non-normalized raw values). There was a minor increase (less than 1.5-fold) of total astrocyte number by higher dosage treatment of Cas9-K5 RNP both in striatum and hippocampus while no significant total neuron number change was observed (see Figure S13, Supporting Information).

Altogether, our results implicate that higher dosage of Cas9-K5 RNP may provide advantages when targeting astrocytes. On the other hand, neuronal gene editing efficiency was capped or saturated and did not significantly benefit by a higher dosage of Cas9-K5 RNP. This information may enable strategies for targeting brain cell types in the future with Cas9-K5. Gene editing in the brain with Cas9-K5 RNP was significantly lower in efficiency than gene editing with AAV, which usually generates 20–30% cell infection rates in the brain.[43] However, the Cas9-K5 RNP can be treated into patients multiple times, whereas AAV-based therapies cannot, and this may compensate for their lower efficiencies.

2.7. Cas9-K5 Can Complex Proteins that Contain Its E5 Counterpart

Hetero- or homo-oligomerization of proteins by coiled-coil interactions has shown great potential for use in biotechnology, bioengineering, and cell-based therapeutic applications.[44] We therefore further investigated if our K5-fused protein is capable of complexing proteins that contained its E5 counterpart $(\text{EVSALEK})_5$. We fused the E5 peptide to EGFP and mixed it with Cas9-K5, to investigate if Cas9-K5 could complex other proteins (see **Figure 8**). As shown by agarose gel electrophoresis in Figure 8, free EGFP-E5 migrates through the agarose gel, due to its negative charge, and can be directly visualized via its fluorescence. In contrast, EGFP-E5 mixed with Cas9-K5 has a very

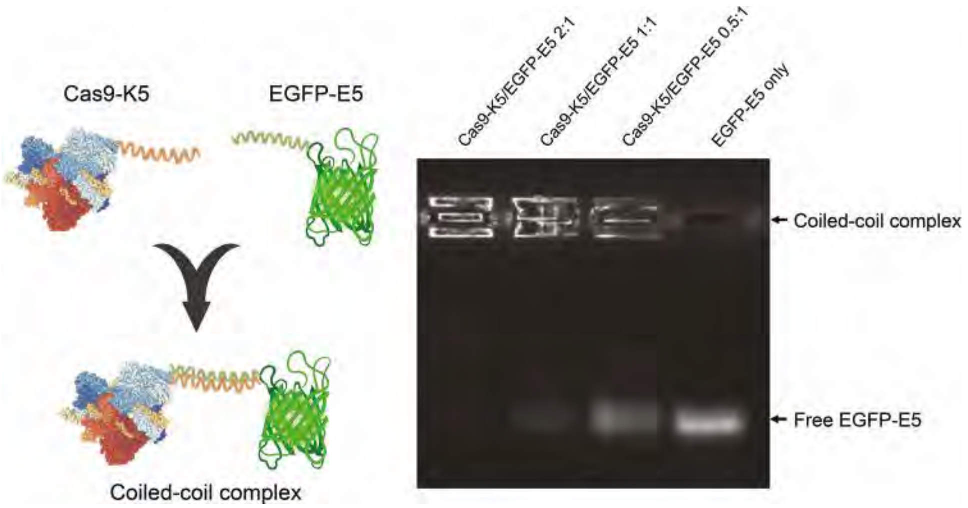

Figure 8. Cas9-K5 can complex EGFP-E5. Complexation of EGFP-E5 with Cas9-K5 at different molar ratios. Cas9-K5 is able to complex with EGFP-E5 as shown by agarose gel electrophoresis.

different gel migration pattern, and the mobility of the EGFP-E5 was retarded after complexation with Cas9-K5. In addition, the inhibitory effect of the Cas9-K5 was dose-dependent and high Cas9-K5 to EGFP-E5 molar ratios, completely inhibited EGFP-E5 from migrating into the gel. Additional control experiments were also performed to investigate if the E5 and K5 sequences were essential for mediating complexation between Cas9 and EGFP. Figure S14, Supporting Information, demonstrates that complexation between Cas9 and EGFP was dependent upon the E5 and K5 sequences. These results demonstrate the great potential of K5/E5 interactions to direct the formation of multicomponent complexes of precisely defined stoichiometry and will allow the introduction of different delivery functionalities into protein complexes.

3. Conclusions

The development of highly efficient CPPs that can be fused to proteins remains a central problem in the field of drug delivery. Although a variety of peptides have been used to enhance the delivery of GFP, these peptides have not been investigated for more challenging proteins such as Cas9 and have also rarely been investigated in vivo. Consequently, there is still a great need for developing new CPPs. The peptide $(KVSALKE)_x$ and its analogues has been used by numerous laboratories to assemble proteins together via coiled-coil interactions. However, the ability of coiled-coil forming peptides to enhance the delivery of proteins into cells has never been investigated. In this report, we demonstrate that the peptide $(KVSALKE)_5$ could enhance the delivery of either GFP or Cas9 RNP into cells and in vivo. Coiled-coil forming peptides have several advantages as CPPs. In particular, the K5 peptide forms an amphiphilic alpha-helix, which generates a hydrophobic surface and a cationic surface, which should enable efficient membrane binding and potentially membrane partitioning and endosomal disruption. The K5 peptide was able to enhance the delivery of the Cas9 RNP into Ai9 fibroblasts and also was effective at editing a variety of cells in the brain after a direct intracranial injection. The K5 peptide did lower the activity of the Cas9 RNP, and appears to be the largest repeat tolerated by the Cas9 RNP. For example, Cas9 fused to $(KVSALKE)_7$ and $(KVSALKE)_9$ both had minimal amounts of enzymatic activity (see Figure S15, Supporting Information,). We anticipate numerous applications of the K5 peptide given its ability to enhance cell uptake, broad cell tropism, and ability to complex other proteins.

4. Experimental Section

Materials: Oligonucleotides were purchased from Integrated DNA Technologies (IDT, Coralville, IA). Phusion High-Fidelity DNA Polymerase was purchased from NEB (Ipswich, MA). Mini-PROTEAN TGX Gels (4–20%) were purchased from Bio-Rad (Hercules, CA). Cas9 proteins were purchased from Macrolab UC Berkeley. BFP HEK cells and GFP HEK cells were a generous gift from GenEdit.[45] NIH 3T3 cells or HeLa cells were obtained from UC Berkeley Cell Culture Facility. Ai9 NIH 3T3 cells were a generous gift from Craig Duvall's lab.[40] Paraformaldehyde (PFA, cat. #: 41678-0010) and D(+)-Sucrose (cat. #: 177140010) were purchased from Acros Organics; phosphate buffered saline (PBS, cat. #: BP 399-4), sodium citrate (cat. #: BP 327–500), and Tween 20 (cat. #: 9005-64-5) from Fisher BioReagents; Superfrost Plus Microsope Slides (cat. #: 12-550-15) and Tissue-Plus O.C.T. Compound from Fisher Healthcare; isoflurane from Vetone; ProLong Gold Antifade Reagent from Molecular Probes; embedding molds from Thermo Scientific; Goat Serum from Gibco; DAPI (4′,6-diamidino-2-phenylindole), DMEM media, non-essential amino acids, penicillin–streptomycin, dPBS, and Accutase were purchased from Invitrogen (Carlsbad, CA).

Antibodies: The rabbit polyclonal RFP antibody was purchased from Rockland (cat. #: 600-401-379), the mouse monoclonal NeuN antibody (cat. #: MAB377) from Millipore (Burlington, MA), and the chicken polyclonal GFAP antibody from EnCor (cat. #: CPCA-GFAP). The donkey anti-rabbit IgG-Cy3 (cat. #: 711-165-152), donkey anti-mouse IgG-Alexa Fluor 647 (cat. #: 715-605-151), and donkey anti-chicken IgY-Cy2 (cat. #: 703-225-155) were purchased from Jackson ImmunoResearch Laboratories, Inc. (West Grove, PA).

Animal Care and Use: Ai9 mice (in C57BL/6J background) were obtained from Jackson Laboratory (stock #007909). The use and care of animals in this study follow the guidelines of the UTHSCSA and UC Berkeley Institutional Animal Care and Use Committee.

Protein Expression: $(KVSALKE)_5$ (K5)-, $(KVSALKE)_7$ (K7)-, or $(KVSALKE)_9$ (K9)-fused *Streptococcus pyogenes* Cas9 (Cas9-K5, Cas9-K7, or Cas9-K9) was expressed from an expression vector that was previously published in the manuscript by Jinek et al.[46] It was composed of a custom pET-based expression vector encoding an N-terminal 6His-tag followed by the maltose-binding protein and a TEV protease cleavage site followed by K5 sequence, as well as two SV40 NLS peptides at its C-terminus. Recombinant Cas9-K5, Cas9-K7, or Cas9-K9 protein was expressed in the *E. coli* strain BL21 (DE3)[46] (UC Berkeley MacroLab) and further purified to homogeneity as previously described. Purified Cas9 protein was stored in 50 mM HEPES at pH 7.5 with 300 mM NaCl, 10% glycerol, and 100 µM TCEP at −80 °C. Cas9-K5, Cas9-K7, or Cas9-K9 protein concentration was determined by a NanoDrop 2000 (Thermo Scientific) from the absorbance at 280 nm. K5 or E5 $(\mathrm{EVSALEK})_5$-fused EGFP (EGFP-K5 or EGFP-E5) was expressed from pET-based vector encoding an N-terminal 6His-tag followed by EGFP and K5 or E5 sequence on the C terminus. Recombinant EGFP-K5 and EGFP-E5 protein was expressed in *E. coli* strain BL21 (DE3) (UC Berkeley MacroLab) and further purified by HisTrap HP (Cytiva). Cas9 RNP formation was conducted by mixing Cas9, Cas9-K5, Cas9-K7, or Cas9-K9 protein with sgRNA at a molar ratio of 1:1.2 and incubated on ice for 15 min before use. sgRNA sequences used in this paper were as below:

BFP and GFP sgRNA targeting sequence: GCTGAAGCACTGCACGCCAT
Ai9 sgRNA targeting sequence: AAGTAAAACCTCTACAAATG

For coiled-coil complexation studies, a 1 mg mL^{-1} solution of Cas9-K5 (or Cas9) was mixed with a 1 mg mL^{-1} solution of EGFP-E5 (or EGFP) at different molar ratios (2:1, 1:1, 1:2) and incubated at room temperature for 20 min. The resulting complexes were run on an agarose gel for coiled-coil interaction analysis.

Cell Culture: Ai9 NIH 3T3 cells, NIH 3T3 cells, HeLa cells, BFP HEK cells, and GFP HEK cells were cultured in DMEM supplemented with 10% fetal bovine serum (Gibco) and 1% penicillin–streptomycin and maintained at 37 °C in a humidified incubator (Thermo Electron Corporation) containing 5% CO_2. When the cells reached 80% confluency, they were passaged using Accutase solution; media was changed every 2–3 days.

Cell Internalization Studies: Studies of intracellular delivery with EGFP and Cas9 RNP were achieved using fluorescence microscopic technique and fluorescence-activated cell sorting. NIH 3T3 cells or HeLa cells were seeded in 96 well plates at a density of 10 000 per well the day before exposing to samples. EGFP-K5 and ATTO 550-labeled Cas9-K5 RNP or their native forms were added into the cell cultures. After incubation at 37 °C for 4 h, the cells were washed three times with PBS and either visualized with a fluorescent microscope EVOS M5000 (Invitrogen) or analyzed via Attune NxT flow cytometer (Invitrogen).

Cas9 RNP Nucleofection and Cas9 RNP Transfection: For nucleofection, cells were detached using Accutase, spun down at 600 × g for 3 min and washed with PBS. Nucleofection was conducted using a Lonza 4D-Nucleofector system with SE Cell Line 4D-Nucleofector X Kit following the manufacturer's protocol. Briefly, 200 000 Ai9 NIH 3T3 cells or BFP HEK cells were suspended in 20 µL SE buffer containing Cas9 RNPs (31.25 pmole of Cas9, 37.5 pmole of sgRNAs) and transfected using the EN-158 or CM-130 Lonza program. After nucleofection, cells were spun down at 600 × g and resuspended in 500 µL fresh DMEM medium supplemented with 10% FBS and 1% penicillin–streptomycin and incubated at 37 °C in tissue culture plates for 5 days before flow cytometry analysis.

For direct transfection studies, 100 µL of Opti-MEM (Gibco) containing Cas9 RNP or Cas9-K5 RNP (16.6 µg Cas9 or Cas9-K5) was added to Ai9 NIH 3T3 cells or GFP HEK cells. The cells were transfected for 48 h at 37 °C in a humidified incubator containing 5% CO_2 and replaced with fresh DMEM medium supplemented with 10% FBS and 1% penicillin–streptomycin. Td-tomato signals or the GFP signals were analyzed by Attune NxT flow cytometer (Invitrogen) after another 24 or 72 h. Gene editing efficiency was determined by the percentage of Td-tomato positive cells or GFP negative cells.

In Vitro Cleavage Assays: The Ai9 template was PCR amplified (forward: TGCTATACGAAGTTATTCGC reverse: GACAAACCACAACTAGAATG) from synthesized Ai9 DNA (ATGTATGCTATACGAAGTTATTCGCGATGAATAAATGAAAGCTTGCAGATCTGCGACTCTAGAGGATCTGCGACTCTAGAGGATCATAATCAGCCATACCACATTTGTAGAGGTTTTACTTGCTTTAAAAAACCTCCCACACCTCCCCCTGAACCTGAAACATAAAATGAATGCAATTGTTGTTGTTAACTTGTTTATTGCAGCTTATAATGGTTACAAATAAAGCAATAGCATCACAAATTTCACAAATAAAGCATTTTTTTCACTGCATTCTAGTTGTGGTTTGTCCAAACTCATCAATGTATCTTATCATGTCT). For in vitro cleavage assays, 500 ng of template DNA was incubated with 500 ng (or as indicated in each Figure) of Cas9 RNP, Cas9-K5 RNP, Cas9-K7 RNP, or Cas9-K9 RNP with sgRNA targeting the Ai9 sequence in 10 µL 1× Cutsmart buffer (NEB) and incubated at 37 °C for 4 h. Gel electrophoresis was performed to verify cleavage of the template.

Stereotaxic Injection: Male and female Ai9 (Cre-dependent tdTomato reporter) mice aged 2–3 months were used in this study. Mice were anaesthetized using isoflurane (4% for induction and 2% for maintaining) and bilaterally injected with saline (left hemisphere) and Cas9-K5 RNP (right hemisphere) into the striatum (AP: 0.50 mm, ML: ±1.87 mm, DV: −3.47 mm) and hippocampus (AP: −2.56 mm, ML: ±1.55 mm, DV: −2.00 mm). Either saline or Cas9-K5 RNP (final concentrations per injection: 0.6 or 2.5 µg µL^{-1}) were infused with 1.5 µL per injected site (0.5 µL min^{-1}) using a Hamilton Neuros syringe. After the infusion, the injector was left at the injection site for 5 min and then slowly withdrawn. A period of 21 days was given before the perfusion and immunostaining procedures. The use and care of animals in this study followed the guidelines of the UTHSCSA.

Immunostaining: 21 days after stereotaxic injection, the mice were anaesthetized by isoflurane and were perfused with ice-cold PBS followed by 4% PFA in PBS. The brains were postfixed for 4 h in 4% PFA, washed once with PBS, and then cryoprotected by 30% sucrose in PBS at 4 °C for 2–3 days. After cryoprotection, the brains were embedded in O.C.T. compound, frozen, and then stored at −80 °C until next processing. Mouse brain sections were obtained by cryostat (CM3050S; Leica Microsystems). Slices with striatum and hippocampus were cryosectioned on the coronal plane at 20 µm, mounted on glass slides, and stored at −20 °C. The sections to be immunostained were washed three times in PBS. Antigen retrieval was performed by steaming in a citrate buffer (0.294% sodium citrate, 0.05% Tween 20 in distilled water, pH 6.0) for 15 min with subsequent cooling over ice for 10 min. The sections were rinsed in PBS and blocked (5% goat serum, 0.2% Triton X-100 in PBS) at room temperature for 1 h. The sections were next incubated in the same blocking solution with primary antibodies (1:500 rabbit anti-RFP, 1:500 mouse anti-NeuN, 1:1000 chicken anti-GFAP) overnight at 4 °C. The sections were washed four times in PBS before incubation with secondary antibodies (1:500 Cy3-conjugated donkey anti-rabbit, 1:500 Alexa Fluor 647-conjugated donkey anti-mouse, 1:500 Cy2-conjugated donkey anti-chicken) for 2 h. After the incubation with secondary antibodies the sections were washed four times in PBS, and then incubated with DAPI diluted in PBS (1:1500 of 5 µg µL^{-1} stock solution) for 10 min. Next,the sections were washed three times in PBS and mounted with Prolong Gold Antifade Reagent and imaged using a Zeiss Axio Observer 7 microscope with 20× and 40× objective, respectively, and captured with camera Axiocam 503 mono (Carl Zeiss Microscopy GmbH).

Image Analysis: Quantification of gene editing efficiency in Ai9 mice was performed in a defined ROI, which was the same for all animals in striatum and hippocampus, respectively. Each injected brain area was analyzed from five images taken as a z-stack (10 µm) with the same magnification (40×) and same exposure times. The total number of tdTomato$^+$, DAPI$^+$, NeuN$^+$, and GFAP$^+$ cells was counted using the Cell counter plugin for ImageJ software (NIH). To determine the percentage of edited cells (tdTomato$^+$) or to present the number of DAPI$^+$ cells in Ai9 mice, tdTomato$^+$ cells were counted and normalized against the number of DAPI$^+$ cells or the number of DAPI$^+$ cells were presented itself (analyzed from a defined ROI, which was the same size for all images analyzed for comparison). To determine the percentage of cell types among edited cells, NeuN$^+$ or GFAP$^+$ cells were counted in only tdTomato$^+$ cells. The percentage of the tdTomato$^+$ cells among the each cell type (neuron or astrocytes) was also analyzed by counting NeuN$^+$ or GFAP$^+$ cells costained with tdTomato among the total NeuN$^+$ or GFAP$^+$ cells. Each cell marker was stained with tdTomato and analyzed independently. The percentage of tdTomato$^+$ and total number of DAPI$^+$ cells among saline and Cas9-K5 RNP (0.6 and 2.5 µg µL^{-1})-injected brain areas were evaluated. The effect of Cas9-K5 RNP concentration (0.6 vs 2.5 µg µL^{-1}) on the cell specificity, total number of edited neurons (tdTomato$^+$;NeuN$^+$) or astrocytes (tdTomato$^+$;GFAP$^+$), as well as total number of all edited cells (tdTomato$^+$) in the striatum and hippocampus were also analyzed.

Statistical Analysis: All in vitro experimental raw data were acquired in at least three independent experiments and presented as mean ± SEM. An unpaired two-tailed t-test was performed to evaluate statistical significance between two groups. $p < 0.05$ was considered significant. The statistical analyses were performed using GraphPad Prism 6. For in vivo experiment two animals (male and female) per group were used. The statistical analyses were conducted with data acquired from a total of five images per animal, a total of ten images per group ($n = 10$). All data were presented as mean ± SEM. The statistical analysis of multiple-group comparison was performed using one-way permutation ANOVA with maximum of 5000 permutations. The post hoc between-group comparisons were evaluated using two-tailed permutation t-test with 10 000 permutations. Significance level was defined as $p < 0.05$. Statistical analyses were conducted using lmPerm and RVAideMemoire packages for R version 3.6.0.

Supporting Information

Supporting Information is available from the Wiley Online Library or from the author.

Acknowledgements

J.L. and J.T. contributed equally to this work. This work was supported by the National Institute of Mental Health (R01MH125979) funded to H.Y.L. and N.M. This work was also supported by the UT Rising STARs award, the Simons Foundation Autism Research Initiative (SFARI) pilot award (#574967), and R21AG072423 funded to H.Y.L, and R61DA048444, U24HG010423, 1UM1AI164559, R01EB023776, UG3NS115599, and Bakar Fellows Spark Award funded to N.M.

Conflict of Interest

The authors declare no conflict of interest.

Data Availability Statement

Research data are not shared.

Keywords

Cas9, cell penetrating peptides, gene editing, neuroscience, nonviral delivery, protein fusions

Received: October 4, 2021
Revised: November 23, 2021

---

[1] J. R. Kintzing, M. V. F. Interrante, J. R. Cochrane, *Trends Pharmacol. Sci.* **2016**, *37*, 993.
[2] S. S. Usmani, G. Bedi, J. S. Samuel, S. Singh, S. Kalra, P. Kumar, A. A. Ahuja, M. Sharma, A. Gautam, G. P. S. Raghava, *PLoS One* **2017**, *12*, e0181748.
[3] H. A. Lagasse, A. Alexaki, V. L. Simhadri, N. H. Katagiri, W. Jankowski, Z. E. Sauna, C. Kimchi-Sarfaty, *F1000Research* **2017**, *6*, 113.
[4] J. Caravella, A. Lugovskoy, *Curr. Opin. Chem. Biol.* **2010**, *14*, 520.
[5] B. Leader, Q. J. Baca, D. E. Golan, *Nat. Rev. Drug Discovery* **2008**, *7*, 21.
[6] M. Di Marco, S. Shamsuddin, K. A. Razak, A. A. Aziz, C. Devaux, E. Borghi, L. Levy, C. Sadun, *Int. J. Nanomed.* **2010**, *5*, 37.
[7] M. Ray, Y. W. Lee, F. Scaletti, R. Yu, V. M. Rotello, *Nanomedicine* **2017**, *12*, 941.
[8] M. P. Stewart, R. Langer, K. F. Jensen, *Chem. Rev.* **2018**, *118*, 7409.
[9] Y. M. Zhang, J. J. Roise, K. Lee, J. Li, N. Murthy, *Curr. Opin. Biotechnol.* **2018**, *52*, 25.
[10] B. Gupta, T. S. Levchenko, V. P. Torchilin, *Adv. Drug Delivery Rev.* **2005**, *57*, 637.
[11] M. Chiper, K. Niederreither, G. Zuber, *Adv. Healthcare Mater.* **2018**, *7*, e1701040.
[12] C. Lonez, M. Vandenbranden, J. M. Ruysschaert, *Adv. Drug Delivery Rev.* **2012**, *64*, 1749.
[13] J. M. Ruysschaert, C. Lonez, *Biochim. Biophys. Acta, Biomembr.* **2015**, *1848*, 1860.
[14] S. Fawell, J. Seery, Y. Daikh, C. Moore, L. L. Chen, B. Pepinsky, J. Barsoum, *Proc. Natl. Acad. Sci. USA* **1994**, *91*, 664.
[15] T. Barka, E. W. Gresik, H. van der Noen, *J. Histochem. Cytochem.* **2000**, *48*, 1453.
[16] J. S. Wadia, R. V. Stan, S. F. Dowdy, *Nat. Med.* **2004**, *10*, 310.
[17] T. Gaj, J. Guo, Y. Kato, S. J. Sirk, C. F. Barbas 3rd, *Nat. Methods* **2012**, *9*, 805.
[18] S. G. Patel, E. J. Sayers, L. He, R. Narayan, T. L. Williams, E. M. Mills, R. K. Allemann, L. Y. P. Luk, A. T. Jones, Y. H. Tsai, *Sci. Rep.* **2019**, *9*, 6298.
[19] B. T. Staahl, M. Benekareddy, C. Coulon-Bainier, A. A. Banfal, S. N. Floor, J. K. Sabo, C. Urnes, G. A. Munares, A. Ghosh, J. A. Doudna, *Nat. Biotechnol.* **2017**, *35*, 431.
[20] Y. J. Chen, Q. W. Deng, L. Wang, X. C. Guo, J. Y. Yang, T. Li, Z. Xu, H. C. Lee, Y. J. Zhao, *Chem. Commun.* **2021**, *57*, 1434.
[21] C. Li, X. W. Cao, J. Zhao, F. J. Wang, *J. Membr. Biol.* **2020**, *253*, 139.
[22] P. Lonn, S. F. Dowdy, *Expert Opin. Drug Delivery* **2015**, *12*, 1627.
[23] A. Bernkop-Schnurch, *Adv. Drug Delivery Rev.* **2018**, *136*, 62.
[24] J. J. Cronican, D. B. Thompson, K. T. Beier, B. R. McNaughton, C. L. Cepko, D. R. Liu, *ACS Chem. Biol.* **2010**, *5*, 747.
[25] N. Nischan, H. D. Herce, F. Natale, N. Bohlke, N. Budisa, M. C. Cardoso, C. P. R. Hackenberger, *Angew. Chem., Int. Ed.* **2015**, *54*, 1950.
[26] S. Ramakrishna, A. B. K. Dad, J. Beloor, R. Gopalappa, S. K. Lee, H. Kim, *Genome Res.* **2014**, *24*, 1020.
[27] G. L. Rosano, E. A. Ceccarelli, *Front. Microbiol.* **2014**, *5*, 172.
[28] G. De Crescenzo, J. R. Litowski, R. S. Hodges, M. D. O'Connor-McCourt, *Biochemistry* **2003**, *42*, 1754.
[29] N. BenTal, A. BenShaul, A. Nicholls, B. Honig, *Biophys. J.* **1996**, *70*, 1803.
[30] J. Seelig, *Biochim. Biophys. Acta, Biomembr.* **2004**, *1666*, 40.
[31] N. Nakayama, K. Hagiwara, Y. Ito, K. Ijiro, Y. Osada, K. Sano, *Langmuir* **2015**, *31*, 8218.
[32] M. Rabe, C. Aisenbrey, K. Pluhackova, V. de Wert, A. L. Boyle, D. F. Bruggeman, S. A. Kirsch, R. A. Bockmann, A. Kros, J. Raap, B. Bechinger, *Biophys. J.* **2016**, *111*, 2162.
[33] G. Pahler, C. Panse, U. Diederichsen, A. Janshoff, *Biophys. J.* **2012**, *103*, 2295.
[34] A. K. Gillingham, S. Munro, *Biochim. Biophys. Acta, Mol. Cell Res.* **2003**, *1641*, 71.
[35] E. Eiriksdottir, K. Konate, U. Langel, G. Divita, S. Deshayes, *Biochim. Biophys. Acta* **2010**, *1798*, 1119.
[36] R. Sauder, J. Seelig, A. Ziegler, in *Cell-Penetrating Peptides: Methods and Protocols* (Ed: U. Langel), Humana Press, New York, NY **2011**.
[37] A. Folska, L. Prevette, presented at 253rd Nat. Meeting (2017), San Francisco, CA, March **2017**.

[38] S. A. Bode, I. C. Kruis, H. P. J. H. M. Adams, W. C. Boelens, G. J. M. Pruijn, J. C. M. van Hest, D. W. P. M. Lowik, *ChemBioChem* **2017**, *18*, 185.

[39] Y. Assal, Y. Mizuguchi, M. Mie, E. Kobatake, *Bioconjugate Chem.* **2015**, *26*, 1672.

[40] B. C. Evans, R. B. Fletcher, K. V. Kilchrist, E. A. Dailing, A. J. Mukalel, J. M. Colazo, M. Oliver, J. Cheung-Flynn, C. M. Brophy, J. W. Tierney, J. S. Isenberg, K. D. Hankenson, K. Ghimire, C. Lander, C. A. Gersbach, C. L. Duvall, *Nat. Commun.* **2019**, *10*, 5012.

[41] L. Madisen, T. A. Zwingman, S. M. Sunkin, S. W. Oh, H. A. Zariwala, H. Gu, L. L. Ng, R. D. Palmiter, M. J. Hawrylycz, A. R. Jones, E. S. Lein, H. Zeng, *Nat. Neurosci.* **2010**, *13*, 133.

[42] A. A. Almad, N. J. Maragakis, *Stem Cell Res. Ther.* **2012**, *3*, 37.

[43] E. Hudry, L. H. Vandenberghe, *Neuron* **2019**, *101*, 839.

[44] T. Lebar, D. Lainscek, E. Merljak, J. Aupic, R. Jerala, *Nat. Chem. Biol.* **2020**, *16*, 513.

[45] K. Lee, M. Conboy, H. M. Park, F. Jiang, H. J. Kim, M. A. Dewitt, V. A. Mackley, K. Chang, A. Rao, C. Skinner, T. Shobha, M. Mehdipour, H. Liu, W. C. Huang, F. Lan, N. L. Bray, S. Li, J. E. Corn, K. Kataoka, J. A. Doudna, I. Conboy, N. Murthy, *Nat. Biomed. Eng.* **2017**, *1*, 889.

[46] M. Jinek, K. Chylinski, I. Fonfara, M. Hauer, J. A. Doudna, E. Charpentier, *Science* **2012**, *337*, 816.

European Journal of Immunology

Tissue immunology and leukocyte trafficking

Research Article

Analysis of lung stromal expression of the atypical chemokine receptor ACKR2 reveals unanticipated expression in murine blood endothelial cells

Christopher A.H. Hansell, Samantha Love, Marieke Pingen, Gillian J. Wilson, Megan MacLeod and Gerard J. Graham

Chemokine Research Group, Institute of Infection, Immunity and Inflammation, University of Glasgow, Glasgow G12 8TA, UK

Analysis of chemokine receptor, and atypical chemokine receptor, expression is frequently hampered by the lack of availability of high-quality antibodies and the species specificity of those that are available. We have previously described methodology utilizing Alexa-Fluor-labeled chemokine ligands as versatile reagents to detect receptor expression. Previously this has been limited to hematopoietic cells and methodology for assessing expression of receptors on stromal cells has been lacking. Among chemokine receptors, the ones most frequently expressed on stromal cells belong to the atypical chemokine receptor subfamily. These receptors do not signal in the classic sense in response to ligand but scavenge their ligands and degrade them and thus sculpt in vivo chemokine gradients. Here, we demonstrate the ability to use either intratracheal or intravenous, Alexa-Fluor-labeled chemokine administration to detect stromal cell populations expressing the atypical chemokine receptor ACKR2. Using this methodology, we demonstrate, for the first time, expression of ACKR2 on blood endothelial cells. This observation sets the lung aside from other tissues in which ACKR2 is exclusively expressed on lymphatic endothelial cells and suggest unique roles for ACKR2 in the pulmonary environment.

Keywords: ACKR2 · Alexa-Fluor labeling · Blood endothelial cells · Lung · Pulmonary immunity

Additional supporting information may be found online in the Supporting Information section at the end of the article.

Introduction

In vivo leukocyte migration is regulated, in the main, by proteins belonging to the chemokine family of chemotactic cytokines [1, 2]. This family is defined on the basis of a conserved cysteine motif in the mature sequence of its members and is divided into CC, CXC, XC, and CX3C subfamilies according to the specific configuration of this motif. The chemokine family arose early in vertebrate evolution [3] (prevertebrate species do not have chemokines) and the primordial chemokine was almost certainly CXCL12, which plays essential roles in stem cell migration during embryogenesis [4-9]. From this one chemokine and its receptor CXCR4, through gene duplication, the family has expanded to the point at which mammals have approximately 45 chemokines, and 18 signaling chemokine receptors, which together orchestrate in vivo homeostatic and inflammatory leukocyte migration. Chemokine regulation of cellular migration is extremely complex and, particularly in the case of inflammation [10], poorly understood, which

Correspondence: Dr. Gerard J. Graham
e-mail: gerard.graham@glasgow.ac.uk

has contributed to ongoing problems in therapeutically targeting inflammatory chemokine receptors in immune and inflammatory diseases [11].

In addition to signaling chemokine receptors that belong to the G-protein-coupled receptor family [12], chemokines also bind to a subfamily of atypical chemokine receptors (ACKRs), which are generally stromally expressed and which fine-tune in vivo chemokine activity by scavenging chemokines and therefore regulating chemokine availability [13-15]. There are currently four members of the ACKR family: ACKR1 (formerly known as DARC), ACKR2 (formerly known as D6), ACKR3 (formerly known as CXCR7), and ACKR4 (formerly known as CCX-CKR). With the exception of ACKR1, these receptors exhibit spontaneous internalization and recycling activity and scavenge chemokines from the environment and target them for lysosomal degradation. ACKR3 carries out this role in some essential developmental contexts and is strongly evolutionarily conserved [5, 6, 16, 17]. ACKR4 scavenges chemokines within the LN to generate intra-LN gradients and facilitate DC migration from the subcapsular sinus into the T-cell zone of the LN [18]. We have had a particular interest in ACKR2, which is the prototypic member of the ACKR family [19]. This receptor binds, internalizes, and degrades all inflammatory chemokines belonging to the CC-chemokine subfamily and thus plays an essential role in the resolution of the inflammatory response [20-24]. This has implications for tumorigenesis [25-28] as well as for branching morphogenesis in a number of developmental contexts [29, 30]. ACKR2 is predominantly expressed on lymphatic endothelial cells [31, 32] and placental trophoblasts [23, 33, 34] with expression also being detected on subsets of splenic B cells [35]. The ACKRs are therefore central regulators of chemokine activity in vivo.

One of the challenges in studying chemokine receptors, including ACKRs, is access to high-quality antibodies. While antibodies to some typical and atypical receptors are available, it has proven extremely difficult to raise useful antibodies to others. For example, there are no high-quality antibodies available for detection of murine ACKR2. A further issue is that even for receptors for which antibodies are available, these antibodies are invariably species specific and it is therefore difficult to carry out analyses in either nonmurine or nonhuman species. This is particularly important for highly conserved receptors such as ACKR3. The availability of a generic methodology to allow detection of ACKRs (and amenable to detection of typical receptors), which would be usable in vivo and applicable to numerous species, would therefore represent a significant technological development.

Here, we describe a novel methodology for the detailed analysis of the phenotypes of ACKR2-expressing cells in lung stroma. The technology is conceptually similar to that reported by Ameti and colleagues [36] and uses ACKR2-dependent internalization of a fluorescently tagged ligand to identify receptor expressing cells and we demonstrate the utility of comparing intratracheal and intravenous administration in defining, and discriminating between, discrete receptor expressing stromal cell types. Using this approach, we report, for the first time, robust expression of ACKR2 by pulmonary blood endothelial cells. This has not been reported in any other tissues and suggests unique roles for ACKR2 in lung function and pulmonary immunity.

Results

ACKR2 is stromally expressed in the lung

Data on ACKR2 expression profiles available through the Immgen database (www.immgen.org) reveal that the lung is the tissue with the highest expression (Supporting Information Fig. 1). We have previously described the versatile use of fluorescently labeled chemokines, instead of antibodies, to detect their cognate receptors using flow cytometry as a read out [35, 37-39]. We used this approach with Alexa-647-labeled CCL22 (a high-affinity ACKR2 ligand: Alexa-CCL22) uptake to detect ACKR2 in lung digests. Importantly, CCL22 also binds to the chemokine receptor CCR4 so to control for any contribution of this receptor to cellular CCL22 binding, and to confirm specific binding to ACKR2, we have included ACKR2$^{-/-}$ mice and tissues in all our analyses. Comparing CCL22 binding in WT and ACKR2$^{-/-}$ tissues and cells therefore allows us to specifically determine the expression patterns of ACKR2. Importantly, there are no differences in circulating levels of CCL22 between WT and ACKR2$^{-/-}$ mice, which might confound these analyses (Supporting Information Fig. 2). Further reasons for selecting CCL22 for this analysis include the fact that this ligand does not display the broad receptor binding profiles of other ACKR2 ligands and expression of CCR4 is more limited than the receptors that bind the other ACKR2 ligands [14]. Flow cytometric analysis of CD45^{+} cells from Alexa-CCL22-stained lung digests failed to detect any significant expression on CD45^{+} leukocytes in either WT or ACKR2$^{-/-}$ lungs (Fig. 1a). The exemplar flow cytometry plot shown in Fig. 1a(i) revealed a low level of Alexa-CCL22 binding to CD45^{+} cells in ACKR2$^{-/-}$ lung digests, which is not seen in WT digests. We did not see this routinely and repeated flow cytometric analyses (Fig. 1a(ii)) revealed essentially undetectable Alexa-CCL2 binding by either WT or ACKR2$^{-/-}$ CD45^{+} cells. These data, therefore, indicated that ACKR2 expression in the lung was predominantly stromal in origin. We used RNA sequencing to generate data on the transcriptional profile of FACS-sorted pulmonary stromal cell types at rest and over the course of an influenza infection to examine possible pathogen-driven alterations in expression. As shown in Fig. 1(b), ACKR2 expression was essentially undetectable in epithelial cells but was present at low levels in fibroblasts and at very high levels in blood endothelial cells. Expression did not vary significantly over the course of influenza infection. Examination of pulmonary ACKR2 expression by qPCR from embryonic day 13.5 to 9 weeks of age indicated that expression is low within the embryo but that it is markedly upregulated immediately after birth and presumably coincident with the onset of breathing. This increased level is maintained and increased as mice age (Fig. 1c).

Next, we tried to use the in vitro Alexa-CCL22 detection method to examine ACKR2 expression on nonleukocytic stromal cells

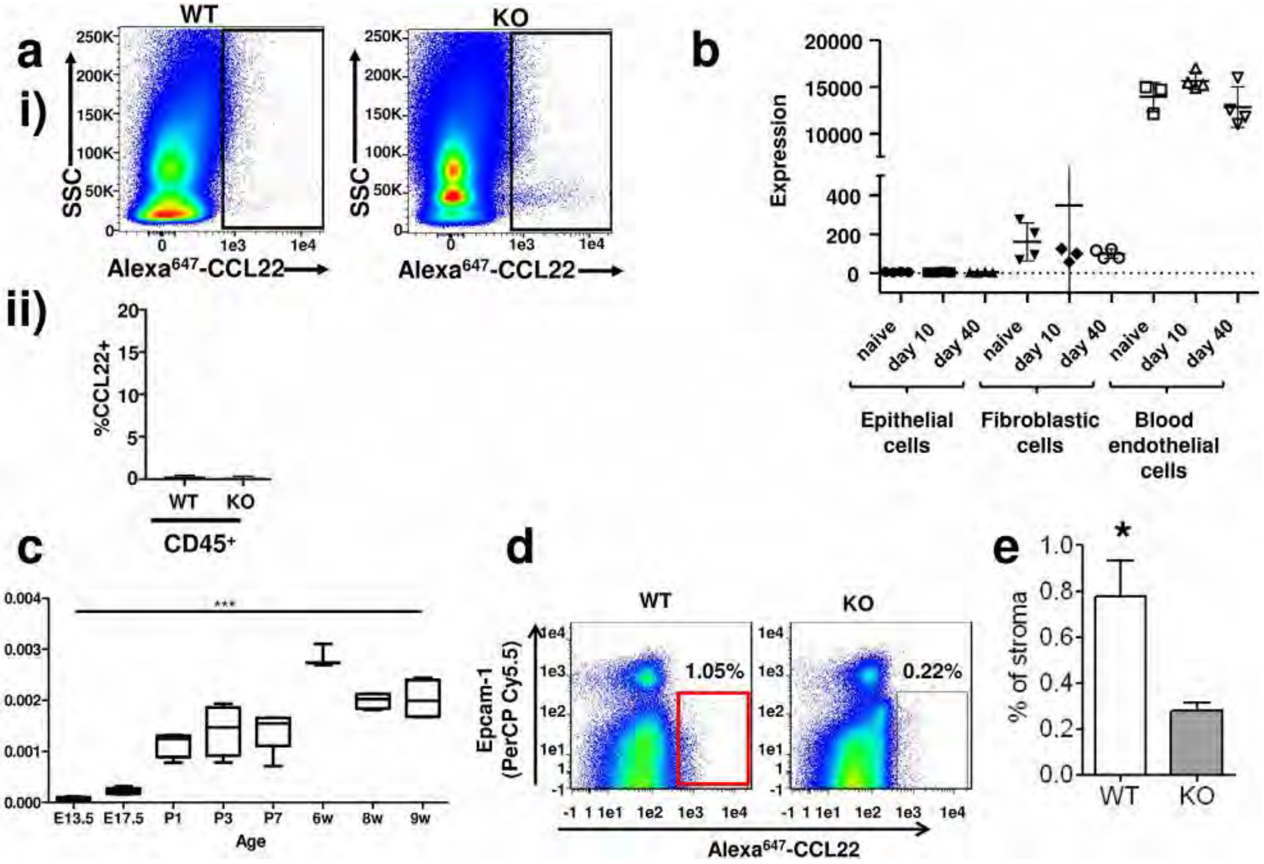

Figure 1. In vitro analysis of pulmonary ACKR2 expression. (a) (i) Flow cytometric analysis showing lack of expression of ACKR2 by CD45+ve cells in lung digests as assessed by comparing Alexa-CCL22 uptake (*X*-axis) in WT and ACKR2$^{-/-}$ (KO) lungs. The Y-axis shows side scatter (SSC) ($n = 3$ WT and 3 KO mice per experiment. The experiment was performed three times). (ii) Graph showing combined results of (i) for multiple analyses of Alexa-CCL22 binding by CD45^{+} cells from the lung. There are no significant differences in the binding profiles of WT and ACKR2$^{-/-}$ (KO) CD45^{+} cells. Error bars represent mean± SD. (b) Analysis of transcriptomic data generated from lung stromal populations showing low level ACKR2 expression in fibroblasts but high-level expression in blood endothelial cells (analyzed using a bespoke bioinformatics pipeline available through Glasgow Polyomics:www.polyomics.gla.ac.uk). These data were generated from resting lung stromal populations as well as from the same populations retrieved from lungs at the indicated times (10 and 40 days) postinfluenza virus infection. (Data were generated and combined using RNA from four separate lung cell harvests and the transctiptomic analyses performed once on these samples. Error bars represent mean ± SD. (c) qPCR analysis of pulmonary ACKR2 expression from embryonic day E13.5 to adult 9-week-old mice. Data were normalized to expression of the housekeeping gene Tata-binding protein. Statistical significance was tested using a one-way ANOVA test and $^{***}p < 0.001$. (Each time point represents PCR data combined from four separate lung preps. PCR was performed on one occasion once all samples were obtained.) Error bars represent mean ± SD. (d) Flow cytometric analysis of CD45-ve Alexa-CCL22 internalizing cells from WT and ACKR2$^{-/-}$ lungs. The *X*-axis shows the Alexa-CXCL22 binding, while the Y-axis shows staining for the epithelial marker EpCAM. ($n = 3$ WT and 3 KO mice per experiment. The experiment was performed three times.) (e) Quantification of the percentage of ACKR2+ve stromal cells detected using this Alexa-CCL22 in vitro labeling approach. Data are combined from three experiments with $n = 3$ mice/group. Statistical significance was tested using Student's *T* test and $^{*}p < 0.05$. Error bars represent mean ± SD.

in the digested lung. However, and as shown in Fig. 1d, this technology, which works well with leukocytes [35, 39, 40] and mammary gland fibroblasts [30], revealed only a minor difference in the numbers of Alexa-CCL22 internalizing cells in WT or ACKR2$^{-/-}$ lungs. These data are summarized numerically in Fig. 1e.

Overall, therefore, these data indicate that ACKR2 is predominantly expressed on stromal cells within the lung but that flow cytometry utilizing fluorescent chemokine uptake with digested lung tissue has limited sensitivity to detect the key stromal expressing cell types. Importantly, the Alexa-CCL22 was added to the lung cells after digestion was completed and the cells washed. There is therefore unlikely to be any contribution of proteolytic degradation of the ligand to the weak binding results obtained in these experiments.

Intratracheal fluorescent chemokine administration detects key ACKR2-expressing stromal components

We reasoned that the function of stromal ACKR2 expression may be dependent on interactions with other stromal components and that the inability to detect it using flow cytometry reflects the inability to take up Alexa-CCL22 due to absence of these interactions. We therefore harvested intact lungs and inflated them with Alexa-CCL22 (in RPMI) intratracheally followed by incubation at

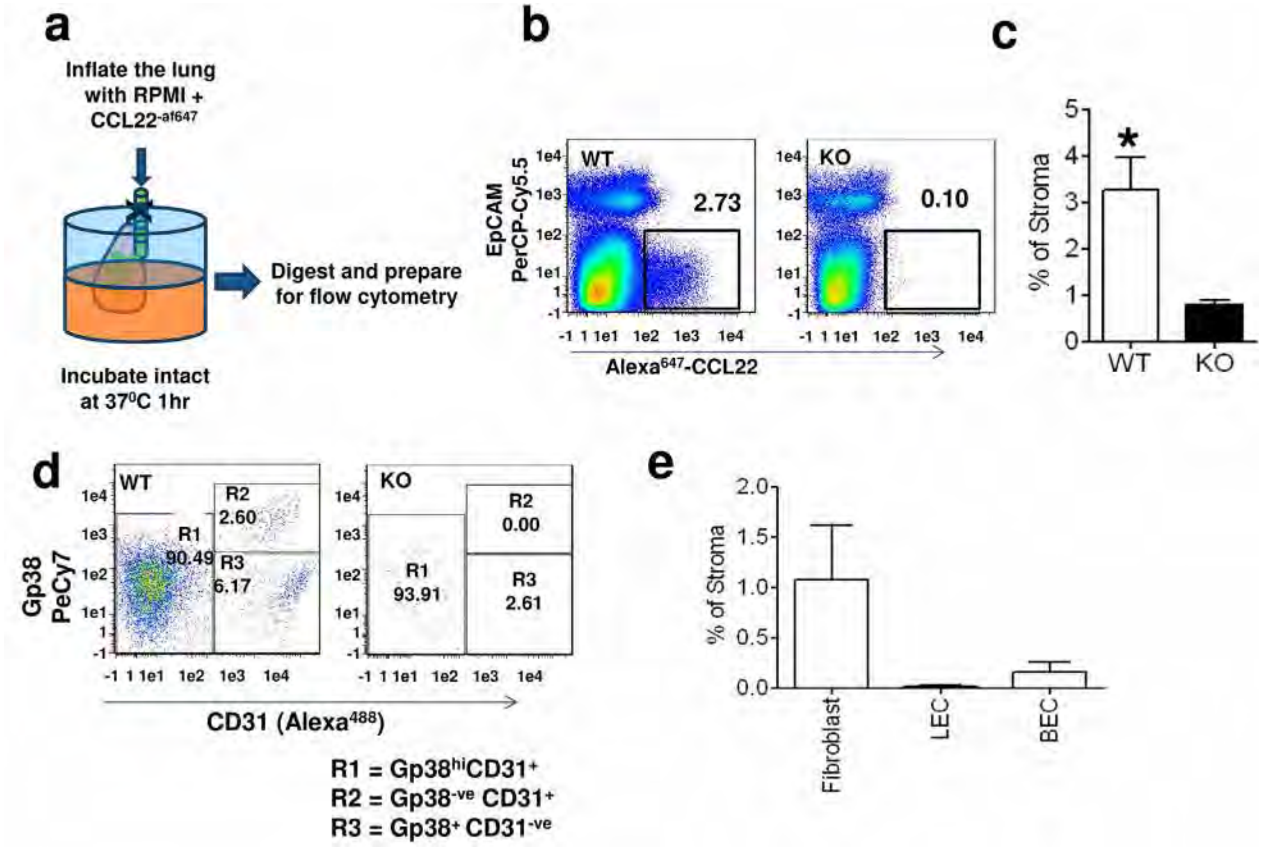

Figure 2. Detection of stromal ACKR2 expression by intratracheal administration of Alexa-CCL22. (a) Diagram indicating the basic methodology that involves removing intact lungs and inflating them through the trachea using an RPMI/Alexa-CCL22 mix. The lung is then incubated at 37°C for 1 h, then digested and prepared for flow cytometry. (b) Flow cytometric analysis showing the presence of a significant Alexa-CCL22 internalizing stromal component in the lung. The X-axis shows the Alexa-CXCL22 binding/internalization, while the Y-axis shows staining for the epithelial marker EpCAM. ($n = 3$ WT and 3 KO mice per experiment. The experiment was performed three times.) (c) Quantification of the levels of stromal ACKR2 detected in WT and ACKR2$^{-/-}$ (KO) lungs following intratracheal Alexa-CCL22 administration. Data are combined from three experiments with $n = 3$ mice/group. Statistical significance was tested using Student's T test and $^{*}p < 0.05$. Error bars represent mean + SD. (d) Flow cytometric analysis of the CD45-ve EpCAM-ve nonepithelial stromal component expressing ACKR2 on the basis of CD31 and Gp38 expression. Data shown are from Alexa-CCL22 binding lung stromal cells from WT (left plot) and ACKR2$^{-/-}$ (KO; right plot) mice. ($n = 3$ WT and 3 KO mice per experiment. The experiment was performed three times.) (e) Summary analysis of the percentage of CD45-ve stroma associated with each of the indicated cell types following intratracheal administration of Alexa-CCL22. Data are combined from three experiments with $n = 3$ mice/group. Error bars represent mean ± SD.

37°C for 1 h (Fig. 2a). Following this, flow cytometric analysis of digested lungs focusing on CD45-ve cellular populations now revealed a sizeable population of Alexa-CCL22 internalizing cells in WT lungs, which are absent from ACKR2$^{-/-}$ lungs (Fig. 2b). These cells are nonepithelial as they are negative for EpCAM staining and these data are summarized numerically in Fig. 2c. Further flow cytometric analysis indicated that these cells fall into three basic categories as defined by CD31 and Gp38 expression (Fig. 2d). These represent fibroblasts (R1; CD31−Gp38−), lymphatic endothelial cells (R2; CD31+Gp38+), and blood endothelial cells (R3; CD31+Gp38−), which are enumerated as shown in Fig. 2e.

Overall, these data demonstrate that it is possible to detect stromal cell populations that bind and internalize Alexa-CCL22 via ACKR2 by introducing the chemokine intratracheally into the intact lung. They also demonstrate novel stromal expression patterns for ACKR2 within the lung.

A subpopulation of fibroblasts in the lung expresses ACKR2

Cells identified in the R1 gate in Fig. 2d, which were negative for markers of lymphatic and vascular endothelial cells, were further phenotyped. Initially, these cells were isolated by cell sorting and then grown in tissue culture. As shown in Fig. 3a, the cells display a morphology suggestive of a fibroblastic phenotype. Flow cytometric analysis revealed that these cells are negative for markers of epithelial (CD166) and endothelial (CD49f) cells but positive for the fibroblastic marker CD140a (Fig. 3b). The CD140a+ve cells can be subdivided into three populations based on Sca-1 staining and SSC. Further Alexa-CCL22 binding assays revealed that the dominant ACKR2-expressing population was Sca-1 high and SSC lo/mid in phenotype (Fig. 3c). Figure 3d further shows that sorted ACKR2+ fibroblastic cells were capable of binding Alexa-CCL22 as indicated by the extensive fluorescence (arrows),

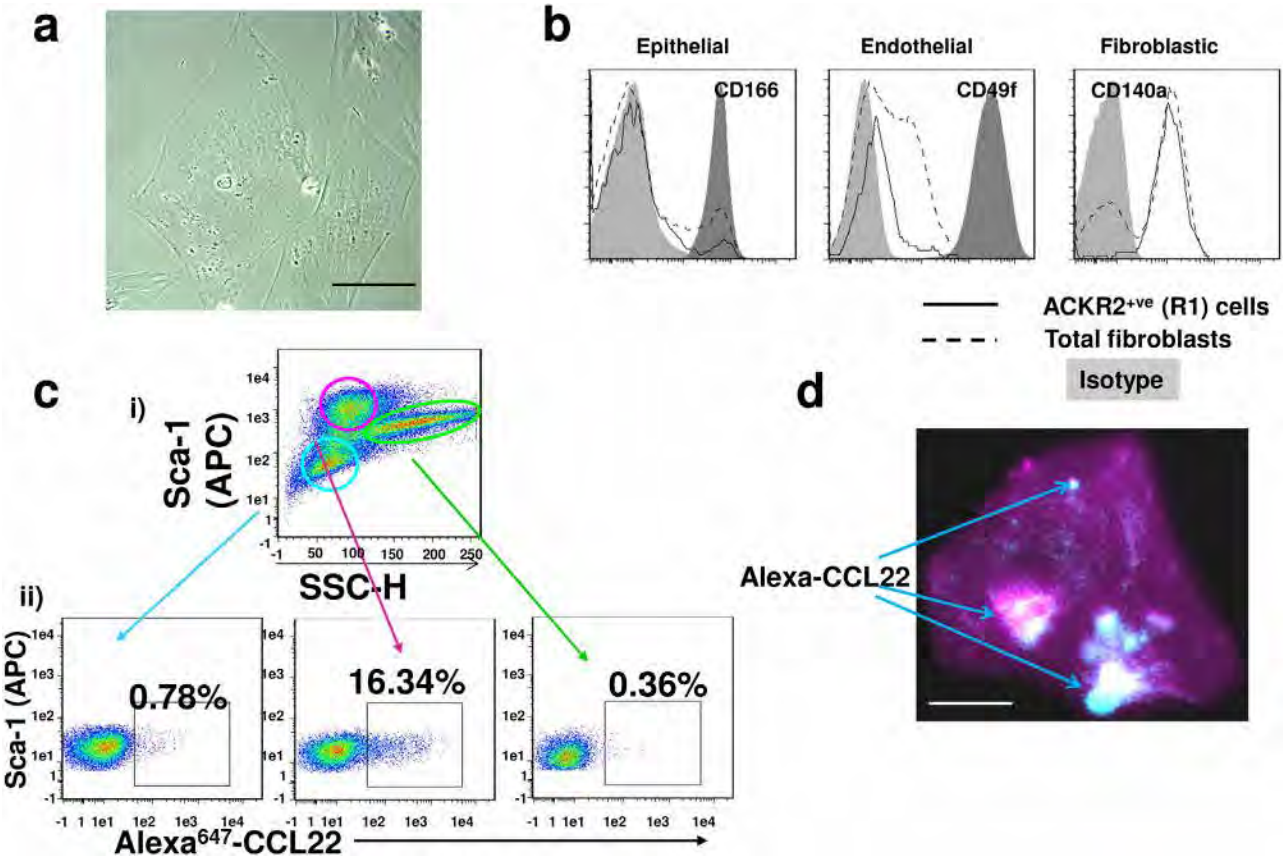

Figure 3. Identification of a fibroblastic population as a component of the ACKR2-expressing stromal population. (a) Brightfield image of cells sorted for internalization of fluorescently labeled Alexa-CCL22. These cells are negative for Gp38, CD45, and CD31 expression ($n = 3$). (Representative image from three separate in vitro cultures.) Image captured at 63× magnification. Scale bar: 10 μm. (b) Flow cytometric analysis of the fibroblastic population showing absence of expression of epithelial (CD166) and endothelial (CD49f) markers but positive expression of fibroblastic markers (CD140a). ($n = 3$ mice per experiment. The experiment was performed three times.) (c) (i) Flow cytometry profile showing Sca-1 staining and SSC for the CD140a$^+$ fibroblast population. (ii) Flow cytometric analysis of Alexa-CCL22 binding by each of the 3 Sca-1+ve populations. ($n = 3$ WT and 3 KO mice per experiment. The experiment was performed three times.) (d) Fluorescent confocal image of ACKR2+ve fibroblastic cells binding and internalizing Alexa-CCL22 (arrowed). (Representative image from three separate in vitro cultures). Image captured at 63× magnification. Scale bar: 10 μm.

confirming expression of functional ACKR2 (Fig. 3b). Given the punctate nature of much of this staining, we propose that it is largely intracellular in nature. Overall these data indicate that one of the ACKR2-expressing stromal components in the lung detected by intratracheal Alexa-CCL22 administration is a fibroblastic subpopulation characterized by CD140a and Sca-1 expression.

Intravenous fluorescent chemokine administration detects further ACKR2-expressing stromal components

We have previously reported expression of ACKR2 in lymphatic endothelial cells [31], however expression in blood endothelial cells as shown in Fig. 2d and e has not been reported. In fact, and as shown in Supporting Information Fig. 3, comparison of transcriptomic data from a broad range of microvascular endothelial types indicates that expression in blood endothelial cells is peculiar to the lung. Given that we have reported polarization of expression of ACKR2 in trophoblasts and lymphatic endothelial cells [31, 34, 41], we wondered whether it may also be polarized in blood endothelial cells. If this is the case, then it is possible that the vascular facing aspect of endothelial cells may be more able to internalize Alexa-CCL22 and thus the blood endothelial cell component might be underestimated by the intratracheal administration of the chemokine. We therefore next injected Alexa-CCL22 intravenously (Fig. 4a) and then harvested the lung for flow cytometric analysis of Alexa-CCL22 cellular interactions. Again, this analysis revealed that Alexa-CCL22 was not bound by lung-resident CD45$^+$ cells (data not shown) but uptake was seen in three populations of nonepithelial stromal cells in WT but not ACKR2$^{-/-}$ lungs. These populations comprised fibroblasts, blood endothelial cells, and lymphatic endothelial cells (Fig. 4b). However, and in contrast to intratracheal administration, intravenous administration detected blood endothelial cells as being by far the dominant ACKR2-expressing stromal population. Figure 4c shows that intravenous administration highlights blood endothelial cells as being the predominant stromal cell component in the lung and comparing intratracheal administration with intravenous

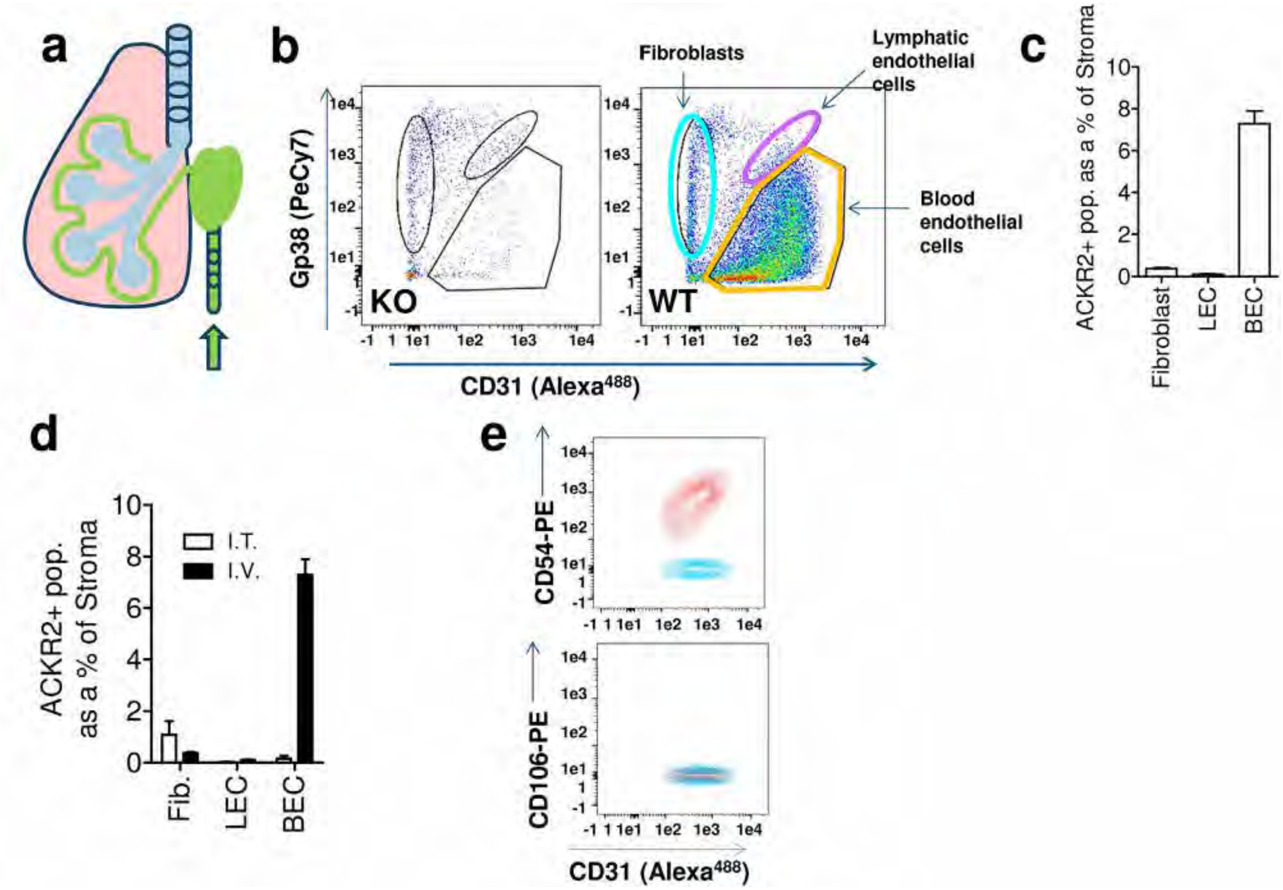

Figure 4. Intravenous administration of Alexa-CCL22 reveals strong expression of ACKR2 on the luminal face of pulmonary vascular endothelial cells. (a) Diagram indicating intravenous injection of Alexa-CCL22 into live mice. (b) Flow cytometric analysis of CD31 (*X*-axis) and Gp38 (*Y*-axis) expression by CD45-ve EpCAM-ve stromal cells that internalize Alexa-CCL22 in ACKR2$^{-/-}$ (KO) and WT lungs. The identified populations are indicated. ($n = 3$ WT and 3 KO mice per experiment. The experiment was performed three times.) (c) Quantification of the % of CD45-ve stromal cellular populations internalizing Alexa-CCL22 following intravenous administration of Alexa-CCL22. Data are combined from three experiments with $n = 3$ mice/group. Error bars represent mean ± SD. (d) Comparison of intratracheal and intravenous administration and the impact on the relative size of the ACKR2+ stromal cell populations detected by flow cytometry. Fib., fibroblasts; LEC, lymphatic endothelial cells; BEC, blood endothelial cells. Data are combined from three experiments with $n = 5$ mice/group. Error bars represent mean ± SD. (e) Flow cytometric analysis of the CD31+ve, Alexa-CCL22 internalizing blood endothelial cells indicate that they are positive for expression of CD54 and negative for CD106 and thus are alveolar, rather than peribronchial, endothelial cells. Red: the gated CD31$^+$ cells that have been antibody stained; blue, fluorescence minus one (FMO) control. ($n = 5$ mice per experiment. The experiment was performed twice.)

administration (Fig. 4d) reveals the differences in cellular detection using these two approaches. As we have previously shown expression of ACKR2 by lymphatic endothelial cells [31, 32], it remained possible that what we have characterized as lung blood endothelial cells are in fact lung lymphatic endothelial cells displaying an altered CD31/Gp38 phenotype compared to other lymphatic endothelial cell populations. To formally test this, we examined lung lymphatic endothelial cell expression of CD31 and Gp38 using Prox-1 reporter mice. Prox-1 is a definitive marker and an essential master regulator of lymphatic endothelial cells [42]. As shown in Supporting Information Fig. 4, Prox-1+ve cells from reporter mouse lungs were exclusively co-positive for CD31 and Gp38, confirming the faithfulness of the lymphatic phenotype in the lung. These data further confirm the blood endothelial nature of the ACKR2+ve stromal cells.

In the lung, there are two major blood vascular beds: one associated with bronchial tissues and one with alveolar tissues. These can be discriminated on the basis of CD54 and CD31 expression [43]. As shown in Fig. 4e, the Alexa-CCL22 internalizing blood endothelial cell population is strongly co-positive for CD31 and CD54, demonstrating that this population is associated with alveolar blood vessels and not peribronchial blood vessels.

In situ hybridization and antibody expression confirm blood endothelial cell expression of ACKR2

To further validate ACKR2 expression by murine pulmonary vascular endothelial cells, we carried out in situ hybridization. As shown in Fig. 5a, clear in situ hybridization signals were seen associated

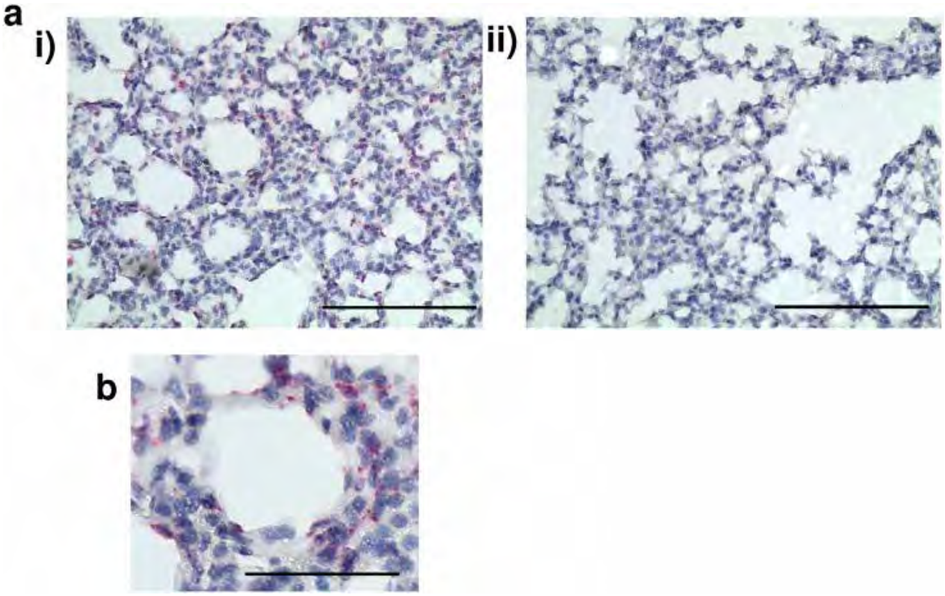

Figure 5. In situ and antibody detection of ACKR2 on pulmonary alveolar blood endothelial cells in mouse and human lung. (a) Representative in situ hybridization showing positivity for ACKR2 expression in alveolar endothelial cells in murine lungs (arrow). (i) WT lungs and (ii) ACKR2$^{-/-}$ lungs. Note the absence of signal in alveolar macrophages. Image captured at 10× magnification. Scale bars: 200 μm. (*n* = 3 mice per experiment. The experiment was performed twice). (b) High power image cropped from (i) showing the peri-alveolar localization of the vascular staining. This image has been amplified 2× and the scale bar = 100 μm.

with alveolar endothelial cells in blood vessels surrounding the alveolar air space in WT, but not ACKR2$^{-/-}$, adult murine lungs. A higher magnification image of a portion of Fig. 5a(i) is shown in Fig. 5b, further highlighting the peri-alveolar localization of the vascular staining. Therefore, in situ hybridization confirms blood endothelial cell expression of ACKR2 in the murine lung.

Discussion

ACKRs are predominantly expressed on stromal cell types and serve key functions in localizing and fine-tuning chemokine activities [15]. While a number of antibodies and reporter mouse-based approaches are available for analysis of ACKR expression patterns, in many cases these are limited and applicable only to mouse and humans. Given that many of the ACKRs display strong evolutionary conservation, other more versatile approaches would therefore represent a significant improvement in the methodological repertoire for ACKR expression analysis. Here, we demonstrate, using the lung, that fluorescently labeled chemokines can be used, with intact tissues, to precisely isolate and phenotypically define stromal cell types expressing individual ACKRs. This is particularly important when, as in the current analyses, removal of the cells from their stromal environment impairs ACKR2 function and thus frustrates this detection methodology. The ability to chemically synthesize chemokines with relative ease and to introduce discrete fluorescent markers at the carboxy terminus [40] means that this approach has full versatility and is appropriate for all members of the chemokine receptor family and all species expressing either typical or ACKRs. Importantly, while we demonstrate the utility of this approach using WT and KO mice, the use of appropriate unlabeled competing chemokines specific for the receptor being studied will allow this technology to be used under circumstances, or in species, where KO models do not exist.

Here, we show that intratracheal, and intravenous, administration of fluorescently labeled CCL22 is capable of identifying stromal cell populations expressing ACKR2. Importantly, in the context of vascular endothelial cell expression, intravenous administration has the advantage of detecting chemokine receptor expression with a polarity favoring expression on the luminal side of the endothelium. Together these approaches allowed us to define fibroblasts, lymphatic endothelial cells, and surprisingly alveolar blood endothelial cells as key sites of stromal ACKR2 expression in the lung. Notably, and in contrast to previous reports, we did not detect ACKR2 activity on alveolar macrophages [44, 45]. This may be due to species differences in expression or alternatively may be a consequence of nonspecific antibody internalization by the alveolar macrophages. Further analysis is required to address this discrepancy.

In summary, therefore we report a methodology appropriate for detecting ACKR expression in the lung, which we believe to be sufficiently versatile to be useful to detect other atypical and typical chemokine receptors in numerous tissues in vivo in divergent species. The data indicate for the first time the stromal expression patterns of ACKR2 in the lung with notably high expression levels on alveolar endothelial cells. These data will help interpret the outcome of analysis of ACKR2 function in the lung, which remains poorly defined.

Materials and Methods

Mice

Animal experiments were performed using cohoused mice in ventilated cages in a barrier facility that conformed to the animal care and welfare protocols approved by the University of Glasgow under the revised Animal (Scientific Procedures) Act 1986 and the European Union Directive 2010/63/EU. Ackr2-deficient mice[21] were bred in-house (C57BL/6 background); wild-type (WT) C57BL6/J mice were from Charles River Research Models and Services. Prox-1 reporter mice were obtained from Jackson laboratories. All experimental mice were sex and age matched.

qPCR

RNA was extracted using RNeasy columns with DNase treatment (Qiagen), and the amount of RNA was quantified on a Nanodrop 1000 Spectrophotometer (Thermo Fisher Scientific). cDNA was synthesized using High-capacity RNA-to-cDNA kit by Applied Biosystems (Thermofisher). For all qPCRs, a final concentration of 0.2 mM primers was used for each PCR set up using PerfeCTa SYBR Green FastMix and ROX qPCR Master Mix (Quanta BioSciences). qPCRs were performed on a Prism 7900HT Fast Real-Time PCR System (Applied Biosystems). The thermal cycles for qPCR of TBP and ACKR2 were 95˚C (3 min) for one cycle and 95˚C (3 s) and 60˚C (30 s) for 40 cycles. Relative expression was calculated using serial dilutions of cDNA standards. Primer sequences designed for qPCR and for producing cDNA standards were designed using Primer3 software (http://frodo.wi.mit.edu/cgi-bin/primer3/primer3_www.cgi). The following primers were used: mouse ACKR2, 5′-TTCTCCCACTGCTGCTTCAC-3′, 5′-TGCCATCTCAACATCACAGA-3′; mouse TBP primer: 5′- AAGGGAGAATCATGGACCAG-3′, 5′-CCGTAAGGCATCATTGGACT-3′.

In situ hybridization

Mice were culled using increasing concentration of CO_2. Lungs were placed in 10% neutral buffered formalin at room temperature for 24–36 h before they were processed by dehydration using rising concentrations of ethanol, xylene stabilization, and paraffin embedding (Shandon citadel 1000; Thermo Shandon). Tissue was then sectioned onto Superfrost plus slides (VWR) at 6 µm using a Microtome (Shandon Finesse 325 Microtome; Thermo). All slides for analysis were processed together. Slides were baked at 60°C for 1 h before pretreatment. Slides were deparaffinized with xylene (5 min × 2) and dehydrated with ethanol (1 min × 2). In situ hybridization was performed using the RNAscope® 2.5 HD Reagent Kit-RED from Advanced Cell Diagnostics (cat. no. 322350) and according to the manufacturer's instructions. Briefly, tissues were incubated with hydrogen peroxide for 10 min at RT. The slides were boiled in antigen retrieval buffer for 15 min. Slides were treated with "protease plus" for 30 min at 40°C. Slides were then hybridized using the RNAScope 2.5 Red Manual Assay (Advanced cell diagnostics) according to manufacturer's instructions using the Mm-ACKR2 probe (NM_021609.4). Slides were mounted in DPX (Sigma Aldrich) and imaged on an EVOS M7000 microscope (Thermofisher).

Intratracheal and intravenous chemokine administration

To administer fluorescent chemokine intratracheally, mice were euthanized using an appropriate schedule 1 method or CO_2 exposure. The mice were then carefully dissected to remove the ribcage and expose the intact lungs and trachea in situ. Using a pair of surgical scissors, a small incision was made at the top of the exposed trachea toward the base of the jaw. A 2 µg/mL solution of Alexa 647^{TM} labeled CCL22 (Almac; Alexa-CCL22) dissolved in RPMI/25mM HEPES was prepared in a polypropolene tube and preserved from light at room temperature until needed. Once the dissection was complete, a syringe with a 19G needle and loaded with 400 µL of the Alexa-CCL22 solution was then inserted into the exposed trachea via the incision. The needle should be tight within the trachea and care should be taken not to pierce the trachea further down. The lungs were then inflated with the chemokine solution and the trachea carefully tied off with surgical thread to prevent the leakage of chemokine solution as the syringe is removed. The intact inflated lungs were then removed and placed into a falcon tube containing enough RPMI to cover the intact inflated lungs. The lungs were then incubated in a water bath for 1 h at 37°C. Following this time, the lungs were removed from the water bath and the surgical thread cut to allow draining of the remaining chemokine solution. The lungs were then digested for a single cell suspension as per the protocol.

Flow cytometry

All flow cytometry analyses adhered to published guidelines for use of flow cytometry and cell sorting in immunological studies [46]. Lungs were removed and finely chopped with scissors, then incubated in digestion mix (1.6 mg/mL Dispase [Roche], 0.2 mg/mL Collagenase P [Roche], and 0.1 mg/mL DNase I [Invitrogen]) in HBSS on a gentle shake at 37°C for 40 min. Lungs were passed through a 40 µm mesh (Greiner Bio-One), RBCs were lysed in 1 mL RBC lysis buffer (eBioscience) for 1 min, and then in 10 mL FACs buffer (PBS, 1% FCS, 0.02% sodium azide, 5 mM EDTA) to quench the reaction. The resulting single cell suspension was preincubated with Fc block (BD Biosciences) in FACS buffer (PBS, 1% FCS, and 5 mM EDTA) and labeled with fluorescent anti-mouse Abs, including CD45 (30-F11), Gp38 (8.1.1), CD140a (APA5), EpCAM-1 (G8.8), CD31 (390), and CD49f (GoH3), each labeled with various fluorochromes (Biolegend) CD166 (eBioALC48) (Ebioscience). Dead cells were labeled using Fixable viability dye efluor 506 or efluor 780 (ebioscience). Cells were stained for 20 min on ice before washing with FACS buffer. Cells were either analyzed by flow cytometry immediately or fixed for 20 min with 2% methanol-free paraformaldehyde (Invitrogen) before washing and placing at 4°C in the dark until ready to be analyzed typically 12–24 h later. Cells were analyzed using LSR2 flow cytometers (Beckton Dickinson) or sorted on a FACSAria. Data were analyzed using FlowJo Version 9.2 software (TreeStar) with populations defined by size, viability, and "fluorescence minus one" isotype controls. Gating strategies are shown in Supporting Information Fig. 5.

Immunofluorescence

Alexa-CCL22 labeled ACKR2+ fibroblasts were flow-sorted from a single cell suspension using the ARIAII (Beckman and Dickinson) as per the flow protocol. ACKR2$^+$ fibroblasts were resuspended in PBS at a density of 2000 cells/mL. Note that 100 μL of this cell suspension was loaded into a cytospin 3 machine (Thermo-Shandon) and the cells were spun for 5 min at 200 rpm onto Superfrost^{TM} plus slides. The cells were air dried in the dark and mounted in Vectashield Hard set mounting medium (Vector Laboratories). The cells were visualized using a Zeiss Spinning Disc confocal microscope.

Fibroblast culture and analyses

Primary ACKR2 positive fibroblasts were flow-sorted from a single cell suspension using the ARIAII (Beckman and Dickinson) as per the flow protocol. Retrieved cells were spun down at 400g for 5 min and washed three times into EMEM with 15% FBS, $1\times$ penicillin/streptomycin, nonessential amino acids, and sodium pyruvate. The cells were plated at a density of approximately 5×10^3 cells per well of a 24-well plate (Gibco). Fibroblasts were cultured as standard in an incubator at 37°C, 5% CO_2.

Statistics

Statistical tests were carried out using Graph Pad Prism software and the individual tests used are indicated in the relevant figure legends. $P = 0.05$ was taken as a cut-off for statistical significance.

Acknowledgements: This study was funded by a Programme Grant from the Medical Research Council. Work in G.J.G.'s lab is also supported by a Wellcome Investigator Award. G.J.G. is a recipient of a Wolfson Royal Society Research Merit Award.

Conflict of interest: The authors declare no financial or commercial conflict of interest.

References

1 **Rot, A. and von Andrian, U. H.**, Chemokines in innate and adaptive host defense: basic chemokinese grammar for immune cells. *Annu. Rev. Immunol.* 2004. **22**: 891–928.

2 **Griffith, J. W., Sokol, C. L. and Luster, A. D.**, Chemokines and chemokine receptors: positioning cells for host defense and immunity. *Annu. Rev. Immunol.* 2014. **32**: 659–702.

3 **Nomiyama, H., Osada, N. and Yoshie, O.**, A family tree of vertebrate chemokine receptors for a unified nomenclature. *Dev. Comp. Immunol.* 2011. **35**: 705–715.

4 **Ara, T., Nakamura, Y., Egawa, T., Sugiyama, T., Abe, K., Kishimoto, T., Matsui, Y. and Nagasawa, T.**, Impaired colonization of the gonads by primordial germ cells in mice lacking a chemokine, stromal cell-derived factor-1 (SDF-1). *Proc. Natl. Acad. Sci. USA* 2003. **100**: 5319–5323.

5 **Valentin, G., Haas, P. and Gilmour, D.**, The chemokine SDF1a coordinates tissue migration through the spatially restricted activation of Cxcr7 and Cxcr4b. *Curr. Biol.* 2007. **17**: 1026–1031.

6 **Boidajipour, B., Mahabaleshwar, H., Kardash, E., Reichman-Fried, M., Blaser, H., Minina, S., Wilson, D. et al.**, Control of chemokine-guided cell migration by ligand sequestration. *Cell* 2008. **132**: 463–473.

7 **Doitsidou, M., Reichman-Fried, M., Stebler, J., Koprunner, M., Dorries, J., Meyer, D., Esguerra, C. V. et al.**, Guidance of primordial germ cell migration by the chemokine SDF-1. *Cell* 2002. **111**: 647–659.

8 **Lapidot, T., Dar, A. and Kollet, O.**, How do stem cells find their way home? *Blood* 2005. **106**: 1901–1910.

9 **Zou, Y., Kottmann, A., Kuroda, M., Taniuchi, I. and Littman, D.**, Function of the chemokine receptor CXCR4 in haematopoiesis and in cerebellar development. *Nature* 1998. **393**: 595-599.

10 **Dyer, D. P., Medina-Ruiz, L., Bartolini, R., Schuette, F., Hughes, C. E., Pallas, K., Vidler, F. et al.**, Chemokine receptor redundancy and specificity are context dependent. *Immunity* 2019. **50**: 378–389.e375.

11 **Schall, T. J. and Proudfoot, A. E. I.**, Overcoming hurdles in developing successful drugs targeting chemokine receptors. *Nat. Rev. Immunol.* 2011. **11**: 355–363.

12 **Bachelerie, F., Ben-Baruch, A., Burkhardt, A. M., Combadiere, C., Farber, J. M., Graham, G. J., Horuk, R. et al.**, International Union of Pharmacology. LXXXIX. Update on the extended family of chemokine receptors and introducing a new nomenclature for atypical chemokine receptors. *Pharmacol. Rev.* 2014. **66**: 1–79.

13 **Bachelerie, F., Graham, G. J., Locati, M., Mantovani, A., Murphy, P. M., Nibbs, R., Rot, A. et al.**, New nomenclature for atypical chemokine receptors. *Nat. Immunol.* 2014. **15**: 207–208.

14 **Bachelerie, F., Graham, G. J., Locati, M., Mantovani, A., Murphy, P. M., Nibbs, R., Rot, A. et al.**, An atypical addition to the chemokine receptor nomenclature: IUPHAR Review 15. *Br. J. Pharmacol.* 2015. **172**: 3945–3949.

15 **Nibbs, R. J. B. and Graham, G. J.**, Immune regulation by atypical chemokine receptors. *Nat. Rev. Immunol.* 2013. **13**: 815–829.

16 **Antonio Sanchez-Alcaniz, J., Haege, S., Mueller, W., Pla, R., Mackay, F., Schulz, S., Lopez-Bendito, G. et al.**, Cxcr7 controls neuronal migration by regulating chemokine responsiveness. *Neuron* 2011. **69**: 77–90.

17 **Sierro, F., Biben, C., Martinez-Munoz, L., Mellado, M., Ransohoff, R. M., Li, M., Woehl, B. et al.**, Disrupted cardiac development but normal hematopoiesis in mice deficient in the second CXCL12/SDF-1 receptor, CXCR7. *Proc. Natl. Acad. Sci. USA* 2007. **104**: 14759–14764.

18 **Ulvmar, M. H., Werth, K., Braun, A., Kelay, P., Hub, E., Eller, K., Chan, L. et al.**, The atypical chemokine receptor CCRL1 shapes functional CCL21 gradients in lymph nodes. *Nat. Immunol.* 2014. **15**: 623–630.

19 **Graham, G. J.**, D6/ACKR2. *Front. Immunol.* 2015. **6**: 280.

20 **Di Liberto, D., Locati, M., Caccamo, N., Vecchi, A., Meraviglia, S., Salerno, A., Sireci, G. et al.**, Role of the chemokine decoy receptor D6 in balancing inflammation, immune activation, and antimicrobial resistance in Mycobacterium tuberculosis infection. *J. Exp. Med.* 2008. **205**: 2075–2084.

21 **Jamieson, T., Cook, D. N., Nibbs, R. J., Rot, A., Nixon, C., McLean, P., Alcami, A. et al.**, The chemokine receptor D6 limits the inflammatory response in vivo. *Nat. Immunol*. 2005. **6**: 403–411.

22 **Lee, K. M., McKimmie, C. S., Gilchrist, D. S., Pallas, K. J., Nibbs, R. J., Garside, P., McDonald, V. et al.**, D6 facilitates cellular migration and fluid flow to lymph nodes by suppressing lymphatic congestion. *Blood* 2011. **118**: 6220–6229.

23 **Martinez de la Torre, Y., Locati, M., Buracchi, C., Dupor, J., Cook, D. N., Bonecchi, R., Nebuloni, M. et al.**, Increased inflammation in mice deficient for the chemokine decoy receptor D6. *Eur. J. Immunol*. 2005. **35**: 1342–1346.

24 **Whitehead, G. S., Wang, T., DeGraff, L. M., Card, J. W., Lira, S. A., Graham, G. J. and Cook, D. N.**, The chemokine receptor D6 has opposing effects on allergic inflammation and airway reactivity. *Am. J. Respir. Crit. Care Med*. 2007. **175**: 243–249.

25 **Hansell, C. A. H., Fraser, A. R., Hayes, A. J., Pingen, M., Burt, C. L., Lee, K. M., Medina-Ruiz, L. et al.**, The atypical chemokine receptor Ackr2 constrains NK cell migratory activity and promotes metastasis. *J. Immunol*. 2018. **201**:2510–2519.

26 **Nibbs, R. J., Gilchrist, D. S., King, V., Ferra, A., Forrow, S., Hunter, K. D. and Graham, G. J.**, The atypical chemokine receptor D6 suppresses the development of chemically induced skin tumors. *J. Clin. Invest*. 2007. **117**: 1884–1892.

27 **Vetrano, S., Borroni, E. M., Sarukhan, A., Savino, B., Bonecchi, R., Correale, C., Arena, V. et al.**, The lymphatic system controls intestinal inflammation and inflammation-associated colon cancer through the chemokine decoy receptor D6. *Gut* 2010. **59**: 197–206.

28 **Massara, M., Bonavita, O., Savino, B., Caronni, N., Mollica Poeta, V., Sironi, M., Setten, E. et al.**, ACKR2 in hematopoietic precursors as a checkpoint of neutrophil release and anti-metastatic activity. *Nat. Commun*. 2018. **9**: 676.

29 **Lee, K. M., Danuser, R., Stein, J. V., Graham, D., Nibbs, R. J. and Graham, G. J.**, The chemokine receptors ACKR2 and CCR2 reciprocally regulate lymphatic vessel density. *EMBO J* 2014. **33**: 2564–2580.

30 **Wilson, G. J., Hewit, K. D., Pallas, K. J., Cairney, C. J., Lee, K. M., Hansell, C. A., Stein, T. and Graham, G. J.**, Atypical chemokine receptor ACKR2 controls branching morphogenesis in the developing mammary gland. *Development* 2017. **144**: 74–82.

31 **McKimmie, C. S., Singh, M. D., Hewit, K., Lopez-Franco, O., Le Brocq, M., Rose-John, S., Lee, K. M. et al.**, G. J., An analysis of the function and expression of D6 on lymphatic endothelial cells. *Blood* 2013. **121**: 3768–3777.

32 **Nibbs, R. J., Kriehuber, E., Ponath, P. D., Parent, D., Qin, S., Campbell, J. D., Henderson, A. et al.**, The beta-chemokine receptor D6 is expressed by lymphatic endothelium and a subset of vascular tumors. *Am. J. Pathol*. 2001. **158**: 867–877.

33 **Lee, K. M., Wilson, G. J., Pingen, M., Fukuoka, A., Hansell, C. A. H., Bartolini, R., Medina-Ruiz, L. and Graham, G. J.**, Placental chemokine compartmentalisation: a novel mammalian molecular control mechanism. *PLoS Biol*. 2019. **17**: e3000287.

34 **Madigan, J., Freeman, D. J., Menzies, F., Forrow, S., Nelson, S. M., Young, A., Sharkey, A. et al.**, Chemokine scavenger D6 is expressed by trophoblasts and aids the survival of mouse embryos transferred into allogeneic recipients. *J. Immunol*. 2010. **184**: 3202–3212.

35 **Hansell, C. A. H., Schiering, C., Kinstrie, R., Ford, L., Bordon, Y., McInnes, I. B., Goodyear, C. S. and Nibbs, R. J. B.**, Universal expression and dual function of the atypical chemokine receptor D6 on innate-like B cells in mice. *Blood* 2011. **117**: 5413–5424.

36 **Ameti, R., Melgrati, S., Radice, E., Cameroni, E., Hub, E., Thelen, S., Rot, A. and Thelen, M.**, Characterization of a chimeric chemokine as a specific ligand for ACKR3. *J. Leukoc. Biol*. 2018. **104**: 391–400.

37 **Ford, L., Hansell, C. H. and Nibbs, R. B.**, Using Fluorescent Chemokine Uptake to Detect Chemokine Receptors by Fluorescent Activated Cell Sorting. In Cardona, A. E. and Ubogu, E. E. (Eds.), *Chemokines*, Humana Press, Totowa, New Jersey 2013, 203–214.

38 **Anselmo, A., Mazzon, C., Borroni, E. M., Bonecchi, R., Graham, G. J. and Locati, M.**, Flow cytometry applications for the analysis of chemokine receptor expression and function. *Cytometry A* 2014. **85**: 292–301.

39 **Ford, L. B., Cerovic, V., Milling, S. W., Graham, G. J., Hansell, C. A. and Nibbs, R. J.**, Characterization of conventional and atypical receptors for the chemokine CCL2 on mouse leukocytes. *J. Immunol*. 2014. **193**: 400–411.

40 **Le Brocq, M. L., Fraser, A. R., Cotton, G., Woznica, K., McCulloch, C. V., Hewit, K. D., McKimmie, C. S. et al.**, Chemokines as novel and versatile reagents for flow cytometry and cell sorting. *J. Immunol*. 2014. **192**: 6120–6130.

41 **Singh, M. D., King, V., Baldwin, H., Burden, D., Thorrat, A., Holmes, S., McInnes, I. B. et al.**, Elevated expression of the chemokine-scavenging receptor D6 is associated with impaired lesion development in psoriasis. *Am. J. Pathol*. 2012. **181**: 1158–1164.

42 **Wigle, J. T. and Oliver, G.**, Prox1 function is required for the development of the murine lymphatic system. *Cell* 1999. **98**: 769–778.

43 **Paine, R., 3rd, Christensen, P., Toews, G. B. and Simon, R. H.**, Regulation of alveolar epithelial cell ICAM-1 expression by cell shape and cell-cell interactions. *Am. J. Physiol*. 1994. **266**: L476–L484.

44 **Castanheira, F., Borges, V., Sonego, F., Kanashiro, A., Donate, P. B., Melo, P. H., Pallas, K. et al.**, The atypical chemokine receptor ACKR2 is protective against sepsis. *Shock* 2018. **49**: 682–689.

45 **Bazzan, E., Saetta, M., Turato, G., Borroni, E. M., Cancellieri, C., Baraldo, S., Savino, B. et al.**, Expression of the atypical chemokine receptor D6 in human alveolar macrophages in COPD. *Chest* 2013. **143**: 98–106.

46 **Cossarizza, A., Chang, H. D., Radbruch, A., Acs, A., Adam, A., Adam-Klages, S., Agace, W. et al.**, Guidelines for the use of flow cytometry and cell sorting in immunological studies. *Eur. J. Immunol*. 2019.**49**: 1457–1973.

Abbreviation: **ACKR**: atypical chemokine receptor

Full correspondence: Dr. Gerard J. Graham, Chemokine Research Group, Institute of Infection, Immunity and Inflammation, University of Glasgow, 120 University Place, Glasgow G12 8TA, UK
e-mail: gerard.graham@glasgow.ac.uk

The peer review history for this article is available at https://publons.com/publon/10.1002/eji.201948374

Received: 2/9/2019
Revised: 13/12/2019
Accepted: 28/2/2020
Accepted article online: 29/2/2020

Received: 4 December 2019 | Revised: 3 June 2020 | Accepted: 15 June 2020

DOI: 10.1002/term.3082

RESEARCH ARTICLE

The effects of cross-linking a collagen-elastin dermal template on scaffold bio-stability and degradation

Joanneke Maitz[1] | Yiwei Wang[1,6] | Ali Fathi[2] | Francia Ximena Escobar[1] | Roxanne Parungao[1] | Paul van Zuijlen[3,4] | Peter Maitz[1,5,6] | Zhe Li[1,5,6]

[1]Burn Injury and Reconstructive Surgery Research Group, ANZAC Research Institute, Concord, New South Wales, Australia

[2]Faculty of Engineering and Information Technologies, University of Sydney, Camperdown, New South Wales, Australia

[3]Burn Centre and Dept. of Plastic and Reconstructive Surgery, Red Cross Hospital, Beverwijk, the Netherlands

[4]Amsterdam Movement Sciences, Amsterdam UMC, Amsterdam, NH, the Netherlands

[5]Burns Unit, Concord Hospital, Concord, New South Wales, Australia

[6]Disciplines of Surgery, University of Sydney Concord Clinical School, Concord, New South Wales, Australia

Correspondence

Zhe Li, Burns Unit, Concord Hospital, Hospital Road, Concord, NSW 2139, Australia.
Email: zhe.li@health.nsw.gov.au

Abstract

MatriDerm is a collagen-elastin dermal template that promotes regeneration in full-thickness wound repair. Due to its noncross-linked status, MatriDerm biodegrades quickly in a wound. Facilitating vascularization and dermal repair, it is desirable for MatriDerm to remain present until the wound healing process is complete, optimizing tissue regeneration and reducing wound contraction. The aim of this study was to investigate the effect of cross-linking MatriDerm on its mechanical and biological properties and to enhance its regenerative functionality. MatriDerm was chemically cross-linked and characterized in comparison with noncross-linked MatriDerm. Scaffold properties including surface morphology, protein release and mechanical strength were assessed. Cell-scaffold interaction, cell proliferation and migration were examined using human dermal fibroblasts. Scaffold biodegradation and its impact on wound healing and contraction were studied in a mouse model. Results showed that cross-linked MatriDerm displayed a small reduction in pore size, significantly less protein loss and a threefold increase in tensile strength. A significant increase in fibroblast proliferation and migration was observed in cross-linked MatriDerm with reduced scaffold contraction in vitro. In the mouse model, noncross-linked MatriDerm was almost completely biodegraded after 14 days whereas cross-linked MatriDerm remained intact. No significant difference in wound contraction was found between scaffolds. In conclusion, cross-linked MatriDerm showed a significant increase in stability and strength, enhancing its durability and cell-scaffold interaction. in vivo analysis showed cross-linked MatriDerm had a reduced biodegradation rate with a similar host response. The extended structural integrity of cross-linked MatriDerm could potentially facilitate improved skin tissue regeneration, promoting the formation of a more pliable scar.

KEYWORDS

collagen-elastin scaffold, cross-linking, degradation, human dermal fibroblasts, mouse model, skin regeneration

1 | INTRODUCTION

Full-thickness skin defects from burns or trauma are traditionally treated by skin grafting, in the majority of cases with an autologous split thickness skin graft. These autologous split thickness skin grafts are harvested from the patient at the junction of the papillary dermis and thereby only include a small amount of dermal elements. The majority of the dermal elements remains in the donor site and ensures wound closure of the donor site similar to the healing of a graze wound. The dermal elements within the split thickness skin graft ensure integration of the graft into a well vascularized wound bed, closing the full-thickness defect. However, due to the lack of a fully intact dermis providing mechanical support for skin regeneration within the slip thickness skin graft, significant scarring is a common outcome (Varkey, Ding, & Tredget, 2015), Scarring is not only associated with aesthetic issues, in specific anatomical areas, particularly over joint flexor surfaces, significant scarring can cause contractures (Harrison & MacNeil, 2008) and severe functional disabilities (Schneider, Holavanahalli, Helm, Goldstein, & Kowalske, 2006; van Baar et al., 2006). In many burn victims, scarring becomes an enduring life-long debilitating consequence of their injuries (Holavanahalli, Helm, & Kowalske, 2010).

In 1980, Integra, the first artificial collagen dermal template chemically cross-linked with glutaraldehyde was introduced to address dermal replacement and subsequently scarring (Burke, Yannas, Quinby, Bondoc, & Jung, 1981; Dagalakis, Flink, Stasikelis, Burke, & Yannas, 1980; Yannas and Burke, 1980; Yannas, Burke, Gordon, Huang, & Rubenstein, 1980). The introduction of dermal regeneration by bioengineered soft tissue reconstruction changed the field of reconstructive surgery. Throughout the following decades, dermal substitutes have been developed to replace the damaged dermis and to provide scaffolding structures for cell attachment, ingrowth, and angiogenesis to generate a neodermis. Dermal substitutes are now available as a variety of porous structures with components including biological proteins and synthetic polymers (Chua et al., 2016; Nyame, Chiang, Leavitt, Ozambela, & Orgill, 2015; Shevchenko et al., 2010; Wang et al. 2018.). With a variety of production techniques available, cross-linking treatment of protein-based dermal scaffolds is one of many procedures to stabilize the proteins, increasing its durability in vivo and time to allow for cell infiltration and tissue regeneration (Reddy, Reddy, & Jiang, 2015).

MatriDerm, a bovine collagen-elastin matrix, is a commercially available dermal substitute for dermal regeneration. MatriDerm is a noncross-linked porous scaffold that has proven to be an effective dermal substitute (Bloemen, van Leeuwen, van Vucht, van Zuijlen, & Middelkoop, 2010; Hur, Seo, & Lee, 2014; Lamme et al., 1996). It is the only available dermal template that has elastin incorporated into the scaffold. As the human native dermal extracellular matrix is composed of 2–4% elastin (dry weight), providing an essential structural and mechanical role (Jelena Rnjak-Kovacina, 2013), the addition of elastin in similar proportions in a dermal regenerative template allows the template to resemble the natural extracellular matrix more closely. However, due to the noncross-linked status of MatriDerm, the scaffold has been demonstrated to biodegrade relatively quickly in vivo. In a study comparing five commercially available dermal substitutes in a porcine model, MatriDerm was noted to biodegrade faster compared with Integra, having fragmented and lost its structure on Day 21 whereas Integra was still fully intact (Philandrianos et al., 2012). In the design of a dermal template, stability and biodegradation are essential properties to fulfil the function as temporary replacements of the extracellular matrix. Ideally, a dermal template contains its three-dimensional, intact structure until the proliferative phase of the wound healing process is complete (van der Veen, van der Wal, van Leeuwen, Ulrich, & Middelkoop, 2010). In humans, the proliferative phase to rebuild the extracellular matrix usually lasts 3 weeks. If the scaffold structures are of poor mechanical strength, it will biodegrade quicker, depriving the wound healing process of the necessary structural support too early and potentially affecting tissue regeneration (Druecke et al., 2004). By increasing mechanical strength and thereby decreasing the rate of biodegradation over time, the extended presence of a more natural supporting scaffold could enhance dermal regeneration and subsequently improve wound healing, wound contraction, and scarring. Further research is required to optimize the structure of dermal substitutes to improve their efficacy in both scar tissue formation and its application in skin tissue engineering. This study is designed to investigate if the in vitro and in vivo performance of MatriDerm as a bioscaffold could be further improved by cross-linking to enhance its bio-stability and extend cell-scaffold interaction for neodermal development.

2 | MATERIALS AND METHOD

2.1 | MatriDerm

MatriDerm (MedSkin Solutions Dr. Suwelack AG, Germany) is a porous dermal regenerative template made of native bovine collagen Types I, III, and V and 3% alpha-elastin hydrolysate from bovine nuchal ligament. It is sterilized through gamma-radiation and stored at room temperature. It is available in various sizes with a thickness of either 1 or 2 mm. For all in vitro and in vivo analysis in this study, 1-mm thick MatriDerm samples with a surface area of either 1 or 0.5 cm^2 were prepared using a scalpel blade (No. 22, Swann-Morton, England) or an 8-mm biopsy punch (Kai Medical, Japan), respectively.

2.2 | Cross-linking MatriDerm

Chemical cross-linking with glutaraldehyde (Sigma Aldrich, United States) is a well-developed technique to increase protein stability and has been reported safe to use in low concentrations (<8%; Reddy et al., 2015). It has been used to cross-link Integra since 1980s, which is still widely used in clinical practice. MatriDerm samples were cross-linked by glutaraldehyde 2.5% (v/v) vapour treatment in a glass desiccator over a period of 24 h at room temperature (humidity of <60%). The cross-linking process was ceased by treating the samples with 0.2 M glycine (Ajax Finechem, ThermoFisher Scientific, United States) in reverse osmosis water. The samples were then sterilized using 80% ethanol (v/v; Sigma Aldrich, United States) for 3 h and washed six times in sterile phosphate-buffered saline (PBS; ThermoFisher Scientific, United States) to remove residual glutaraldehyde. In order to dry the scaffolds, samples were removed from the PBS wash and placed on filter paper to soak up any residual PBS. All cross-linked and noncross-linked samples were stored dry and sterile at 4°C prior to further assessments.

2.3 | Characterization of cross-linked and noncross-linked MatriDerm

2.3.1 | Uniaxial tensile tests

Uniaxial elongation tensile tests were performed in an unconfined state using an Instron (Model 5543, United States) with a 10-N biological load cell, according to previously described testing procedures (Annabi et al. 2011; Fathi et al., 2013; Wang et al., 2015). Samples were soaked in PBS for 2 h at 37°C prior to mechanical testing (*n* = 3 per group). For both cross-linked and noncross-linked samples, the height, thickness, and width was recorded at 26.87 ± 3.55, 0.99 ± 0.10, and 9.84 ± 0.67 mm, respectively. For the uniaxial tensile tests, the samples were subjected to a loading and unloading cycle at 37°C; the load (N) was applied at a cross speed of 0.05 mm/min. The Young's modulus was obtained from the slope of the stress–strain curve generated over the linear portion of the strain range after the initial toe region. A determination of the ultimate tensile strength was not practical due to the inherent friability of the constructs, which included failure at the grips.

2.3.2 | Stability

Samples (0.5 cm^2) of cross-linked or non-cross-linked MatriDerm were placed in 500 μl of PBS and placed on a shaker for gentle circulation (60 rpm) of PBS around the samples in a consistent environment of 37°C over 35 days (*n* = 3 per group). PBS was collected every 2 days and replaced with fresh PBS. The protein concentration in PBS was determined by bicinchoninic acid assay (Pierce BCA assay, ThermoFisher Scientific, United States) and compared with a calibration curve established using a series dilution of bovine serum albumin (ThermoFisher Scientific, United States) in PBS. The protein released was subsequently calculated as % w/w and used to assess the influence of cross-linking on protein biodegradation.

2.3.3 | Surface morphology

Surface morphology of noncross-linked or cross-linked MatriDerm was examined using a scanning electron microscope (SEM; JEOL JSM-6380, JEOL Ltd., Tokyo, Japan; *n* = 2 per group). Dry, sterile specimens were mounted on aluminum sample stubs and sputter coated with platinum using an auto coater (JFC-1600 Auto Fine Coater, JEOL Ltd., Tokyo, Japan) prior to examination in the SEM at a voltage of 15 kV.

2.3.4 | Quantification of pore size and porosity

Average pore size was determined by measuring 30 randomized pores on SEM images of cross-linked and noncross-linked MatriDerm using a Java-based image processing program (ImageJ, Laboratory for Optical and Computational Instrumentation, United States; *n* = 3 per group). Pore size was measured by two independent observers. To determine porosity, samples of cross-linked and noncross-linked were fixed in 10% formalin (Sigma Aldrich, United States) for 24 h prior to tissue processing and embedded in paraffin blocks (*n* = 3 per group). Sections of 5 μm were stained using haemotoxylin and eosin (H&E; Biostain, Australia and VWR, Australia). Stained sections of noncross-linked and cross-linked MatriDerm were imaged using a microscope cell imaging system (EVOS M7000 Cell Imaging System, ThemoFisher Scientific, United States) at a magnification of ×20, and black and white binary conversion was generated using ImageJ. The porosity was calculated using ImageJ and defined as percentage of interfibre space relative to the total scaffold area measured.

2.4 | In vitro analysis of human dermal fibroblast interaction with cross-linked and noncross-linked MatriDerm

2.4.1 | Cell proliferation and distribution

In vitro analysis was conducted with primary human dermal fibroblasts cultured in Dulbecco modified eagle medium (DMEM), supplemented with 10% (v/v) foetal bovine serum, 2-mM L-glutamine and 100 U penicillin-0.1 mg streptomycin-0.2 mg neomycin/mL at 37°C, and 5% CO_2 (Sigma Aldrich, United States). The fibroblasts (at Passage 4) were harvested and seeded onto either cross-linked and noncross-linked MatriDerm samples at a density of 100,000 cells/cm^2 (*n* = 3 per group, per time point). Cell-seeded scaffolds were incubated at 37°C and 5% CO_2 under steady-state conditions and were collected on Days 1 and 14 postseeding. All cell-seeded scaffolds were fixed in 10% (v/v) neutrally buffered formalin for 24 h and subsequently dehydrated through a series of ethanol and xylene (Point of Care Diagnostics, Australia) concentrations. The cell-seeded scaffolds were soaked in paraffin and then embedded in paraffin blocks for histology. Sections at a thickness of 5 μm were collected every 200 μm to quantify cell population throughout each cross-section and determine cell distribution evenly throughout the entire sample. Samples were stained with Masson's Trichrome (Acros Organics, ThermoFisher Scientific, United States) staining, and cell numbers in each collected section were counted manually using a light microscope by two independent researchers. Cell proliferation and cell distribution throughout the samples at Days 1 and 14 were compared between cross-linked and noncross-linked MatriDerm.

2.4.2 | SEM analysis of human dermal fibroblast-seeded scaffolds

Cell morphology of human dermal fibroblasts seeded on cross-linked and noncross-linked MatriDerm was examined using an SEM. Cell-seeded scaffolds were removed from the culture plates at Days 1 and 14 post cell seeding (*n* = 3 per group, per time point). After rinsing three times with PBS, cell-seeded templates were primarily fixed with 2.5% glutaraldehyde in 0.1 M sodium cacodylate buffer for 2 h. Samples were rinsed with cacodylate buffer before the secondary fixation with 2% osmium tetroxide for 2 h. The fixed cell-seeded scaffolds were washed with sodium cacodylate buffer (Sigma Aldirch, United States) and dehydrated in a series of ethanol dilutions from 50–95% (v/v) and completing the process with 100% molecular-sieved ethanol (Sigma Aldrich, United States). Samples were rinsed two to three times for 2 min in each solution. The specimens were air-dried, mounted on aluminum sample stubs, and sputter coated with platinum prior to examination in the SEM at a voltage of 15 kV.

2.4.3 | Contraction of human dermal fibroblast-seeded and nonseeded scaffolds

Prior to cell proliferation and morphological analysis, each cell-seeded scaffold was measured in their cell culture well to monitor cell-induced contraction at Dayw 1 and 14 postseeding (*n* = 4 per group, per time point). Images were taken of the scaffolds in their respective culture plates, and the diameter of each scaffold was measured using ImageJ in reference to the diameter of the culture well. Calculation was conducted based on the measurements collected by two independent researchers.

2.5 | In vivo analysis of cross-linked and noncross-linked MatriDerm in a murine model

2.5.1 | Murine model

Pathogen-free, male Balb/c mice, aged 12 weeks, and weighing an average of 23.5 ± 0.7 g were used for this study (*n* = 3 per group, per time point). All animals were housed in standard approved cages with free access to food and water, in the Molecular Physiology Unit of the ANZAC Research Institute. The environment was closely controlled at 24–26°C and 44–46% humidity under a 12:12 h light dark cycle with lights on at 6 am. All protocols for this study were approved by the Sydney Local Health District Welfare Committee (Protocol No. 2013/019) under the National Health and Medical Research Council guidelines for animal experimentation. A two-wound model was used for this study. Each mouse was anaesthetized individually via intraperitoneal injection of a mixture of ketamine (50 mg/ml) and xylazine (50 mg/ml; Troy Laboratories, Australia) at 0.01 ml/g of body weight. On each mouse, the dorsal area was shaved, and two adjacent but identical full-thickness skin excisions of 1 cm^2 were created surgically. The wounds were covered with either noncross-linked or cross-linked MatriDerm templates followed by full-thickness skin grafts from the opposite site superimposed onto the template, creating an autograft. Both grafts were sutured in place with 5-0 silk (Perma-Hand Silk, Ethicon, Johnson & Johnson, United States), dressed with Atrauman (Hartmann, Australia), IV 3000 (Smith & Nephew, United Kingdom), and an elasticated circular dressing to protect the dressing and skin graft. Carprofen (5 mg/kg; Rimadyl, Australia) was given at the time of anaesthesia and then on the following 2 days postoperatively for analgaesia. After surgery, each mouse was caged individually for the first 3 days and then two mice per cage thereafter with free access to water and food. Skin graft take was macroscopically observed and contraction was quantified by measuring wound size with VISITRAK™ Digital Portable Device (Smith & Nephew, United Kingdom) on Days 0, 3, 5, 7, 10, 14, 21, and 28 using a wound grid. Wound size was then measured using VISITRAK digital system by two independent researchers.

2.5.2 | Histology

Skin biopsies were collected on Day 7, 14, and 28 post procedure. Biopsies were fixed in 10% (v/v) formalin, embedded in paraffin and sectioned at 5-μm thickness. Cross-sections were deparaffinized in xylene, dehydrated in a series of ethanol, and stained with H&E. Samples were examined under a bright-field light microscope (Olympus BX60, Olympus, PA, United States). Microscopic skin graft take (acceptance of graft to the wound bed and subsequently viability of the graft), scaffold degradation, cell infiltration, and blood vessel formation were assessed by two independent researchers. Images of the samples were taken using a microscope cell imaging system.

2.6 | Statistics

Data are expressed as mean ± standard deviation. Using IBM SPSS software (IBM, United States), the statistical significance was evaluated with either *t* test for two groups or analysis of variance (ANOVA) for groups greater than two, with *p* value of <.05 being defined as statistically significant.

3 | RESULTS

3.1 | Characterization of cross-linked and noncross-linked MatriDerm

3.1.1 | Uniaxial tensile test results

Cross-linked MatriDerm was noted to be a macroscopically firmer, spongy scaffold when moistened compared with its more fragile noncross-linked counterpart. The tensile modulus of the noncross-linked and cross-linked constructs was obtained from the slope of the stress–strain curve generated over the linear portion of the strain range after the initial toe region. The findings from the mechanical analysis of the scaffolds showed that the cross-linking of the constructs resulted in a significant threefold increase in tensile modulus. A minor effect on energy loss was noted in cross-linked MatriDerm, when the strain level reached above 15%; however, no cracks or torsions were observed in the samples. Tensile modulus was measured at an average of 268.8 ± 27.9 kPa for cross-linked MatriDerm compared with 98.1 ± 12.6 kPa for noncross-linked MatriDerm (Figure 1a).

3.1.2 | Scaffold stability results

Scaffold stability testing was assessed based on protein release from the scaffolds into PBS at 37°C. A significantly higher release rate of protein from noncross-linked MatriDerm was found compared with cross-linked MatriDerm over a period of 35 days (Figure 1b). Initially, a protein burst release was observed on Day 1 for both noncross-linked and cross-linked scaffolds. However, noncross-linked MatriDerm released approximately 165.1 ± 11.2 μg of protein on Day 1, which is significantly higher than the cross-linked MatriDerm that only released 33.8 ± 2.4 μg on the same day. Subsequently, both scaffolds developed a plateau cumulative release of protein. Noncross-linked MatriDerm reached a plateau on Day 11, earlier than cross-linked MatriDerm. On Day 17, both scaffolds had reached their plateau with noncross-linked MatriDerm releasing protein at a rate of 9–11 μg/day and cross-linked MatriDerm releasing protein at a rate of 2–3 μg/day. In total, the protein released from noncross-linked MatriDerm was measured up to 407.3 μg after 35 days but only 107.4 μg for cross-linked MatriDerm. This result confirmed that a cross-linked MatriDerm scaffold is more stable, with reduced protein release suggesting a potentially slower biodegradation rate.

3.1.3 | Pore size, porosity, and morphology results

Cross-linked MatriDerm displayed a small but significant decrease in pore size and porosity compared with non-cross-linked MatriDerm. Pore size was visibly reduced under electron microscopy, forming condense and compressed fibres with a thicker width compared with those of non-cross-linked MatriDerm (Figure 2a). Pore size was found to be reduced by approximately 1.5 μm in cross-linked MatriDerm compared with noncross-linked MatriDerm. Average pore size of noncross-linked MatriDerm was measured at 26.5 ± 4.0 μm and of cross-linked MatriDerm at 25.0 ± 4.8 μm (Figure 2b). Porosity was also found to be significantly decreased in cross-linked MatriDerm, resulting in a 13.94% reduction in the porosity of cross-linked compared with noncross-linked MatriDerm (Figure 2c). Less pores and visibly thicker structured fibres of collagen and elastin were noted in the cross-sections of cross-linked MatriDerm (Figure 2d).

3.2 | In vitro analysis of cell-scaffold interaction

3.2.1 | Scaffold contraction

During the initial stages of seeding cross-linked and noncross-linked MatriDerm with human dermal fibroblasts, macroscopic contraction of the scaffold was observed over 14 days (Figure 3a). Noncross-linked MatriDerm decreased by 2.12 ± 0.13 mm in diameter, and cross-linked MatriDerm displayed a milder contraction of 1.19 ± 0.30 mm on Day 1 (Figure 3b). Noncross-linked MatriDerm was reduced by another 0.93 mm by Day 14, reducing its size to 4.95 ± 0.15 mm in diameter: a total 38% contraction compared with its original size. In contrast, cross-linked MatriDerm displayed minimal contraction, only reducing by another 0.15 mm in 14 days, resulting in a diameter of 6.66 ± 0.38 mm, with a total 17% contraction compared with its original size. Cross-linked MatriDerm was measured significantly larger (1.71 mm more in diameter on Day 14) compared with noncross-linked MatriDerm. Scaffold diameter was also compared between noncross-linked MatriDerm samples with and without cell seeding and cross-linked MatriDerm samples with and without cell seeding to determine whether scaffold contraction could be attributed to the human fibroblasts causing the contraction or the scaffold itself. No significant difference was found in the size between cell-seeded and noncell-seeded scaffolds within each scaffold group. Noncross-linked MatriDerm showed diameters of 4.95 ± 0.15 mm with cells and 4.91 ± 0.30 mm without cells, whereas cross-linked MatriDerm showed diameters of 6.66 ± 0.38 mm with cells and 6.63 ± 0.21 mm without cells by Day 14 (Figure 3c,d).

3.2.2 | Cell proliferation

Dermal fibroblast interaction with cross-linked and noncross-linked MatriDerm was examined, showing no evidence of cytotoxic effects of glutaraldehyde cross-linked MatriDerm on cultured fibroblasts and displaying significant differences in cell proliferation. On Day 1, cell number was found similar between cross-linked (50,745.7 ± 5,383

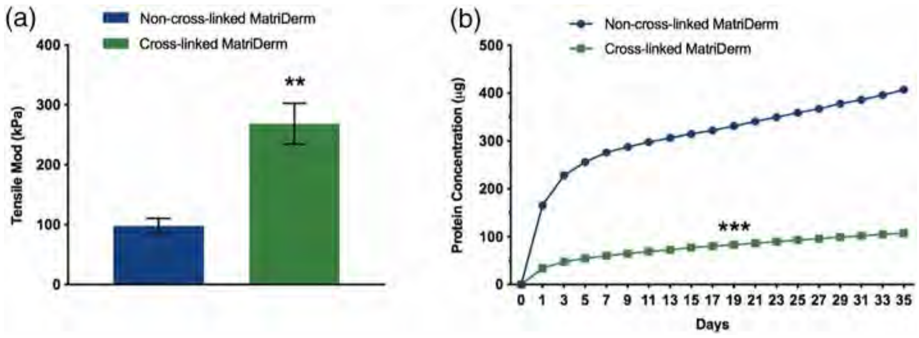

FIGURE 1 (a) Tensile modulus for noncross-linked and cross-linked MatriDerm, *p* value = .012E-1. (b) Accumulated protein release from cross-linked and noncross-linked MatriDerm over 35 days, *p* value = .031E-3. Error bars not visible due to small variation [Colour figure can be viewed at wileyonlinelibrary.com]

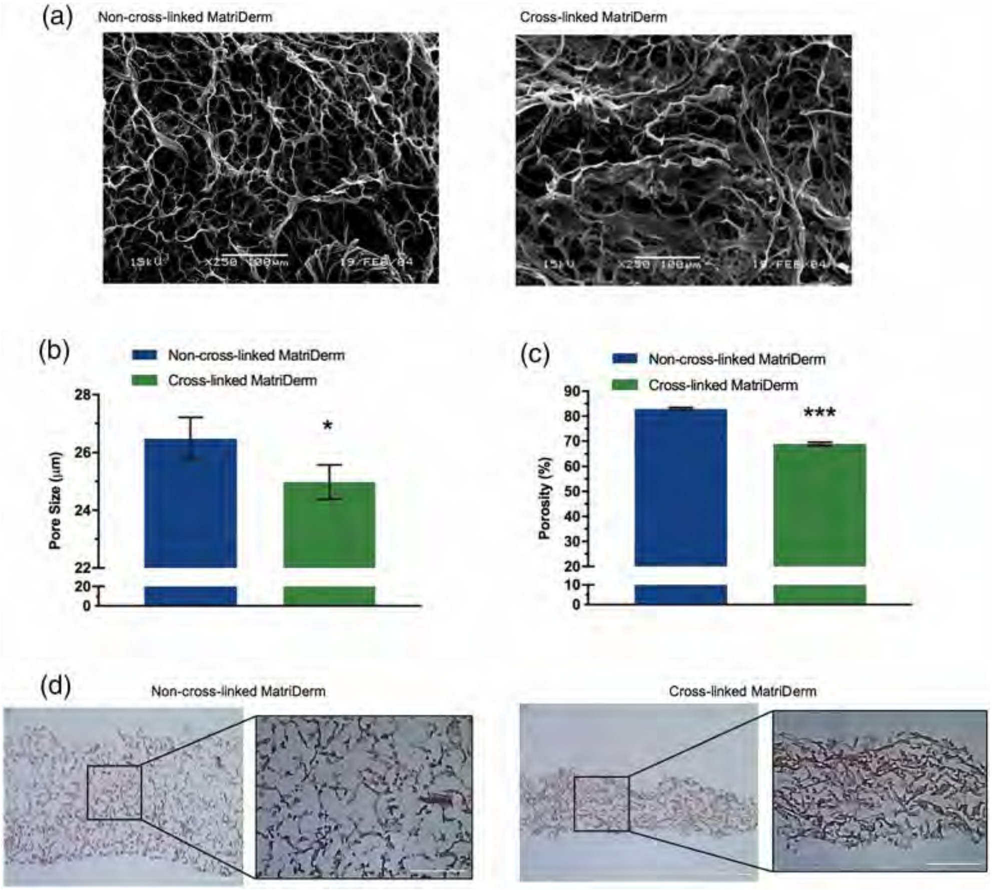

FIGURE 2 (a) Scanning electron microscopy images of noncross-linked and cross-linked MatriDerm, scale bar = 100 μm. (b) Average pore size of noncross-linked and cross-linked MatriDerm, *p* value = .024. (c) Porosity of noncross-linked MatriDerm compared with cross-linked MatriDerm, *p* value = .012E-13. D Transverse sections of H&E fixed noncross-linked and cross-linked MatriDerm prior to binary conversion, scale bar = 200 μm of and 100 μm in higher resolution [Colour figure can be viewed at wileyonlinelibrary.com]

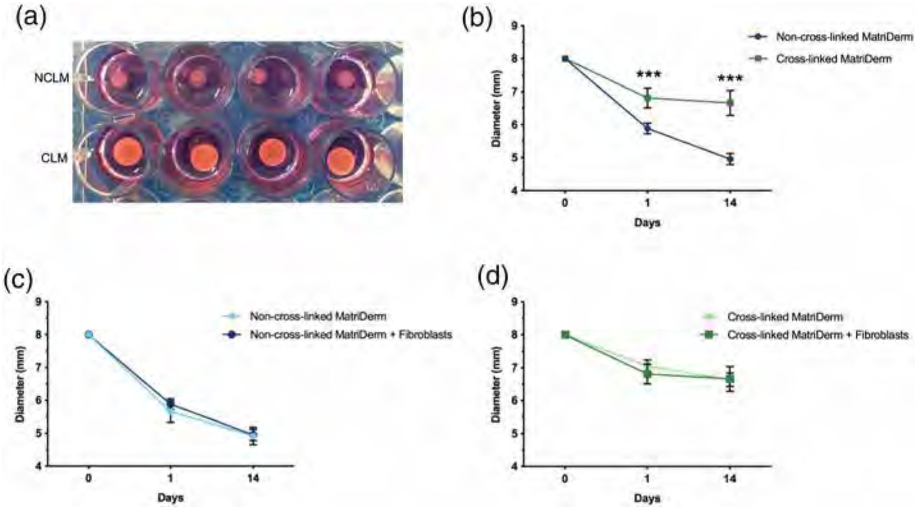

FIGURE 3 (a) Macroscopic image of non-cross-linked (NCLM) and cross-linked MatriDerm (CLM) seeded with human dermal fibroblasts in a cell cultured environment on Day 14. (b) Diameter (millimetre) of noncross-linked and cross-linked MatriDerm seeded with human dermal fibroblasts on Days 0, 1 (*p* value = .024E-2), and 14 (*p* value = .018E-3). (c) Diameter (millimetre) of noncross-linked MatriDerm without dermal fibroblasts and seeded with dermal fibroblasts on Days 0, 1, and 14. (d) Diameter (millimetre) of cross-linked MatriDerm without dermal fibroblasts and seeded with dermal fibroblasts on Days 0, 1, and 14. Note: *Y*-axis of images b, c, and d commence at 4 mm [Colour figure can be viewed at wileyonlinelibrary.com]

fibroblasts) and noncross-linked MatriDerm (52,179.3 ± 4,706 fibroblasts). After 14 days, dermal fibroblasts proliferating on cross-linked MatriDerm doubled in number (102,802.3 ± 15,797 fibroblasts), displaying a significant growth of 103% compared with Day 1. Dermal fibroblasts seeded onto noncross-linked MatriDerm only showed growth of 17% in 14 days (60,927.0 ± 4,005 fibroblasts). Significantly more cells were identified on cross-linked MatriDerm compared with noncross-linked MatriDerm (Figure 4a).

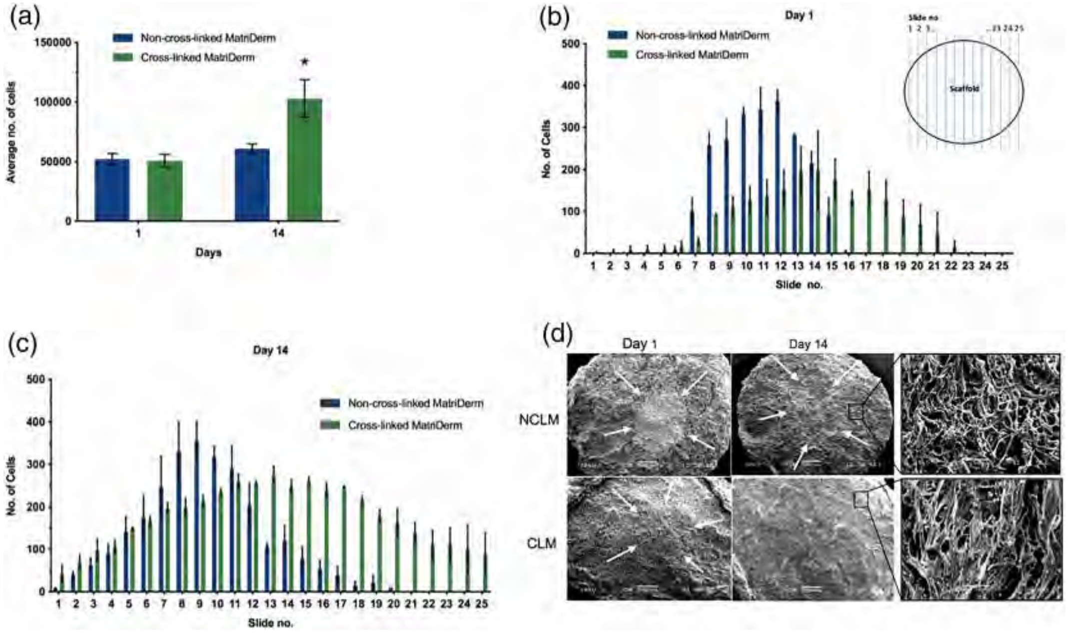

FIGURE 4 (a) Cell quantification of noncross-linked and cross-linked MatriDerm on Days 1 and day 14, *p* value = .047 for Day 14. (b) Pattern of distribution of dermal fibroblasts in noncross-linked and cross-linked MatriDerm on Day 1 including schematic drawing top left corner of scaffold cross-sections related to slide number. (c) Pattern of distribution of dermal fibroblasts in noncross-linked and cross-linked MatriDerm on Day 14. (d) Scanning electron microscopy of noncross-linked (NCLM) and cross-linked MatriDerm (CLM) seeded with human dermal fibroblasts on Days 1 and 14, scale bar = 500 μm, higher resolution of Day 14, scale bar = 50 μm. White arrows indicate the border of confluent cells [Colour figure can be viewed at wileyonlinelibrary.com]

3.2.3 | Cell migration and distribution

Dermal fibroblasts tended to migrate throughout cross-linked MatriDerm from Day 1, with cells more evenly distributed and cell growth extending towards the periphery, compared with noncross-linked MatriDerm. On Day 1, dermal fibroblasts seeded on cross-linked MatriDerm commenced cell migration immediately from the centrum dispersing throughout the scaffold, whereas dermal fibroblasts seeded onto noncross-linked MatriDerm were mainly concentrated in the centre (Figure 4b). On Day 14, a majority of the dermal fibroblasts seeded on non-cross-linked MatriDerm were still localized in the central area of the scaffold, whereas cross-linked MatriDerm demonstrated more cell migration and proliferation to the outermost edges of the scaffold (Figure 4c). Dermal fibroblast migration and distribution were also confirmed under SEM, showing centrally confluent cells in both noncross-linked and cross-linked MatriDerm on Day 1 (Figure 4d). On Day 14, cross-linked MatriDerm subsequently showed a thick layer of confluent dermal fibroblasts on cross-linked MatriDerm, covering the entire template. Noncross-linked MatriDerm only displayed a centrally confluent layer at Day 14 (Figure 4d, white arrows). Morphology of the dermal fibroblasts was not affected in cross-linked MatriDerm as the cells displayed similar healthy characteristics to the cells seeded onto noncross-linked MatriDerm. The results from the scanning electron microscopy images were consistent with cell quantification, distribution, and migration measurements.

3.3 | In vivo analysis in murine model

3.3.1 | Graft take and wound contraction

Similar graft take rate was measured in both cross-linked and noncross-linked MatriDerm, with 78% and 86% graft take, respectively. No significant difference in graft take was detected, demonstrating that glutaraldehyde cross-linked MatriDerm did not negatively affect wound healing (Figure 5a). Similar wound contraction was displayed in both cross-linked and noncross-linked MatriDerm wounds over 28 days (Figure 5b). Wound contraction rates increased at Day 7 for both cross-linked and noncross-linked MatriDerm, stabilizing on Day 21. At Day 28, wounds with cross-linked and noncross-linked MatriDerm contracted in total by 50.7% and 49.4%, respectively.

3.3.2 | In vivo host response and scaffold degradation

The in vivo scaffold study between cross-linked and noncross-linked displayed similar host responses. Both scaffolds were well tolerated by animals with minimal cell infiltration and local inflammation noted with histological analysis. However, cross-linked MatriDerm demonstrated a slower biodegradation in vivo. At Day 7, both scaffolds displayed an intact and sturdy structure under a taken graft (Figure 5c),

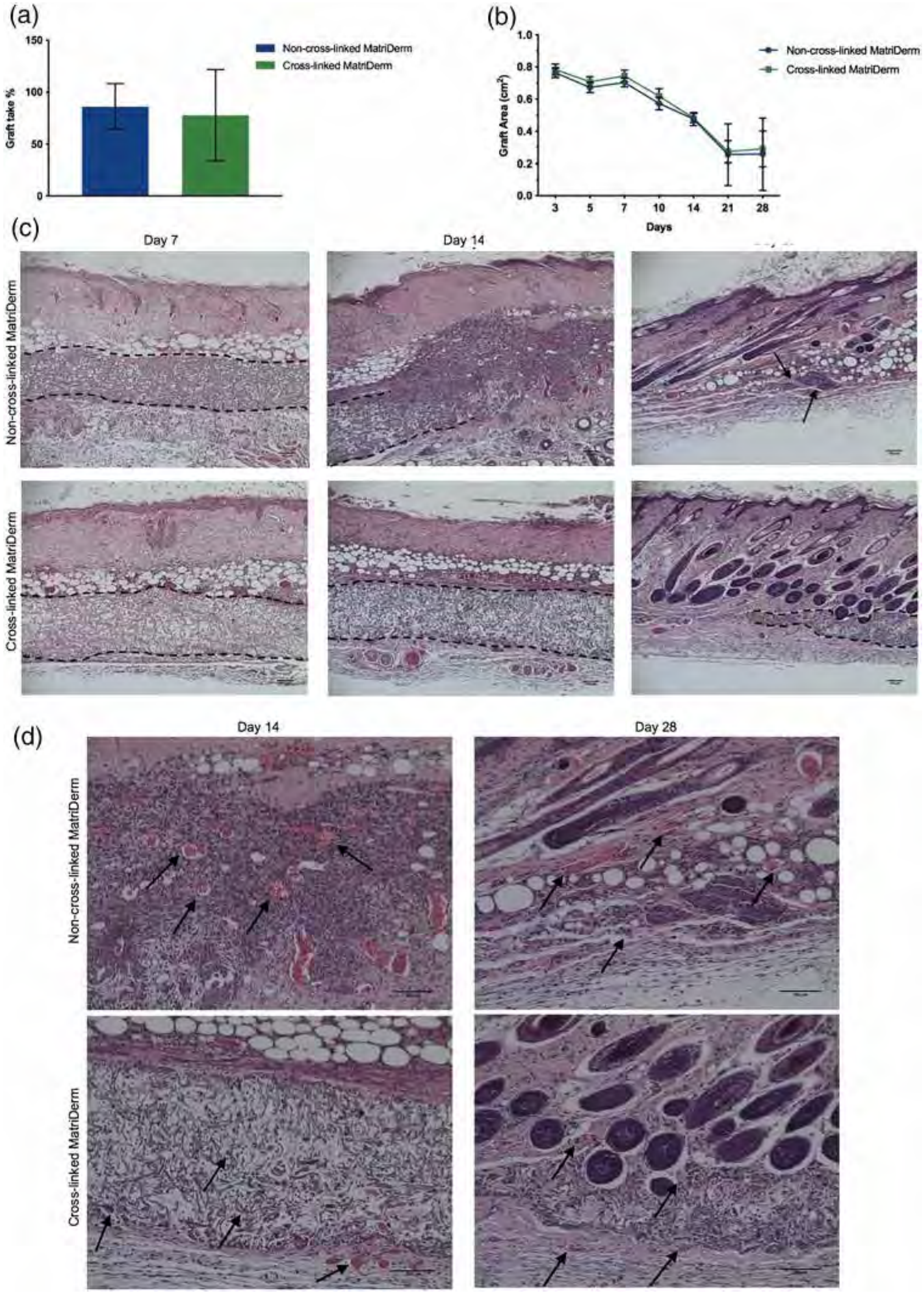

FIGURE 5 (a) Graft take (%) of noncross-linked and cross-linked MatriDerm in in vivo analysis. (b) Wound contraction of noncross-linked and cross-linked MatriDerm on Days 3, 5, 7, 10, 14, 21, and 28. (c) H&E-stained cross-linked and noncross-linked MatriDerm on Days 7, 14, and, 28. Scaffolds indicated by dotted line and arrows, scale bar = 100 μm. (d) Angiogenesis demonstrated by arrows in H&E-stained cross-linked and noncross-linked MatriDerm on Days 14 and 28, scale bar = 100 μm [Colour figure can be viewed at wileyonlinelibrary.com]

with cell infiltration observed between 20% and 40% for both scaffolds. At Day 14, noncross-linked MatriDerm breakdown was evident, fragmenting mainly centrally, with a considerable inflammatory response, whereas cross-linked MatriDerm was grossly intact. In comparison, 100% of the cross-linked MatriDerm scaffold remained compared with 61% of the noncross-linked MatriDerm scaffold. Host cell infiltration was observed to be higher centrally in noncross-linked MatriDerm, ranging from 90% to 100% centrally to 50–60% peripherally. Cross-linked MatriDerm displayed a more evenly dispersed host cell infiltration between 40% and 60%. At Day 28, cross-linked MatriDerm also showed signs of biodegradation, decreasing in size, whereas only remnants of noncross-linked MatriDerm were found. Approximately 60% of cross-linked MatriDerm were noted remaining under the skin grafts, whereas approximately 8% of non-cross-linked was found on Day 28. Noncross-linked host cell infiltration was observed at 95–100% as the scaffold was fully absorbed, and cross-linked MatriDerm at 95–100% centrally where absorbed, but 60–70% peripherally where fragments of the scaffold were still visible.

3.3.3 | Angiogenesis

Angiogenesis was observed in noncross-linked MatriDerm earlier than in cross-linked MatriDerm. Vessel formation was primarily observed in areas where the scaffold had been biodegraded with only fragmental remnants. At Day 14, noncross-linked MatriDerm was primarily degraded in the centre of the scaffold, displaying more neovascularization in noncross-linked MatriDerm compared with cross-linked MatriDerm. Cross-linked MatriDerm also displayed angiogenesis at Day 14 within the intact scaffold and by Day 28, vessel formation increasingly developed, displaying vessel formation similar to noncross-linked MatriDerm at Day 14.

4 | DISCUSSION

The existing and extensive research into the ideal dermal template for skin tissue engineering is becoming increasingly complex. Many commercial dermal substitutes are available today with different components, biological and mechanical properties, and cross-linking methods, attempting to achieve an optimal composition. Ideally, dermal templates should biodegrade gradually while promoting tissue regeneration at a matching speed, assisting the restoration of skin structures and functions. Optimization of scaffold properties including bio-stability and mechanical strength is therefore important in the quest to develop an ideal dermal template for the reconstruction of skin with minimal wound contraction and scarring. This study was designed to prolong the in vivo half-life of a commercially available dermal template that degrades relatively quickly. By chemically cross-linking MatriDerm, the scaffold's strength and stability were enhanced, prolonging its durability in both in vitro and in vivo studies. Increasing the mechanical strength resulted in a reduced biodegradation rate, allowing for a more ideal prolonged presence of the collagen-elastin matrix in the healing wound and potentially enhancing its regenerative properties.

In the quest to develop an ideal dermal template, investigation into the ideal pore size has been complicated by the growing possibilities of biomaterials and building techniques, each with its own effect on cell interaction (O'Brien et al., 2005; Wang et al., 2005). Furthermore, specific cells require different pore sizes for optimal cell attachment, growth, and motility (Salem et al., 2002). In poly(L-lactic acid) and poly(L-lactic-co-glycolic acid) scaffolds, pore sizes smaller than 160 μm have been reported to be optimal for the attachment of human skin fibroblasts (Yang et al., 2002). In a study with collagen-glycosaminoglycan scaffold cross-linked with glutaraldehyde and grafted in guinea pigs, the recommended optimal pore size was between 20 and 125 μm, however, requiring autologous cells seeding prior to implantation (Yannas et al., 1989). In fact, a recent study examining the effects of using an alternative chemical cross-linking method, 1-ethyl-3-(3-dimethylaminopropyl)carbodiimide hydrochloride cross-linking, on collagen scaffolds showed more favourable outcomes when pore size was not too enlarged, as a larger pore size promotes further myofibroblast differentiation and more foreign body giant cells (Boekema et al. 2014).

In this study, pore size and porosity were found to be affected by enhancing the physiochemical strength of MatriDerm through cross-linking with glutaraldehyde. The average pore size was measured to be approximately 26.5 μm for noncross-linked MatriDerm and 25 μm for cross-linked MatriDerm. In cell culture, the significant decrease in pore size and porosity after cross-linking did not inhibit cell attachment, migration, or proliferation of the human dermal fibroblasts on cross-linked MatriDerm, which may be explained by enhanced fibre strength and elasticity after cross-linking. Interestingly, significantly increased cell proliferation and a more disperse cell migration was found on cross-linked MatriDerm with reduced pore size and porosity. These findings may be attributed to the higher surface wettability of exposure of protein on the cross-linked surface, facilitating cell migration through the pores (Côté & Doillon, 1992). SEM analysis of seeded dermal fibroblasts on Day 14 revealed long process extensions of cells that linked to the underlying scaffolds and to neighbouring cells, indicating strong cell adhesion with the underlying substrate via focal contacts and good overall biocompatibility with both cross-linked and noncross-linked MatriDerm. SEM analysis also confirmed that cross-linked MatriDerm is seemingly more favourable for supporting cell migration and the formation of a confluent layer of dermal fibroblasts over 14 days, while maintaining the integrity of the scaffold. The findings of increased cell proliferation on cross-linked MatriDerm can be further supported by the tendency of human dermal fibroblasts to display favourability towards rigid surfaces (Hsin-I Chang, 2011). By stabilizing the scaffold and increasing its scaffold rigidity, we found enhanced cell proliferation and migration of dermal fibroblasts throughout the template. However, it has also been shown that in more rigid environments, fibroblasts tend to differentiate into myofibroblasts, the main contributor of contraction (Harrison & MacNeil, 2008; Hinz, 2006). Myofibroblasts are activated by stress and strain and subsequently exert their contractile function to bring collagen bundles together. (Hinz, 2016) Yet, in the quest for the ideal dermal template, excessive myofibroblast presence is not desired as further contraction of the template or of the regenerated tissue is unnecessary and would only cause further excessive scarring and contractures. In this study, despite the increased rigidity of cross-linked MatriDerm, cell-scaffold interaction studies did not suggest the presence of excessive myofibroblasts. in vitro experiments showed contraction of cross-linked MatriDerm was present but was significantly less than that of noncross-linked MatriDerm and independent of the presence of human dermal fibroblasts.

At present, MatriDerm remains the only commercial available dermal substitute that contains an elastin element. The presence of elastin has been shown to reduce the differentiation of fibroblasts into myofibroblasts (Kloxin et al., 2010). As myofibroblasts are considered to be the main contributor of scar contraction, (Harrison & MacNeil, 2008; Shin & Minn, 2004) reducing the differentiation could potentially lead to a more pliable scar. In addition, the presence of elastin promotes native elastin production (Daamen et al., 2008; Hinek, Wang, Liu, Mitts, & Jimenez, 2005) and angiogenesis (Daamen et al., 2008; Wang et al., 2015), further supporting healthy scar formation. De Vries et al. (1995) demonstrated that elastin in a collagen-elastin matrix enhanced the architecture of scar tissue, with a more organized formation of collagen, to closer relate to normal skin properties. Therefore, by stabilizing the collagen-elastin matrix, these beneficial effects of elastin could be present in the wound for a longer period of time to further improve scar quality.

By cross-linking MatriDerm, its matrix durability was enhanced without impeding on cell integration and viability, increasing the presence of elastin during the wound healing period and thereby maintaining its supportive influence as well as functionality during cell-matrix interaction and tissue regeneration for a longer period of time. In our study, cross-linked MatriDerm was present and intact for a longer period of time than noncross-linked MatriDerm in vivo. After 2 weeks, cross-linked MatriDerm remained well intact whereas noncross-linked MatriDerm was almost completely biodegraded, allowing cross-linked MatriDerm to extend further into the proliferation phase of wound healing. Angiogenesis appeared to be active and took place earlier in noncross-linked MatriDerm compared with cross-linked MatriDerm in the animal model. Yet prolonged and extensive angiogenesis was observed in wounds with cross-linked MatriDerm, potentially relating to the intact matrix structure and a prolonged presence of elastin. No excessive collagen formation or inflammatory response was noted in cross-linked MatriDerm, which is supported by similar graft take data between both cross-linked and noncross-linked MatriDerm.

Mouse models are commonly used as a cost-effective research tool for informative investigations or preliminary screenings of the efficacy and biosafety of dermal templates and skin substitutes. The in vivo wound contraction and graft take did not appear significantly different in the wounds grafted with cross-linked MatriDerm or noncross-linked MatriDerm. However, some notable limitations should certainly be taken into consideration when interpreting the data from our mouse model study. First, mouse skin is very thin and different from human skin in structures and wound healing mechanism. Mouse skin is well known to heal by contraction due to the presence of panniculus carnosus beneath their skin, whereas human skin heals by re-epithelization, making skin contraction studies limited in mouse models (Abdullahi, Amini-Nik, & Jeschke, 2014). Our in vitro and histological study showed that that cross-linked MatriDerm had stronger mechanical strength, increased stability, and delayed degradation but displayed no significant effect on the wound contraction in comparison with noncross-linked MatriDerm. The wound contraction results from our study are very likely being impacted by the unique contraction mechanisms of mouse skin wound healing. Second, the sample size in our invivo study is relatively small. We examined 18 mice with 9 per group in the study. Although using a well-established and reproducible mouse model, the limited sample size may not allow the detection of any small difference between the wound contractions of study groups. This could lead to inaccuracy when comparing the wound healing, in particular, the measurements of wound contraction between the groups. Although the sample size could be increased for better statistical power, a larger sample size would not resolve the impact associated with inherent contraction healing mechanism of mice. Graft take rate could also be impacted by small sample size. However, for this study, the graft take is less an issue as all wounds in our study, either grafted with cross-linked or noncross-linked, healed completely without any complications as evidenced by histology. MatriDerm is a well-known, clinically approved dermal regenerative template with excellent take rate. In this study, the similar wound healing with no obvious cytotoxicity or unfavourable host reaction between the groups. With non-crossed MatriDerm as a benchmark for comparison, the similarity between the groups may optimistically indicate that the cross-linking, although stabilizing the matrix and slowing down its degradation, did not alter its properties for wound healing.

Based on overall data from this study and with consideration of its limitations, cross-linking MatriDerm enhances the scaffold's strength and stability, prolonging its durability in both in vitro and in vivo experiments. Cross-linked MatriDerm developed a macroscopically sturdier, less fragile scaffold, which was confirmed with tensile testing. It was easier to handle than noncross-linked MatriDerm, resolving a common issue raised by surgeons. Its increased strength and the effect on reducing the biodegradability rate over time allowed for an extended structural integrity of the collagen-elastin matrix and effective cell-matrix interaction. in vitro experiments with human dermal fibroblasts demonstrated viable cells with increased proliferation over and throughout cross-linked MatriDerm, and in vivo results demonstrated similar graft take rates without abnormal or excessive inflammatory response. Cross-linking could potentially enhance the regenerative capacity of MatriDerm in the healing wound. Our in vitro and in vivo data certainly warrant a further investigation of the role of cross-linked MatriDerm in modulating wound healing and contraction. For future study, we would consider the investigation in a more suitable animal model such as porcine with a statistically calculated sample size. A porcine model shares similar skin structures and wound healing mechanism to humans and would allow for larger wound sizes, measuring wound epithelization, contractions, and even scarring more precisely. The data from a porcine model would be more clinically translational to human trials than that from a mouse model.

A dermal scaffold with optimal structural and functionalities including mechanical strength and degradation rate is critical for ideal dermal regeneration in skin tissue engineering. As such, to increase the structural stability and delay its degradation by crosslinking would potentially allow extended structural supports and improved scaffold-guided dermal regeneration to full thickness, which, if being translated clinically, would potentially lead to increased quality of wound healing, reduced wound contraction, and scarring. The future potential of a stronger and sturdier collagen-elastin dermal template lies not only within the benefits of prolonging its in vivo half-life for a longer exposure of elastin in a healing wound but further in the field of cultured epithelial autografts. By creating a scaffold that is rigid enough for dermal fibroblast and keratinocytes to proliferate on in an in vitro environment, autologous cells can be grown in lab on a strong base that will not disintegrate too early, allowing the formation of an autologous cultured living skin substitute, enhancing its future prospective use on the reconstructive ladder.

5 | CONCLUSION

In this study, cross-linking a collagen-elastin matrix with glutaraldehyde was found to increase the scaffold's strength and reduced its biodegradation rate. Exposure to human dermal fibroblasts in an in-vitro environment demonstrated positive compatibility and reduced contraction of the scaffold. Without affecting wound healing or graft take, cross-linked MatriDerm was found to have a prolonged durability in a healing wound, causing no excessive scar formation. Eventhough no significant difference was found in wound contraction, the extended exposure of cross-linked MatriDerm in a wound could potentially have beneficial effects on tissue regeneration, subsequently promoting the formation of a more pliable, healthy scar. As cross-linked MatriDerm presents a more stable three-dimensional matrix, its potential use in skin tissue engineering promises a great future.

ACKNOWLEDGEMENTS

MatriDerm was kindly provided by the Red Cross Hospital and Association of Dutch Burn Centres, Beverwijk, the Netherlands.

CONFLICT OF INTEREST

The authors declare they have no conflict of interest.

ORCID

Joanneke Maitz https://orcid.org/0000-0001-5276-9637

REFERENCES

Abdullahi, A., Amini-Nik, S., & Jeschke, M. G. (2014). Animal models in burn research. (1420–9071 (Electronic)). *Cellular and Molecular Life Sciences*, *71*(17), 3241–3255.

Annabi, N., Fathi, A., Mithieux, S. M., Martens, P., Weiss, A. S., & Dehghani, F. (2011). The effect of elastin on chondrocyte adhesion and proliferation on poly (ε-caprolactone)/elastin composites. *Biomaterials.*, *32*(6), 1517–1525.

Bloemen, M. C., van Leeuwen, M. C., van Vucht, N. E., van Zuijlen, P. P., & Middelkoop, E. (2010). Dermal substitution in acute burns and reconstructive surgery: A 12-year follow-up. *Plastic and Reconstructive Surgery*, *125*(5), 1450–1459. https://doi.org/10.1097/PRS.0b013e3181d62b08

Boekema, B. K., Vlig, M., Damink, L. O., Middelkoop, E., Eummelen, L., Bühren, A. V., & Ulrich, M. M. (2014). Effect of pore size and cross-linking of a novel collagen-elastin dermal substitute on wound healing. *Journal of Materials Science: Materials in Medicine*, *25*(2), 423–433.

Burke, J. F., Yannas, I. V., Quinby, W. C. Jr., Bondoc, C. C., & Jung, W. K. (1981 Oct). Successful use of a physiologically acceptable artificial skin in the treatment of extensive burn injury. *Annals of Surgery*, *194*(4), 413–428.

Chua, A. W. C., Khoo, Y. C., Tan, B. K., Tan, K. C., Foo, C. L., & Chong, S. J. (2016). Skin tissue engineering advances in severe burns: Review and therapeutic applications. *Burns & Trauma*, *4*(1). https://doi.org/10.1186/s41038-016-0027-y

Côté, M.-F., & Doillon, C. J. (1992). Wettability of cross-linked collagenous biomaterials: in vitro study. *Biomaterials*, *13*(9), 612–616. https://doi.org/10.1016/0142-9612(92)90029-N

Daamen, W. F., Nillesen, S. T., Wismans, R. G., Reinhardt, D. P., Hafmans, T., Veerkamp, J. H., & Van Kuppevelt, T. H. (2008). A biomaterial composed of collagen and solubilized elastin enhances angiogenesis and elastic fiber formation without calcification. *Tissue Engineering Part A.*, *14*(3), 349–360.

Dagalakis, N., Flink, J., Stasikelis, P., Burke, J. F., & Yannas, I. V. (1980 Jul). Design of an artificial skin. Part III. Control of pore structure. *Journal of Biomedical materials research.*, *14*(4), 511–528.

De Vries, H. J., Zeegelaar, J. E., Middelkoop, E., Gijsbers, G., Van Marle, J., Wildevuur, C. H., & Westerhof, W. (1995). Reduced wound contraction and scar formation in punch biopsy wounds. Native collagen dermal substitutes. *Br J Dermatol*, *132*(5), 690–697. https://doi.org/10.1111/j.1365-2133.1995.tb00712.x

Druecke, D., Lamme, E. N., Hermann, S., Pieper, J., May, P. S., Steinau, H. U., & Steinstraesser, L. (2004). Modulation of scar tissue formation using different dermal regeneration templates in the treatment of experimental full-thickness wounds. *Wound Repair and Regeneration.*, *12*(5), 518–527.

Fathi, A., Lee, S., Zhong, X., Hon, N., Valtchev, P., & Dehghani, F. (2013). Fabrication of interpenetrating polymer network to enhance the biological activity of synthetic hydrogels. *Polymer*, *54*(21), 5534–5542. https://doi.org/10.1016/j.polymer.2013.08.052

Harrison C A., MacNeil S (2008). The mechanism of skin graft contraction: An update on current research and potential future therapies. *Burns*, *34*, (2), 153–163. https://doi.org/10.1016/j.burns.2007.08.011

Hinek, A., Wang, Y., Liu, K., Mitts, T. F., & Jimenez, F. (2005). Proteolytic digest derived from bovine Ligamentum Nuchae stimulates deposition of new elastin-enriched matrix in cultures and transplants of human dermal fibroblasts. *Journal of Dermatological Science*, *39*(3), 155–166. https://doi.org/10.1016/j.jdermsci.2005.04.002

Hinz B (2006). Masters and servants of the force: The role of matrix adhesions in myofibroblast force perception and transmission. *European Journal of Cell Biology*, *85*, (3-4), 175–181. https://doi.org/10.1016/j.ejcb.2005.09.004

Hinz, B. (2016). The role of myofibroblasts in wound healing. *Current Research in Translational Medicine*, *64*(4), 171–177. https://doi.org/10.1016/j.retram.2016.09.003

Holavanahalli, R. K., Helm, P. A., & Kowalske, K. J. (2010). Long-term outcomes in patients surviving large burns: The skin. *Journal of Burn Care & Research*, *31*(4), 631–639. https://doi.org/10.1097/BCR.0b013e3181e4ca62

Hsin-I Chang, Y. W. (2011). Cell responses to surface and architecture of tissue engineering scaffolds. In D. Eberli (Ed.), *Regenerative medicine and tissue engineering‐Cells and biomaterials*. London, United Kingdom: IntechOpen.

Hur, G. Y., Seo, D. K., & Lee, J. W. (2014). Contracture of skin graft in human burns: Effect of artificial dermis. *Burns: Journal of the International Society for Burn Injuries*, *40*(8), 1497–1503. https://doi.org/10.1016/j.burns.2014.08.007

Jelena Rnjak-Kovacina, A. S. W. (2013). The role of elastin in wound healing and dermal substitute design. In D. B. L. Lars-Peter Kamolz (Ed.), *Dermal replacements in general, burn and plastic surgery*. Dordrecht: Springer. https://doi.org/10.1007/978-3-7091-1586-2_5

Kloxin, A. M., Benton, J. A., & Anseth, K. S. (2010). In situ elasticity modulation with dynamic substrates to direct cell phenotype. *Biomaterials.*, *31*(1), 1–8.

Lamme, E. N., de Vries, H. J., van Veen, H., Gabbiani, G., Westerhof, W., & Middelkoop, E. (1996). Extracellular matrix characterization during healing of full-thickness wounds treated with a collagen/elastin dermal substitute shows improved skin regeneration in pigs. *The Journal of Histochemistry and Cytochemistry*, *44*(11), 1311–1322. https://doi.org/10.1177/44.11.8918906

Nyame T T, Chiang H A, Leavitt T, Ozambela M, Orgill D P (2015). Tissue-Engineered Skin Substitutes. *Plastic and Reconstructive Surgery*, *136*, (6), 1379–1388. https://doi.org/10.1097/prs.0000000000001748

O'Brien F.J., Harley B.A., Yannas I.V., Gibson L.J. (2005). The effect of pore size on cell adhesion in collagen-GAG scaffolds. *Biomaterials*, *26*, (4), 433–441. https://doi.org/10.1016/j.biomaterials.2004.02.052

Philandrianos C, Andrac-Meyer L, Mordon S, Feuerstein J, Sabatier F, Veran J, Magalon G, Casanova D (2012). Comparison of five dermal substitutes in full-thickness skin wound healing in a porcine model. *Burns*, *38*, (6), 820–829. https://doi.org/10.1016/j.burns.2012.02.008

Reddy, N., Reddy, R., & Jiang, Q. (2015). Crosslinking biopolymers for biomedical applications. *Trends in Biotechnology*, *33*(6), 362–369. https://doi.org/10.1016/j.tibtech.2015.03.008

Salem A. K., Stevens R., Pearson R. G., Davies M. C., Tendler S. J. B., Roberts C. J., Williams P. M., Shakesheff K. M. (2002). Interactions of 3T3 fibroblasts and endothelial cells with defined pore features. *Journal of Biomedical Materials Research*, *61*, (2), 212–217. https://doi.org/10.1002/jbm.10195

Schneider, J. C., Holavanahalli, R., Helm, P., Goldstein, R., & Kowalske, K. (2006). Contractures in burn injury: Defining the problem. *Journal of Burn Care & Research*, *27*(4), 508–514. https://doi.org/10.1097/01.BCR.0000225994.75744.9D

Shevchenko R V., James S L., James S. E. (2010). A review of tissue-engineered skin bioconstructs available for skin reconstruction. *Journal of The Royal Society Interface*, *7*, (43), 229–258. https://doi.org/10.1098/rsif.2009.0403

Shin, W. D., & Minn, W. K. (2004). The effect of myofibroblast on contracture of hypertrophic scar. *Plastic and Reconstructive Surgery*, *113*(2), 633–640. https://doi.org/10.1097/01.PRS.0000101530.33096.5B

van Baar, M. E., Essink-Bot, M. L., Oen, I. M., Dokter, J., Boxma, H., & van Beeck, E. F. (2006). Functional outcome after burns: A review. *Burns: Journal of the International Society for Burn Injuries*, *32*(1), 1–9. https://doi.org/10.1016/j.burns.2005.08.007

van der Veen, V. C., van der Wal, M. B., van Leeuwen, M. C., Ulrich, M. M., & Middelkoop, E. (2010). Biological background of dermal substitutes. *Burns: Journal of the International Society for Burn Injuries*, *36*(3), 305–321. https://doi.org/10.1016/j.burns.2009.07.012

Varkey, M., Ding, J., & Tredget, E. E. (2015). Advances in skin substitutes—Potential of tissue engineered skin for facilitating anti-fibrotic healing. *Journal of Functional Biomaterials*, *6*(3), 547–563. https://doi.org/10.3390/jfb6030547

Wang H, Pieper J, Péters F, van Blitterswijk C A, Lamme E N. (2005). Synthetic scaffold morphology controls human dermal connective tissue formation. *Journal of Biomedical Materials Research Part A*, *74A*, (4), 523–532. https://doi.org/10.1002/jbm.a.30232

Wang Y, Beekman J, Hew J, Jackson S, Issler-Fisher A C, Parungao R, Lajevardi S S, Li Z, Maitz P K M. (2018). Burn injury: Challenges and advances in burn wound healing, infection, pain and scarring. *Advanced Drug Delivery Reviews*, *123*, 3–17. https://doi.org/10.1016/j.addr.2017.09.018

Wang, Y., Mithieux, S. M., Kong, Y., Wang, X. Q., Chong, C., Fathi, A., … Weiss, A. S. (2015). Tropoelastin incorporation into a dermal regeneration template promotes wound angiogenesis. *Advanced Healthcare Materials*, *4*(4), 577–584. https://doi.org/10.1002/adhm.201400571

Yang J, Shi G, Bei J, Wang S, Cao Y, Shang Q, Yang G, Wang W (2002). Fabrication and surface modification of macroporous poly(L-lactic acid) and poly(L-lactic-co-glycolic acid) (70/30) cell scaffolds for human skin fibroblast cell culture. *Journal of Biomedical Materials Research*, *62*, (3), 438–446. https://doi.org/10.1002/jbm.10318

Yannas I. V., Burke John F. (1980). Design of an artificial skin. I. Basic design principles. *Journal of Biomedical Materials Research*, *14*, (1), 65–81. https://doi.org/10.1002/jbm.820140108

Yannas I. V., Burke J. F., Gordon P. L., Huang C., Rubenstein R. H. (1980). Design of an artificial skin. II. Control of chemical composition. *Journal of Biomedical Materials Research*, *14*, (2), 107–132. https://doi.org/10.1002/jbm.820140203

Yannas I. V., Lee E., Orgill D. P., Skrabut E. M., Murphy G. F. (1989). Synthesis and characterization of a model extracellular matrix that induces partial regeneration of adult mammalian skin.. *Proceedings of the National Academy of Sciences*, *86*, (3), 933–937. https://doi.org/10.1073/pnas.86.3.933

Received: 3 October 2019 | Revised: 27 December 2019 | Accepted: 30 December 2019

DOI: 10.1002/cam4.2853

ORIGINAL RESEARCH

Cancer Medicine Open Access WILEY

Expression profiles of miRNAs in giant cell tumor of bone showed miR-187-5p and miR-1323 can regulate biological functions through inhibiting FRS2

Yuanhan Jin[1] | **Jing Zhang**[2] | **Hao Zhu**[3] | **Gentao Fan**[3] | **Guangxin Zhou**[3]

[1]Department of Orthopedics, Jinling Hospital, Medical school of Southeast University, Nanjing, China

[2]Department of Orthopedics, Jinling Hospital, Nanjing Medical University, Nanjing, China

[3]Department of Orthopedics, Jinling Hospital, Nanjing University, Nanjing, China

Correspondence
Guangxin Zhou, No. 305 Zhongshan Eastern Road, Nanjing 210002, China.
Email: zhougxnj1@163.com

Funding information
NSFC (Natural Science Foundation of China) ID: 81472508; Name: Novel therapeutic approaches for osteosarcoma developed based on exosome-mediated microRNA transport mechanisms in vivo.

Abstract

Background: Giant cell tumor of bone (GCTB) is considered to be a kind of borderline tumor, which has a tendency to recur and translocate. MicroRNAs are one type of small noncoding RNA, which can inhibit the translation of targeted mRNA through RNA-induced silencing complex.

Methods: Microarray was conducted on three groups of tumor tissues and normal tissues from patients with GCTB, and results showed different expression profiles of miRNAs with Gene Ontology analysis and Kyoto Encyclopedia of Genes and Genomes analysis. The functions of miR-187-5p and miR-1323, which were highly expressed in GCTB, were examined by 5-ethynyl-2′-deoxyuridine (EDU), transwell, and CCK8 assays. RNAhybrid et al. (RNA prediction softwares) predicted that the two microRNAs targeted fibroblast growth factor receptor substrate 2 (FRS2), which was verified by luciferase assay and rescue experiments.

Results: miR-187-5p and miR-1323 were highly expressed in tumor tissues. They can jointly regulate the biological functions of GCTB in vitro. Luciferase assay confirmed that the two microRNAs can bind to the 3′ untranslated regions (UTR) of mRNA of FRS2. And, rescue experiments verified the relationships between the two microRNAs and FRS2.

Conclusion: There were some different-expressed microRNAs between GCTB and normal tissues. miR-187-5p and miR-1323 can regulate the biological functions of GCTB through influencing the expression of FRS2.

KEYWORDS

expression profiles, functions, GCTB, microRNAs

1 | INTRODUCTION

Giant cell tumor of bone (GCTB) is a type of borderline tumor.[1,2] It has low morbidity but high recurrence, so well as high metastasis rate, especially translocating to the lung. Giant cell tumor of bone can occur in most long bones in human bodies, including the distal femur and proximal tibia. And, people aged from 20 to 40 have more morbidity than other age

---

Yuanhan Jin and Jing Zhang contributed equally to this work, and both should be considered as the first authors.

groups.[3] The main pathological ingredients of GCTB include multinucleated giant cells and stromal cells, which have the ultrastructure of osteosarcoma. Meanwhile, the high expression of Receptor activator for nuclear factor-κ B ligand (RANKL) has significant meaning in the development and treatment of GCTB.[4] At present, the main therapies include surgery and medicine.[5] Although the permission of Denosumab (monoclonal antibody for RANKL) treatment on patients with GCTB has been realized,[5] the recurrence and metastasis of GCTB still need other measures to control. Much more molecules and cytokines' functions in GCTB need more exploration.

MicroRNAs are one kind of small noncoding RNAs with the length of 19-25 nt,[6] which can bind to the 3′UTR of mRNA with Argonaute proteins to form RISC (RNA-induced silencing complex), resulting in the inhibited expression of mRNA.[7] Bussing et al firstly found that let-7 is a highly conserved miRNA, which can influence many pathways and processes in cancers.[8] After that, many researches on the mechanism of microRNAs regulating the occurrence and development of tumors have sprung up.[9,10] There have been some miRNAs studied on GCTB, such as miR-30a,[11] miR-127,[12] and miR-376a.[12] These miRNAs could regulate the development of GCTB. However, there are few researches showing a systematic expression profile on microRNAs in GCTB.

This study used microarrays on tissues from patients of GCTB to show the different expression profiles of microRNAs. Moreover, with the detection of microRNAs, we analyzed them through GO (Gene Ontology) analysis and KEGG (Kyoto Encyclopedia of Genes and Genomes) analysis to explore and summarize the functions of these microRNAs deeply. At the same time, we found miR-187-5p and miR-1323 had higher expression in tumor tissues than normal tissues. Thus, we studied the two RNAs about their functions in GCTB in vitro. The aims of the research were to investigate more miRNAs functioning in GCTB and provide some usable information for the treatment of GCTB in the future.

2 | METHODS AND MATERIALS

2.1 | Specimens Collection

Specimens were collected from the patients with GCTB (information shown in Table S1) in Jinling Hospital (Nanjing, China) from January 2016 to January 2019. While the tumor tissues were cut from the patient's bodied, they were put in the collagenase B (Roche Diagnostics). After the primary culture of GCTB cell line, the redundant tissues were stored in refrigerator at −80°C. At the same time, part of normal tissues, which were adjacent to the tumor tissues, was cut and stored at the same state.

The research has been approved by the Ethics Committee of Jinling Hospital (Nanjing, China). And, the use of patients' tissues for the research has been permitted by patients with their signature on the consent files.

2.2 | Cell culture and transfection

The cell line (GCTB) was established from the tumor samples of patients. The tissues were cut into small pieces and digestion of 1.5 mg/mL collagenase B for 3 hours at 37°C in Dulbecco's Modified Eagle Medium (DMEM; Gibco),which contained 10% fetal beef serum (FBS; Gibco) and 100 U/mL penicillin/streptomycin (Gibco). Then, cells suspension was centrifuged, washed twice with phosphate buffer liquid, and cultured in the conditional medium. Twenty-four hours later, the cells were treated with Trypsin (Gibco) to suspend the cells. After three passages, detached cells were cultured to eliminate any remaining giant cells. The main cells we cultured were stromal cells, confirmed by the immunofluorescence of CD68 and PCNA (Figures S1–S3). When the density of cells grew to 80%, we transfected the microRNA mimics and inhibitors into the cells with Lipofectamine® 3000 (Invitrogen). The transfected concentrations of microRNA mimics, inhibitors, and plasmids were dependent on the situations and expectations.

2.3 | Microarray analysis

Microarray was conducted with the Affymetrix® GeneChip miRNA array analysis (Affymetrix), provided by Shanghai Biotechnology Corporation, to explore the expression profiles of microRNAs in GCTB and adjacent normal tissues. The total RNA was extracted from tissues through TRIZOL (Invitrogen). Hybridization signals were detected using an Affymetrix® scanner. With the Gene Clustering 3.0 and Java Tree View, the raw data were analyzed.

2.4 | quantitate Reverse Transcription-Polymerase Chain Reaction (qRT-PCR)

The total RNAs were extracted from tissues and cells through TRIZOL. The extracted RNAs were dissolved in Diethypyrocarbonate (DEPC) water. According to the RNA reverse transcription systems, the reverse transcription solution was prepared (Takara). The PCR machines (MiniAmp; Thermo Fisher) were used to complete the reverse transcription process, and cDNAs were obtained. After that, the real-time quantitative PCR systems (Takara) were prepared according to different cDNAs, and the reactions progressed in the 7900HT Fast Real-Time PCR System (Life Technologies Corporation). miRNAs and mRNAs were performed with probe methods and SYBR GREEN method, respectively. After the reaction, the instrument can analyze the Ct values according to the signals. Through the threshold, targeted RNAs and glyceraldehyde-3-phosphate dehydrogenase (GAPDH)/U6 (internal reference) had their own Ct values. And the deviation between the two Ct values can be considered as ΔCt. The relative RNA levels were represented by $2^{-\triangle Ct}$. The sequences of the primers of fibroblast growth factor (FGF) receptor substrate 2 (FRS2) are shown in supplementary (Table S2).

2.5 | Western Blot

The total proteins were extracted from tissues and cells through RIPA. The superior structure of the protein was disrupted with 5× sodium dodecyl sulfate (SDS) solution. The gels were prepared with a concentration of 12.5%. The antibodies we used in the experiments were “mouse anti-human FRS2” (Santa Cruz, USA), “mouse anti-human GAPDH” (Santa Cruz, USA), and “goat anti-mouse” (Santa Cruz, USA). All the procedures followed the manufactures' instructions. The total protein-SDS solution was added to the gel according to the estimated content of the target protein, and constant voltage of 80 V was applied for electrophoresis with the help of the electrophoresis apparatus (EPS-300-IIV; CBS). After the separation of the protein, the gel was taken out and placed in the transfer capsules with a sponge-thick filter-gel-PVDF membrane-filter paper structure. And, constant current of 0.3 A was applied to transfer the film for 90 minutes. After taking out of the PVDF membranes, according to the ladder, the corresponding bands containing the internal reference protein GAPDH and the target protein on the membranes were cut out. After blocking for 1 hour with 5% milk, the bands were immersed in the respective first antibody solution overnight. Then, the bands were washed by 1× Tris-HCL+Tween buffer solution (TBST) for several times. And, the bands were incubated with the secondary antibody for 1 hour, followed by TBST washing for several times. Then, the bands were reacted with enhanced chemiluminescent (SuperSignal West Femto; Thermo Fisher) and examined by chemiluminescence detector (Fluoroskan; Thermo Fisher). The instrument can collect the signals from the chemiluminescent and the product of intensities and areas could be considered as the parameters of tested proteins. These were recorded and calculated by ImageJ (NIH). The ratio of the parameters of targeted protein and GAPDH (control) represented the relative level of the targeted proteins.

2.6 | luciferase reporter assay

Fibroblast growth factor receptor substrate 2 3′UTR was amplified by the cDNA coding FRS2 (NM_006654.5). The pGL3-basic vectors (Promega) were used to construct the luciferase reporter plasmids, including “wild type” and “mutant type”. These plasmids were co-transfected with microRNA mimics into the cells we cultured. After 24 hours, cell lysis products were extracted and the luciferase activity was examined with the dual-luciferase assay system (Promega). The luciferase activity could represent the binding efficiency of the miRNAs and sequences of 3′UTR. Renilla luciferase activity was used to normalize for transfection efficiency.

2.7 | EUD assay

5-Ethynyl-2’-deoxyuridine (EDU) assay was conducted with Cell-LightTM EdU Apollo567 kit (Guangzhou Ruibo Biotechnology). When the density of cells turned to 80%, the mimics or inhibitors were transfected into cells. After 24 hours, reagent A was added to the medium and cells were cultured for another 4 hours. Then, according to the manufacturer's instructions, the cells were stained. When the staining was done, photos were taken under the microscope (EVOS M7000; Thermo Fisher) at 200×. The uracil could emit red fluorescence under green excitation light and the nucleus could emit blue fluorescence under light blue excitation light. When focusing on one field, the numbers of red and blue were counted and calculated with the help of ImageJ (NIH). The relative proliferation rate was represented by the ratio of red and blue.

2.8 | Transwell assay

The Transwell chambers were bought from CORNING. After transfection, cells were diluted into the concentration of 10^5/well and translocated to the chambers, which were added with DMEM (free FBS). Under the chambers, DMEM containing 20% FBS was filled in the wells. After culturing for 36 hours, the medium was discarded and cells were stained by crystal violet, presenting with blue. Then, the stained cells were captured under the microscope (EVOS M7000; Thermo Fisher) at 100×. Focusing on one field, the blue spots represented the cells that traversed through the porous membrane and glue to reflect the relative invasion rate. The numbers of blue spots were counted and calculated by ImageJ (NIH).

2.9 | Cell viability assay

CCK8 reaction mixture (APExBIO) was used to perform the cell viability experiments. About 100 μL of cell suspension from each well was added into a tube containing 6-mL condition medium to dilute the concentration. Then, the new suspension was averagely spread into 96-well plates with 100 μL of each well. After culturing for 24, 48, 72, 96, 120 hours, respectively, 10-μL CCK8 reaction mixture was added to each well. The enzyme-labeled instrument (Multiskan GO; Thermo Fisher) was used to detect the absorbance of OD450 in each well after culturing the mixture of CCK8 reaction and cells for 2 hours. Every time point had an absorbance which could represent the cellular viability in that time and then comparison of the trend of the absorbance of each sample was the assay result.

2.10 | Statistical analysis

All data statistics were performed with SPSS 20.0 (IBM). Data are expressed as mean ± SD. One-way ANOVA analysis was used to compare the differences among groups. *, **, ***, and **** indicate $P < .05$, $P < .01$, $P < .001$, and $P < .0001$, respectively.

3 | RESULTS

3.1 | Expression profiles of microRNAs in GCTB

The specimens we got during the surgeries were divided into three groups: two normal tissues adjacent to the tumors (group g1), two primary tumor tissues (group g2), and one relapsed tumor tissue + one metastatic tumor tissue in lung (group g3). The group g3 was defined that the two tumors were considered to be with higher malignancy than the tumors in group g2. These three groups' tissues were conducted with microarrays to detect the different microRNAs among them. Defining with the fold change >1.5, the heat maps (Figure 1A) showed that between g2 and g1 there were 17 different miRNAs including eight upregulated and nine downregulated. Comparing g3 with g1, there were eight different-expressed microRNAs. However, unfortunately, few microRNAs were found between g3 and g2, so that we cannot obtain a heat map between them. Besides, three scatter plots (Figure 1B) and volcano plots (Figure 1C) were formed to exhibit the different profiles among the three groups further.

3.2 | Functional pathways analysis of the different-expressed microRNAs

Gene Ontology analysis is the classification of gene functions, including biological process, cellular component, and molecular function.[13] We performed GO analysis among the three groups. The GO classification (Figure 2A) shows that among the three comparisons, most host genes of microRNAs were involved in cellular process of the biological process, cell part of the cellular component, and binding of the molecular function. Moreover, the GO enrichment (Figure 2B) could further elucidate that between g2 and g1, most host genes of different-expressed microRNAs were involved with mediated actin nucleation and intrinsic apoptotic signaling pathway in response to osmotic stress. While comparing g3 and g1, most host genes were connected with the regulation of synaptic vesicle fusion to presynapt and m7G (5′) pppN diphosphatase activity. Between g2 and g3, lung morphogenesis and type endopeptidase activity were obviously involved with more host genes.

Kyoto Encyclopedia of Genes and Genomes analysis is the biological pathway classification entry.[14] The host genes of the microRNAs mainly participated in signal transduction, immune system, and cancers according to the KEGG classification analysis of three comparisons (Figure 2C). Meanwhile, the KEGG enrichment analysis (Figure 2D) showed these host genes could be involved in the Ras signaling pathway, alcoholism, and TGF-beta signaling pathway.

3.3 | miR-187-5p and miR-1323 were downregulated in tissues of GCTB

In terms of the microarrays analysis, we found that miR-187-5p and miR-1323 had low expression in tumor tissues, no matter in the primary tumors or the tumors with higher malignancy. Thus, we performed qRT-PCR on the 20 pairs of tissues of patients with GCTB. As the results showed, miR-187-5p and miR-1323 were overtly downregulated in tumor tissues (Figure 3A).

As a result, we considered that the two microRNAs may function in GCTB. To examine these microRNAs' activities in GCTB, we, respectively, transfected the microRNA mimics into the cells cultured by the GCTB tissues (GCTBSC). qRT-PCR (Figure 3B) showed that after transfection of mimics, the relative level of miR-187-5p and miR-1323 increased concomitantly. And, EDU assay was conducted. As the results (Figure 3C) showed, miR-187-5p and miR-1323 mimics can separately inhibit the proliferation rate of GCTBSC, but co-transfection of the two microRNAs can have joint influence on GCTBSC. Meanwhile, transwell assay (Figure 3D) confirmed the inhibition of translocation of GCTBSC by the two microRNAs.

FIGURE 1 MicroRNAs were differently expressed among the three groups shown by microarrays. A, The heat map of the aberrant microRNAs (fold change [FC] > 1.5). The left showed the microRNAs between g2 and g1, while the right showed between g3 and g1. B, The scatter plots of the aberrant microRNAs (FC > 1.5). The left showed the microRNAs between g2 and g1. The middle showed between g3 and g1, while the right showed between g2 and g3. C, The volcano plots of the aberrant microRNAs (FC > 1.5). The picture sequence was similar to the aforementioned

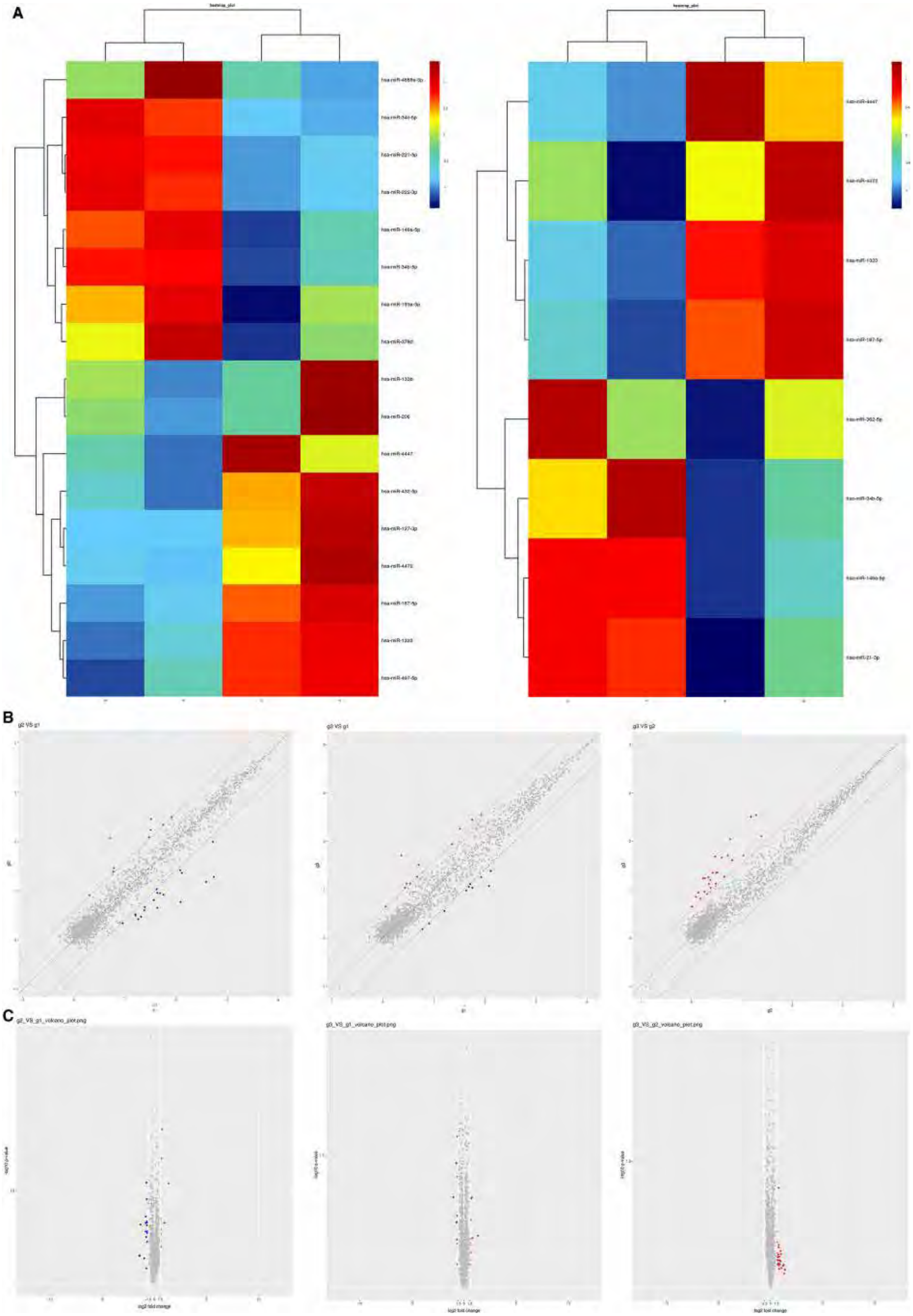
A
heatmap_plot
hsa-miR-4668a-3p
hsa-miR-34c-5p
hsa-miR-221-5p
hsa-miR-222-3p
hsa-miR-146a-5p
hsa-miR-34b-5p
hsa-miR-181a-5p
hsa-miR-376c
hsa-miR-133b
hsa-miR-206
hsa-miR-4447
hsa-miR-432-5p
hsa-miR-127-3p
hsa-miR-4472
hsa-miR-187-5p
hsa-miR-1323
hsa-miR-487-5p
heatmap_plot
hsa-miR-4447
hsa-miR-4472
hsa-miR-1323
hsa-miR-187-5p
hsa-miR-362-5p
hsa-miR-34b-5p
hsa-miR-146a-5p
hsa-miR-21-3p
B
g2 VS g1
g3 VS g1
g3 VS g2
C
g2_VS_g1_volcano_plot.png
g3_VS_g1_volcano_plot.png
g3_VS_g2_volcano_plot.png
log2 fold change
log2 fold change
log2 fold change

FIGURE 2 The aberrant microRNAs could have some functions. A, The results of Gene Ontology (GO) classification analysis. The left showed the compared analysis between g2 and g1. The middle showed between g3 and g1, while the right showed between g2 and g3. B, The results of GO enrichment analysis. The picture sequence was similar to the aforementioned. C, The results of Kyoto Encyclopedia of Genes and Genomes (KEGG) classification analysis. The picture sequence was similar to the aforementioned. D, The results of KEGG enrichment analysis. The picture sequence was similar to the aforementioned

And, CCK8 assay (Figure 3E) was performed to verify the cellular viability. With high expression of the two microRNAs, viability of GCTBSC was overtly impaired and the situation deteriorated when co-transfection. To further examine the effect brought by the two microRNAs, the miR-187-5p and miR-1323 inhibitors were utilized and the abovementioned three

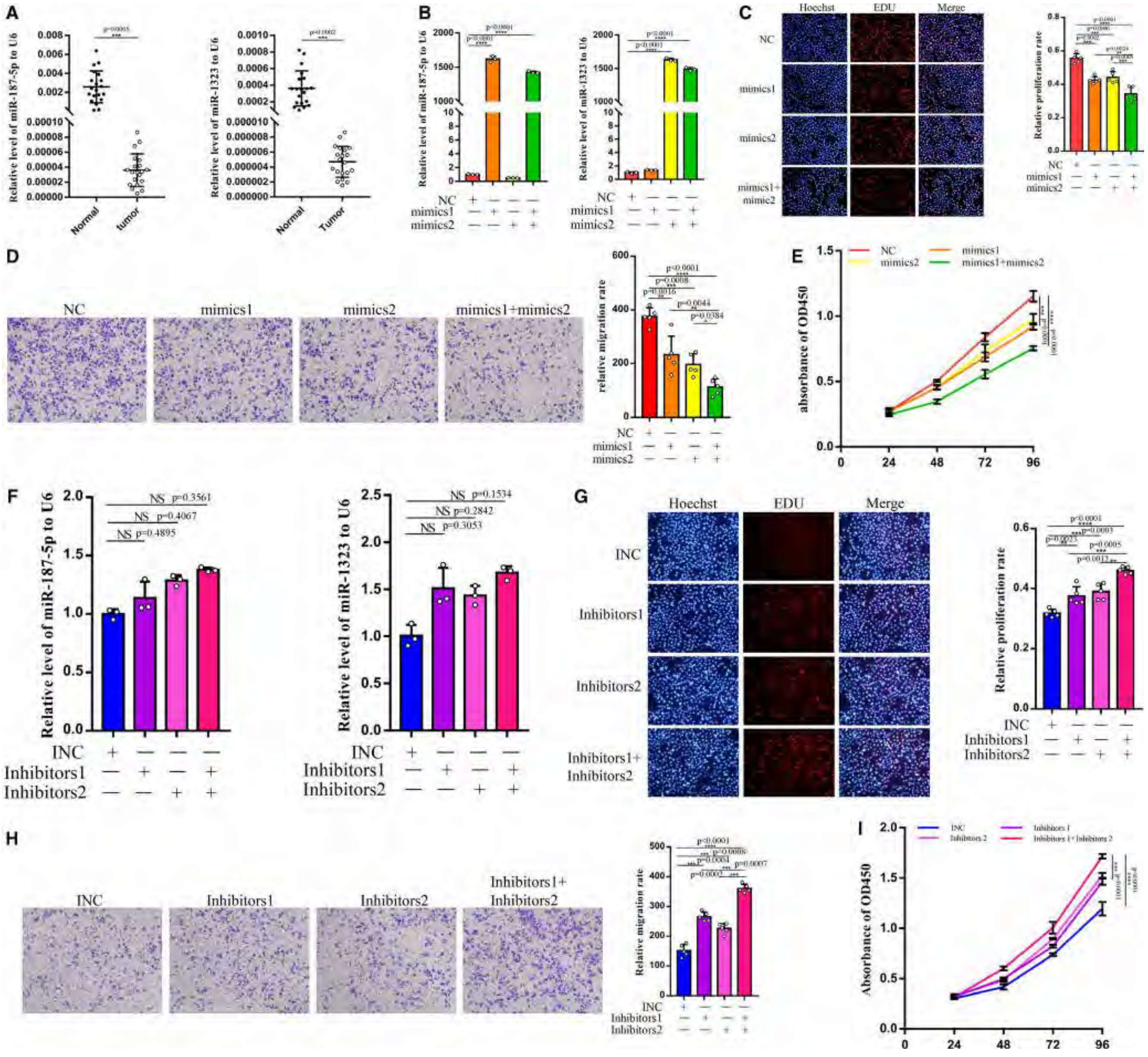

FIGURE 3 miR-187-5p and miR-1323 can regulate the biological functions of GCTBSC. A, The two miRNAs had a low expression in tumor tissues shown by qRT-PCR. B, The relative levels of the two miRNAs after the transfection of the mimics. C, After the transfection of mimics, the EDU assay examined the proliferation of GCTBSC. And, the right picture showed the statistical results. D, Transfection was tested by transwell assay and statistical result showed the significance. E, The cell counting kit-8 (CCK8) assay showed that the mimics can inhibit the cellular viability. F, The relative levels of the two miRNAs after the inhibitors transfection. G, The EDU assay and statistic results showed that the two inhibitors can prompt the proliferation. H, The transwell assay verified the improvement of translocation. I, The CCK8 showed the change in cellular viability. "NS", "*", "**", "***", and "****" represented none sense, $P < .05$, $P < .01$, $P < .001$, and $P < .0001$, respectively. "NC", "mimics1", and "mimics2" represented negative control, miR-187-5p mimics, and miR-1323 mimics, respectively. "INC", "inhibitors1", and "inhibitors2" represented inhibitors negative control, miR-187-5p inhibitors, and miR-1323 inhibitors, respectively. GCTB, giant cell tumor of bone

function assays (Figure 3f-i) were performed. As we expected, inhibitors of the two microRNAs had positive influence on GCTBSC.

To sum up, we can control the relative level of miR-187-5p and miR-1323 to regulate the total biological functions of GCTBSC. Besides, simultaneously changing the level of the two microRNAs could have a united effect.

3.4 | miR-187-5p and miR-1323 may depress FRSC through RISC

According to previous researches, microRNAs were cleaved by Drosha and Dicer, and one strand of the two was selected to bind to Argonaute proteins. RISC was formed to recognize certain mRNA, bind to it, and repress its translation. In view

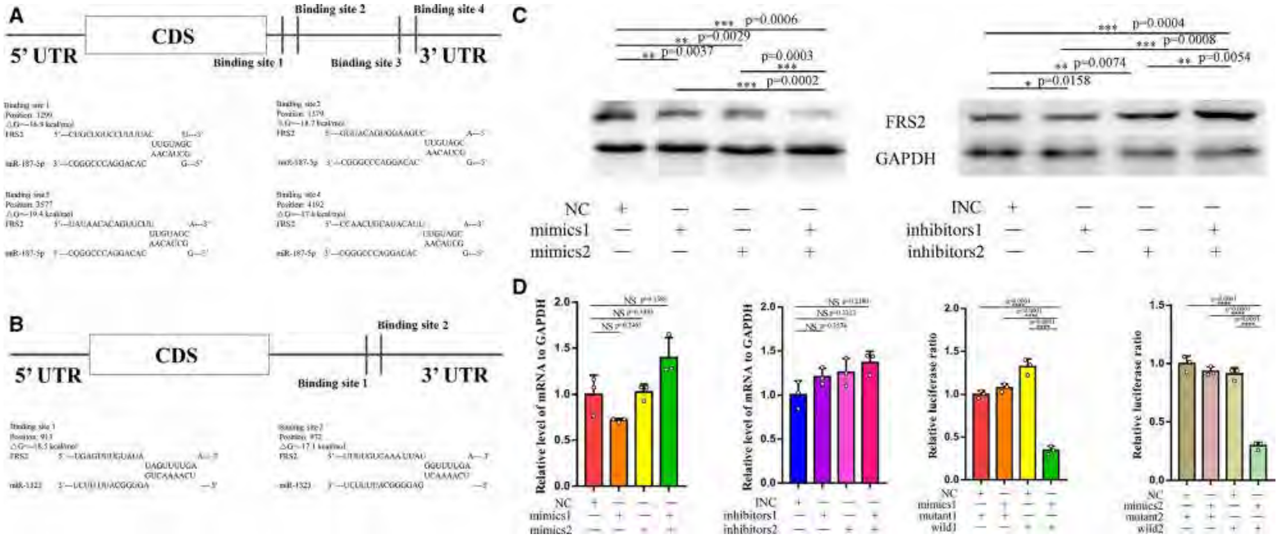

FIGURE 4 FRS2 was predicted to be targeted by miR-187-5p and miR-1323 by three software. A, The schematic diagram of the binding sites of miR-187-5p and the binding sequence. B, The schematic diagram of the binding sites of miR-1323 and the binding sequence. C, Western blot results that the mimics and inhibitors can regulate the protein levels of FRS2 in cells. D, The relative levels of mRNA of FRS2 in cells after the transfection of the mimics and inhibitors showed little change. E, Luciferase reporter assays confirmed the 3′UTR of mRNA of FRS2 can be bound by the two mimics, and the luciferase activities had a significant decrease while co-transfecting with the wild and mimics. "NS", "*", "**", "***", and "****" represent none sense, $P < .05$, $P < .01$, $P < .001$, and $P < .0001$, respectively. "wild1" and "mutant1" represented the luciferase reporter plasmids that contained the wild type and mutant type of the binding sites that miR-187-5p could bind to the mRNA 3′UTR of FRS2, respectively. "wild2" and "mutant2" represented the luciferase reporter plasmids contained the wild type and mutant type of the binding sites that miR-1323 could bind to the mRNA 3′UTR of FRS2, respectively

of the inhibited activity of miR-187-5p and miR-1323, we presumed that the two miRNAs may silence some mRNAs to approach their goals. Thus, with the prediction of the software including Targetscan, miRanda, and RNAhybrid, we found that miR-187-5p and miR-1323 could both bind to the 3′UTR of FRS2. As Targetscan showed 3′UTR FRS2 had four binding sites for miR-187-5p (Figure 4A) and two binding sites for miR-1323 (Figure 4B). Then, with the examination of Western blot (Figure 4C), we found that mimics and inhibitors of the two microRNA can obviously alter the relative protein level of FRS2. Yet, the mRNA levels of FRS2 were relatively steady (Figure 4D). Subsequently, we assigned the 3′UTR of FRS2 into the luciferase reporter vectors (wild), and also the mutant of the 3′UTR (mutant) was implemented as control. After the co-transfection of two mimics with the wild and mutant luciferase reporter vectors separately, the mimics could evidently decrease the luciferase activities in GCTBSC, while mutant vectors had little influence on the luciferase activities (Figure 4E).

As a result, we determined that miR-187-5p and miR-1323 could repress the expression of FRS2 through the binding of the 3′UTR of mRNA.

3.5 | Inhibition of FRS2 could limit the biological functions of GCTBSC

Although we had elucidated the binding of miR-187-5p and miR-1323 to the 3′UTR of FRS2, the functions of FRS2 in GCTB have yet been ambiguous. Firstly, we detected the expression of FRS2 in tumor tissues and normal tissues of patients with GCTB. And, the relative protein level was probed by immunohistochemistry. As the result (Figure 5A) showed, FRS2 had an ectopic expression in GCTB. To further dig into its functions in GCTB, we designed three types of siRNAs targeting FRS2 (siRNA1, siRNA2, siRNA3 sequences shown in Table S2). And, the three siRNAs can evidently decrease the protein and mRNA level of FRS2 in GCTBSC demonstrated by Western blot and qRT-PCR (Figure 5B). Following on the transfection of the siRNAs, aforementioned function assays (Figure 5C-E) were conducted in GCTBSC. As expected, siRNAs targeting FRS2 had generated significant suppressive impact on GCTBSC. And, the functions of forced expression of FRS2 would be stated later. With the evidences shown above, we can conclude that FRS2 may play an important role in GCTB as a proto-oncogene. And, the downregulation of its expression in GCTBSC could impose a restriction on tumor activities.

3.6 | miR-187-5p and miR-1323 can regulate biological functions of GCTB through the repression of FRS2

The functions of miR-187-5p and miR-1323 had been proved in GCTBSC, as well as FRS2. However, we could not figure out the exact mechanism of the influence of the two

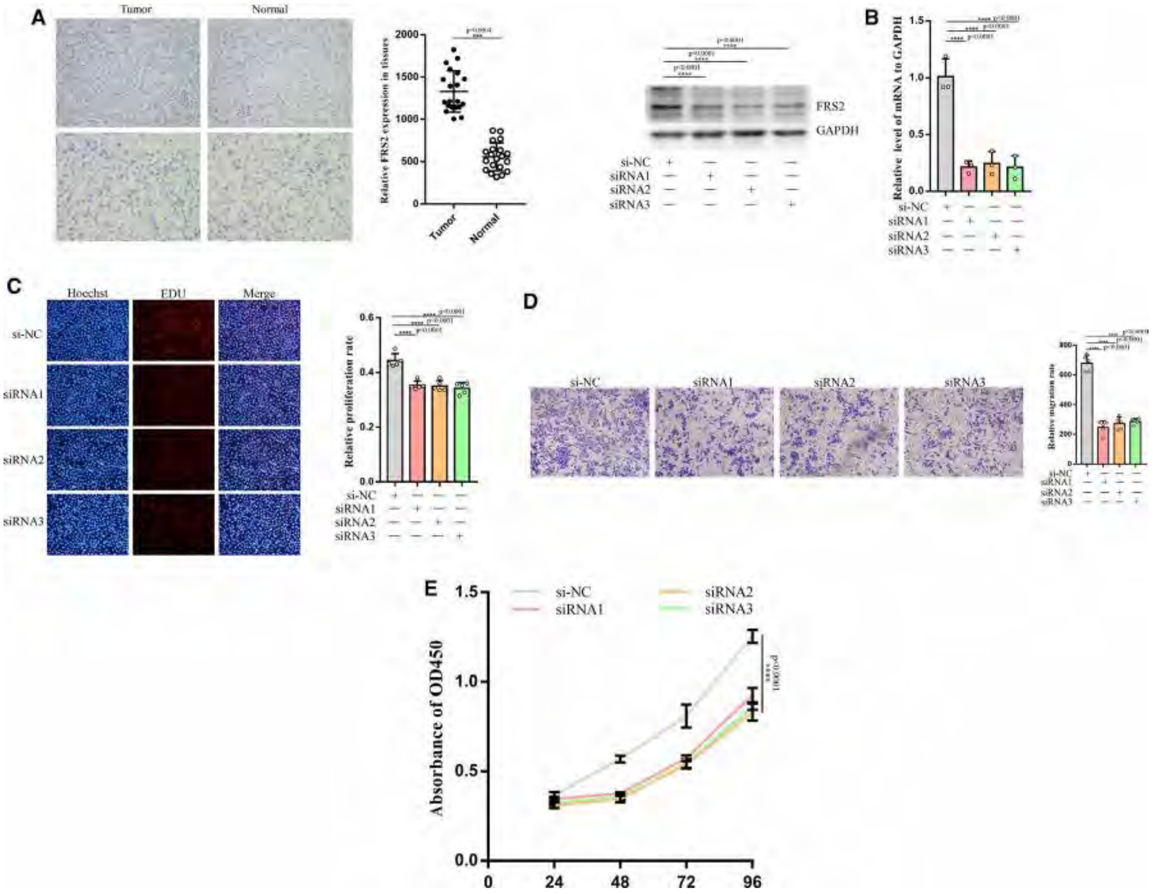

FIGURE 5 FRS2 was downregulated in tumor tissues and can influence the functions of GCTBSC. A, The immunohistochemistry of FRS2 in tumor tissues and normal tissues. The above two photos were taken at 200× and the down were taken at 400×. And, the statistical result showed the significance. B, After transfection of three siRNAs and negative control, the relative protein and mRNA levels of FRS2 in cells were examined by Western blot (left) and qRT-PCR (right). C, The EDU assay and its statistical result showed that the three siRNAs can overtly block cell proliferation. D, The transwell assay and its statistical result showed the inhibition of translocation by the three siRNAs. E, Cellular viability was tested by CCK8 and downregulated. “***” and “****” represent none sense, $P < .05$, $P < .01$, $P < .001$, and $P < .0001$, respectively. “si-NC” represented siRNA negative control. GCTB, giant cell tumor of bone

microRNAs exerting on GCTBSC. To prove the conjecture that the two microRNAs realized their roles by silencing FRS2 in GCTBSC, we performed the rescue experiments. The vectors forcedly expressing FRS2 were designed and co-transfected with the two microRNA mimics into GCTBSC. As Western blot (Figure 6A) showed, forced expression of FRS2 could be recovered to the level of negative control by the addition of the two microRNAs. Nonetheless, the relative mRNA level of FRS2 had little change even through the interruption of the two microRNAs (Figure 6B,C). Far more importantly, as far as the function assays (Figure 6D-F) conducted, the FRS2-overexpressed plasmids could prompt the total cellular activities, including proliferation, translocation, and cellular viability. Yet, after the addition of the two kinds of mimics, the positive influence could be alleviated, especially the combined addition of miR-187-5p and miR-1323 mimics.

As a result, we had a conclusion that the co-transfection of the FRS2-overexpressed plasmids and microRNA mimics could adjust the influence caused by the sole transfection of FRS2-overexpressed plasmids. Further, we could also reach that miR-187-5p and miR-1323 could regulate the biological functions of GCTB through repressing the expression of FRS2.

4 | DISCUSSION

Giant cell tumor of bone is a borderline tumor, which has a high recurrence and a tendency to translocation, especially the lung.[1,2] Even though Denosumab has been approved to treat for GCTB,[5] there exists a need to demonstrate the mechanism of occurrence and development of the tumor in order to find more effective molecules functioning in GCTB.

MicroRNAs are considered as one kind of small noncoding RNAs, with a length of 19-25 nt.[6] It is recognized that microRNAs could form into RISC with Argonaute proteins and repress the translation of certain mRNAs.[7] There have been some research on microRNAs in GCTB. Quan Huang's

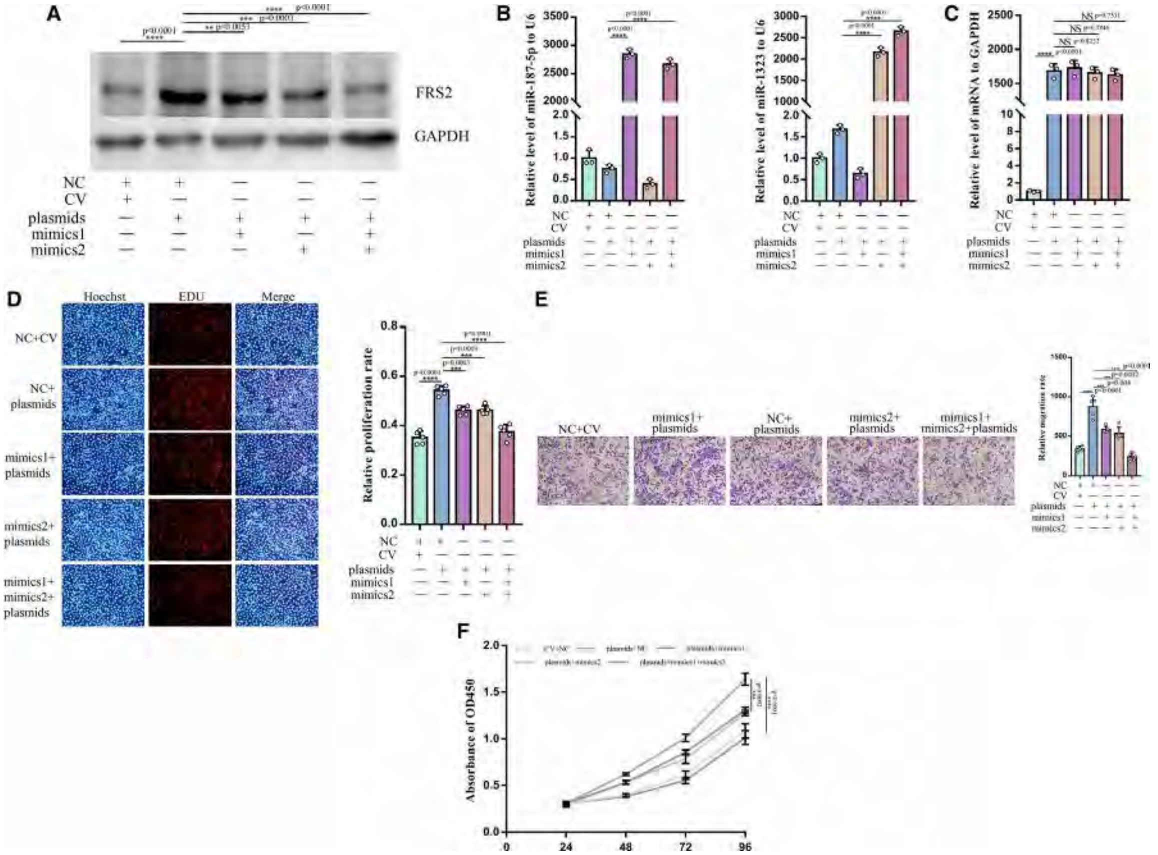

FIGURE 6 miR-187-5p and miR-1323 can regulate the biological functions of GCTB through blocking the expression of FRS2. A, After the co-transfection, the relative protein levels of FRS2 in cells. B, qRT-PCR showed the relative miRNA levels after co-transfection. C, The relative mRNA levels of FRS2 increased after adding FRS2-overexpressed plasmids. D-F, The function experiments showed the mimics can rescue the influence exerted by the plasmids. "NS", "**", "***", and "****" represent none sense, $P < .05$, $P < .01$, $P < .001$, and $P < .0001$, respectively. "CV" and "plasmids" represented the negative vectors and FRS2-overexpressed plasmids, respectively. GCTB, giant cell tumor of bone

team found that miR-30a can target RUNX2 to inhibit the osteolysis in GCTB.[11] And, Ingrid Herr's research proved that miR-127 and miR-376a can act as tumor suppressors through the silence of COA1 and PDIA6 in GCTB.[12] Nonetheless, few researches on microarrays conducted in GCTB have been launched. We performed the microarrays on three groups of GCTB and found two microRNAs, miR-187-5p and miR-1323, downregulated in tumor tissues, no matter primary tissues or recrudescent tissues. miR-187-5p has been found to target CYP1B1 to suppress cancer cell progression in non-small cell lung cancer.[15] Besides, Li et al proved that miR-187-5p may be associated with cell biological functions of bladder cancer.[16] It may be involved with drug sensitivity in breast cancer cell lines as well. Initially, miR-1323 was raised to be upregulated in complete hydatidiform moles.[17] And then, Priscilla T-Y Law's team predicted that miR-1323 was upregulated and linked with the poor prognosis in hepatocellular carcinoma.[18] Afterward, it has been found in the prediction of resistance to neoadjuvant radiochemotherapy in squamous cell carcinoma of the esophagus.[19] However, there has no research exploring their functions in GCTB. Thus, our team firstly discovered the aberrant expression of the two microRNAs and examined their functions in GCTB.

miR-187-5p and miR-1323 have been examined to synergistically regulate the biological functions of GCTB in vitro as we utilized the mimics and inhibitors. Yet, to elucidate the deep mechanism behind the regulation, we conjectured that miR-187-5p and miR-1323 may have a common targeted mRNA, FRS2, through the calculation and prediction of the three software. Fortunately, after the transfection of the two microRNA mimics and inhibitors, the protein level of FRS2 had some predicted changes with the stable level of mRNA. Besides, luciferase reporter assays further confirmed our forecast. Fibroblast growth factor receptor (FGFR) substrate 2 is one type of the adaptor/scaffold protein, which can bind to receptor tyrosine kinases and activate downstream signals.[20] Zhang et al found that FRS2 had a high expression in high-grade liposarcoma and activation of the FGFR/FRS2 signaling may play an important role in the development of liposarcoma.[21] Dey's team launched a research that inhibition of FRS2 could block the PI3K/AKT signaling to induce apoptosis and suppress the proliferation and translocation in breast cancer.[22] Song Wu et al figured out that FRS2 had an obviously upregulation in bladder cancer through whole-genome sequencing, which could recruit endothelial cells and induce tube formation.[23] Based on these studies, we conducted immunohistochemistry in GCTB tissues and adjacent normal tissues, and found that FRS2 was highly expressed in tumor tissues. Besides, siRNA targeting FRS2 confirmed that interruption of its expression in GCTBSC could alleviate the tumor activities. Finally, we co-transfected plasmids expressing FRS2 with the two kinds of mimics into GCTBSC to verify that the plasmids can exacerbate the tumor activities, while the addition of the two mimics could recover the influence of the plasmids.

Unfortunately, we could not construct the animal models of GCTB so that we have not examined our prediction in vivo. Even though there are some researches mocking the tumors with the chick embryo chorioallantoic membrane assay,[24] we have been doubting its reliability and validity.

5 | CONCLUSION

Through microarray, we found the ectopic expression of several microRNAs in GCTB. miR-187-5p and miR-1323 were highly expressed in tumor tissues, which could unitedly regulate biological functions of GCTB in vitro. Furthermore, mRNA of FRS2 could be targeted and repressed by the two microRNAs, so as to compromise the tumor activities.

ORCID

Yuanhan Jin https://orcid.org/0000-0002-1963-0198

REFERENCES

1. Wülling M, Engels C, Jesse N, Werner M, Delling G, Kaiser E. The nature of giant cell tumor of bone. *J Cancer Res Clin Oncol*. 2001;127(8):467-474.
2. Turcotte RE. Giant cell tumor of bone. *Orthop Clin North Am*. 2006;37(1):35-51.
3. Klenke FM, Wenger DE, Inwards CY, Rose PS, Sim FH. Giant cell tumor of bone: risk factors for recurrence. *Clin Orthop Relat Res*. 2011;469(2):591-599.
4. Orosz Z, Athanasou NA. Giant cell-containing tumors of bone. *Surg Pathol Clin*. 2017;10(3):553-573.
5. Wei G, Jianmin L, Jingnan S, et al. Guideline for clinical evidence-based diagnosis and treatment of giant cell tumor of bone. *J Bone Joint Surg Ch*. 2018;11(04):41-52.
6. Hagan JP, Croce CM. MicroRNAs in carcinogenesis. *Cytogenet Genome Res*. 2007;118(2–4):252-259.
7. Bartel DP. MicroRNAs: target recognition and regulatory functions. *Cell*. 2009;136(2):215-233.
8. Büssing I, Slack FJ, Großhans H. let-7 microRNAs in development, stem cells and cancer. *Trends Mol Med*. 2008;14(9):400-409.
9. Eder M, Scherr M. MicroRNA and lung cancer. *N Engl J Med*. 2005;352(23):2446-2448.
10. Yu F, Yao H, Zhu P, et al. let-7 regulates self renewal and tumorigenicity of breast cancer cells. *Cell*. 2007;131(6):1109-1123.
11. Huang Q, Jiang Z, Meng T, et al. MiR-30a inhibits osteolysis by targeting RunX2 in giant cell tumor of bone[J]. *Biochem Biophys Res Comm*. 2014;453(1):160-165.
12. Herr I, Sähr H, Zhao Z, et al. MiR-127 and miR-376a act as tumor suppressors by in vivo targeting of COA1 and PDIA6 in giant cell tumor of bone. *Cancer Lett*. 2017;409:49.
13. Ashburner M, Ball CA, Blake JA, et al. Gene Ontology: tool for the unification of biology. The Gene Ontology Consortium. *Nat Genet*. 2000;25(1):25-29.
14. Draghici S, Khatri P, Tarca AL, et al. A systems biology approach for pathway level analysis. *Genome Res*. 2007;17(10):1537-1545.
15. Mao M, Wu Z, Chen J. MicroRNA-187-5p suppresses cancer cell progression in non-small cell lung cancer (NSCLC) through down-regulation of CYP1B1[J]. *Biochem Biophys Res Comm*. 2016;478(2):649-655.
16. Li Z, Lin C, Zhao L, et al. Oncogene miR-187-5p is associated with cellular proliferation, migration, invasion, apoptosis and an increased risk of recurrence in bladder cancer. *Biomed Pharmacother*. 2018;105:461-469.
17. Na Q, Wang D, Song W. Underexpression of 4 placenta-associated microRNAs in complete hydatidiform moles. *Int J Gynecol Cancer*. 2012;22(6):1075-1080.
18. Law P-Y, Qin H, Ching A-K, et al. Deep sequencing of small RNA transcriptome reveals novel non-coding RNAs in hepatocellular carcinoma. *J Hepatol*. 2013;58(6):1165-1173.
19. Slotta-Huspenina J, Drecoll E, Feith M, et al. Correction to: microRNA expression profiling for the prediction of resistance to neoadjuvant radiochemotherapy in squamous cell carcinoma of the esophagus. *J Transl Med*. 2018;16(1):128.
20. Kouhara H, Hadari YR, Spivak-Kroizman T, et al. A lipid-anchored Grb2-binding protein that links FGF-receptor activation to the Ras/MAPK signaling pathway. *Cell*. 1997;89(5):693-702.
21. Zhang K, Chu K, Wu X, et al. Amplification of FRS2 and activation of FGFR/FRS2 signaling pathway in high-grade liposarcoma. *Can Res*. 2013;73(4):1298-1307.
22. Voshol PJ, Dey JH, Oakeley E, et al. Targeting fibroblast growth factor receptors blocks PI3K/AKT signaling, induces apoptosis, and impairs mammary tumor outgrowth and metastasis. *Can Res*. 2016;70(10):4151-4162.
23. Wu S, Ou T, Xing N, et al. Whole-genome sequencing identifies ADGRG6 enhancer mutations and FRS2 duplications as angiogenesis-related drivers in bladder cancer. *Nat Commun*. 2019;10(1):720.
24. Balke M, Neumann A, Szuhai K, et al. A short-term in vivo model for giant cell tumor of bone. *BMC Cancer*. 2011;11(1):241-241.

SUPPORTING INFORMATION

Additional supporting information may be found online in the Supporting Information section.